Numerical Simulations of Laminar and Turbulent Mixing Layers behind a Thin Airfoil

By:

Saeed Rahbarimanesh

Supervised by:

Dr. Catherine Mavriplis

A thesis submitted to the Faculty of Graduate and Postdoctoral Studies
in partial fulfillment of the requirements for the degree of

MASTER OF APPLIED SCIENCE

in Mechanical Engineering

Ottawa-Carleton Institute for Mechanical and Aerospace Engineering
University of Ottawa
Ottawa, Canada

August 2015

Abstract

Steady and unsteady simulations of two-stream incompressible mixing layers with a fixed velocity ratio of 2, generated at the trailing edge of a NACA0006 airfoil in 2D and 3D domains are investigated in laminar and turbulent flow regimes.

Numerical simulations are first conducted to study the behavior of mixing layers in laminar flow regimes. Effects of high-speed side free-stream Reynolds number and temperature are investigated and considered in relation to prediction of the developing behavior of the 2D mixing layer. Unsteady behavior of the 3D case in a range of free-stream Reynolds numbers is also explored and visualized by using parallel computation. Having shown that shape factors in both streamwise and spanwise directions increase with increasing free-stream velocity, it is found that for the 2D case raising the high-speed side flow temperature reduces the stability of the velocity profiles. The rate of reduction is accelerated by employing higher Reynolds numbers.

Turbulent mixing layers behind the airfoil are studied numerically by employing parallel computation for Reynolds-Averaged Navier-Stokes (RANS)-based models for 2D and 3D grids. In addition, large eddy simulation (LES) is conducted to explore 3D behavior of the turbulent mixing layer. Effects of inflow turbulence intensity as well as Reynolds number are investigated by examining growth rate parameters. Although the applied turbulence models predict almost the same trends of spreading rate and velocity distribution, the SST model in 2D cases and the LES model in 3D cases gave the best results. It is also found that shape factor decreases with increasing turbulence intensity. Furthermore, increasing the Reynolds number did not show any significant influence on this trend. In the spanwise direction, the shape factor variation does not follow this trend.

Acknowledgements

I would like to express my deepest gratitude to my supervisor Dr. Catherine Mavriplis, for her kind help, professionalism, and valuable technical guidance throughout the entire period of my research at the University of Ottawa. I am so grateful and simply have no further words to explain her support and patience.

A deep appreciation is extended to my family for providing me with continuous encouragement to maintain my focus on my studies. I truly appreciate all their support and advice during this experience. This accomplishment could not be achieved without them.

I would also like to thank my friends who helped me through their promoting suggestions.

Table of Contents

List of Figures

List of Tables

Nomenclature

Roman Characters

C	**Chord length**	**m**
c_p	**Specific heat capacity at constant pressure**	$\frac{\mathbf{J}}{\mathbf{kg-K}}$
D_h	**Hydraulic diameter**	**m**
g	**Gravity**	$\frac{\mathbf{m}}{\mathbf{s}^2}$
H	**Shape factor**	**-**
h	**Mixing layer thickness**	**m**
I	**Turbulence intensity**	**%**
I_{edge}	**Turbulence intensity at the edge of the mixing layer**	**%**
k	**Turbulent kinetic energy**	$\frac{\mathbf{m}^2}{\mathbf{s}^2}$
k_h	**Thermal conductivity coefficient**	$\frac{\mathbf{W}}{\mathbf{m-K}}$ / $\frac{\mathbf{m}^2}{\mathbf{s}}$
k_{h0}	**Initial thermal conductivity coefficient**	$\frac{\mathbf{W}}{\mathbf{m-K}}$ / $\frac{\mathbf{m}^2}{\mathbf{s}}$
k_l	**Laminar kinetic energy**	$\frac{\mathbf{m}^2}{\mathbf{s}^2}$
L	**Channel length**	**m**
l	**Turbulent length scale**	**m**
N	**Time period**	**sec(s)**
p	**pressure**	**Pa**
Q	**Volume flow rate**	$\frac{\mathbf{m}^3}{\mathbf{s}}$
q	**Heat flux**	$\frac{\mathbf{W}}{\mathbf{m}^2}$
Re	**Reynolds number**	**-**
$Re_{critical}$	**Critical Reynolds number**	**-**

Re_{δ^*}	**Displacement thickness Reynolds number**	-
Re_{θ}	**Momentum thickness Reynolds number**	-
$\widetilde{Re}_{\theta_t}$	**Momentum thickness Reynolds number at transition**	-
r	**Velocity ratio of high-speed side to low-speed side**	-
T	**Temperature**	K
T_{ref}	**Reference temperature**	K
$T1$	**Dimensionless temperature scale (ratio of airfoil surface temperature to high-speed side free-stream temperature)**	-
$U,\ U_{\infty}, U_{o}, U_{inf}$	**Free-stream inflow velocity (high-speed side)**	$\frac{\mathrm{m}}{\mathrm{s}}$
U_{edge}	**Outer stream velocity at the edge of the mixing layer**	$\frac{\mathrm{m}}{\mathrm{s}}$
$U_{low\ (high)-speed\ side}$	**Low (High)-speed side free-stream velocity**	$\frac{\mathrm{m}}{\mathrm{s}}$
$u, v\ , w$	**Cartesian velocity components in streamwise, transverse, and spanwise directions**	$\frac{\mathrm{m}}{\mathrm{s}}$
$\overline{u}, \overline{v}\ , \overline{w}$	**Mean streamwise, transverse, and spanwise velocities**	$\frac{\mathrm{m}}{\mathrm{s}}$
$\overline{u'^2}, \overline{v'^2}, \overline{w'^2}$	**Reynolds normal stresses (mean-square)**	$\frac{\mathrm{m}^2}{\mathrm{s}^2}$
$\overline{u'v'}, \overline{u'w'},\ \overline{v'w'}$	**Reynolds shear stresses (mean-square)**	$\frac{\mathrm{m}^2}{\mathrm{s}^2}$
x, y , z	**Streamwise, transverse, spanwise coordinates**	m
x^*	**Dimensionless x coordinate – Laminar mixing layer**	-
y_0	**Center of the turbulent mixing layer**	m
y^+	**Wall coordinate (wall-function law)**	-
y^*	**Dimensionless y scale – Laminar mixing layer**	-

Greek Symbols

γ	**Turbulence intermittency**	**-**
δ	**Boundary layer thickness**	**m**
δ_w	**Vorticity thickness of the turbulent mixing layer**	**m**
δ^*	**Displacement thickness**	**m**
δ^{**}	**Dimensionless displacement thickness**	**-**
ϵ	**Dissipation rate**	$\frac{\mathrm{m}^2}{\mathrm{s}^3}$
η	**Dimensionless similarity solution variable (Blasius)**	**-**
η^+	**Kolmogorov length scale**	**-**
θ	**Momentum thickness**	**m**
θ^*	**Dimensionless momentum thickness**	**-**
λ	**Dissipation coefficient (Stokes' hypothesis)**	$\frac{\mathrm{kg}}{\mathrm{m}-\mathrm{s}}$
μ	**Molecular viscosity**	$\frac{\mathrm{kg}}{\mathrm{m}-\mathrm{s}}$
μ_t	**Turbulent viscosity**	$\frac{\mathrm{kg}}{\mathrm{m}-\mathrm{s}}$
μ_{t-SGS}	**Turbulent sub-gird scale viscosity**	$\frac{\mathrm{kg}}{\mathrm{m}-\mathrm{s}}$
ν	**Kinematic viscosity**	$\frac{\mathrm{m}^2}{\mathrm{s}}$
ξ	**Dimensionless transverse length scale for mixing layer**	**-**
ρ	**Density**	$\frac{\mathrm{kg}}{\mathrm{m}^3}$
σ	**Spreading parameter**	**-**
τ	**Dimensionless time**	**-**
τ_{ij}	**Shear stress tensor with respect to x and y coordinates**	**Pa**
φ	**Dissipation function**	$\frac{\mathrm{kg}}{\mathrm{m}^3}$

$\boldsymbol{\omega}$	**Specific dissipation rate**	$\frac{1}{s}$
Δx , Δy	**Grid element size in x and y direction**	**m**
Δt	**Time step**	**sec(s)**

Subscripts and Superscripts

$(\ )'$	**Fluctuating part of the quantity**
$\overline{(\ )}$	**Mean part of the quantity**
$(\ )_{i,j,k}$	**Quantity in the x, y, z directions**
$(\ )_{rms}$	**Root mean squared quantity**

Acronyms

CFD	**Computational Fluid Dynamics**
CFL	**Courant Friedrichs Lewy (Courant Number)**
DNS	**Direct Numerical Simulation**
DMP	**Distributed Memory Parallel processing**
LES	**Large Eddy Simulation**
LGRSTM	**Launder-Gibson Reynolds-Averaged Stress Turbulence Model**
LHS	**Left Hand Side of equation**
MPI	**Message Passing Interface**
RANS	**Reynolds-Averaged Navier-Stokes equations**
RAS	**Reynolds-Averaged Stress model**
RHS	**Right Hand Side of equation**
S-A	**Spalart –Allmaras turbulence model**
SGS	**Sub-Grid Scale**
SMP	**Shared Memory Parallel processing**
SST	**Shear Stress Transport turbulence model**
TKE	**Turbulent Kinetic Energy**

Chapter 1: Introduction

1.1. Purpose of the Research

Free and bounded mixing layers, as a fundamental type of shear flows in fluids engineering, are declared by different authors as a means to evaluate distinctive aspects of laminar-turbulent mechanisms of fluid mixing. Furthermore, these types of flows are frequently seen in downstream regions of turbo-machinery equipments such as compressors, turbines: mixing layers form at the trailing edges of thin blades and their effect on the performance of the next row of blades is of engineering concern. Depending on fluid flow properties as well as inflow conditions, a variety of mixing layer features such as symmetry or asymmetry, self-preservation, and oscillation of the core layers are displayed (Akhtar, 2010). Free mixing layers past wedges or corners are relatively unaffected by walls spreading in the streamwise direction. Thus, velocity and pressure gradients in these flows - that are created due to upstream boundary conditions - are smoothed out by viscous diffusion and convective deceleration (Wiecek and Mehta, 1998). Figure 1 displays a typical 2D mixing layer generated behind a small flat plate in the experimental study of Lasheras and Choi (1988).

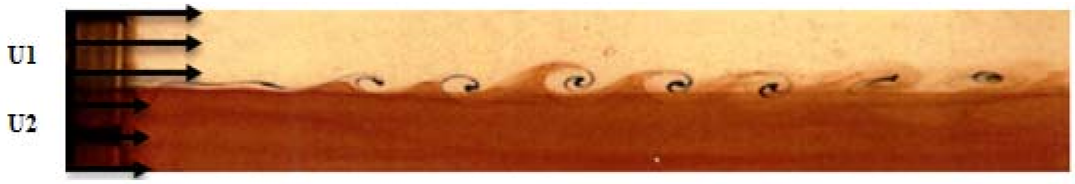

Fig. 1: Streamwise evolution of a 2D mixing layer behind the flat plate - vortex rollup (Lasheras and Choi, 1988)

Early investigations of steady incompressible laminar and turbulent mixing layers behind the splitter flat plate show that the flow just downstream of the plate is developing and non-self-similar. Further downstream, wavy-type vortex structures decay and the velocity profile between the upper and lower flows is smoothed out turning into an S-shaped free shear layer at the interface of the two streams (White, 2006, pp. 215-236). Although this is regarded as the general behavior of the 2D and 3D mixing layers, turbulent mixing layers exhibit more complexities, due to coherent vortical structures.

Steady behavior of 2D two-stream flows can be generalized by using a Blasius-type similarity variable for each stream (Schlichting and Gersten, 2000). Moreover, as indicated in Do et al.’s study (2010), behavior of flow behind the flat plate even at relatively low and moderate Reynolds numbers often exhibits wavy-shape instabilities - Tollmien-Schlichting (T-S) waves. These instabilities, if triggered by imposing fluctuations, lead to formation of self-induced motions (noise) in turbulent flow regimes.

The difference between the developing laminar mixing layer and the developed turbulent mixing layer is clearly shown in an experiment of Ito et al. (2013). As indicated in Figure 2b, turbulent mixing increases in the streamwise direction causing the interface between the upper and lower streams to become distorted. This is in opposition to a developing laminar mixing layer (Figure 2a) in which corresponding zones of upper and lower streams are well-distinguished.

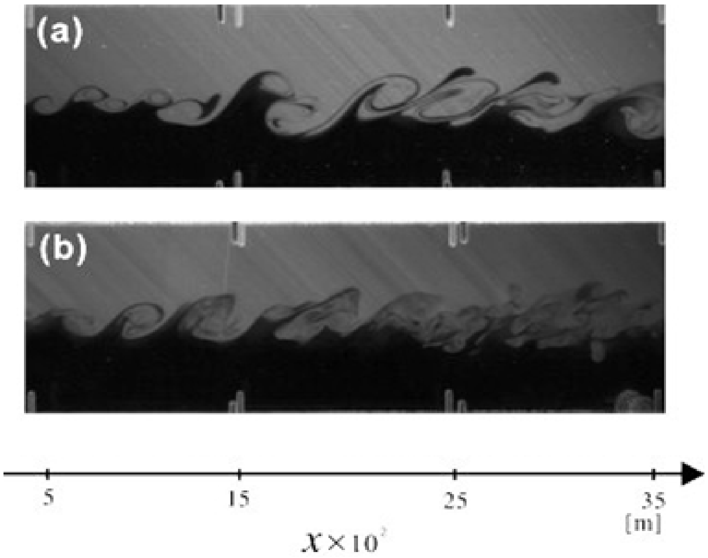

Fig. 2: Visualization of the mixing layer; a) developing laminar mixing layer, b) developed turbulent mixing layer (Ito, 2013)

Stability results for similar profiles over flat plates can be estimated from a universal graph correlating critical Reynolds number and a specified range of shape factors (Wazzan et al., 1979): with increasing shape factor, critical Reynolds number decreases and instability occurs earlier. Although there are some studies on the influence of upstream conditions on the developing behavior of mixing layers, the uncertainty in prediction of instability behavior of shear flows with small shape factors, such as the mixing layer of the present work, points to a need to examine the effects of inflow changes on the stability of downstream regions of these flows. Thus, it is one of the intentions of this study to investigate unsteady mixing layers behind a two-dimensional NACA0006 airfoil section with different inflow conditions to study their influence on the layers. Effects of changing the high-speed side free-stream temperature as well as Reynolds number on the developing behavior of the laminar mixing layer are illustrated.

There are considerable numbers of turbulent models developed for investigations of different types of turbulent flow physics. Most of these models, other than the well-known RANS equations, solve relevant equations by which turbulent properties, e.g. turbulent viscosity, turbulent kinetic energy, dissipation rate, are determined. Among these fast-growing models, Large Eddy Simulation (LES) and Direct Numerical Simulation (DNS), which provide more accurate computation procedures, have become more popular as computational resources grow. However, complexity of these methods including high demand on computing resources, time, and also the number of grid points to resolve all scales particularly in wall-bounded flows have always been a matter of arguments (Rumsey and Ying, 2002). All of these models have been used with a number of numerical schemes, such as lower and higher order finite volume/element and spectral methods, for the numerical simulation of turbulent shear layers. In the current study, LES and RANS-based models will be explored in detail to examine not only the behavior of the mixing layer behind the airfoil with different turbulence intensities and Reynolds numbers, but also reliability of these models against experimental investigations for such a flow.

Needless to say, shared and distributed memory parallel processing methods (SMP and DMP) have become popular in CFD studies because of their abilities to distribute the simulation domain into sub-domains and then solve the governing equations simultaneously on a number of processors defined for corresponding sub-domains. Using this kind of computation method has shown a sharp decrease in simulation time particularly for complicated fluid flow problems such as unsteady combustion, and three-dimensional turbulence. In order to perform parallel processing, the main code of each program should have the capability of distribution and also communication of data among the processors (Shang, 2014). In the present work, shared memory parallel processing in OpenFoam® is used for computations of laminar and turbulent mixing layers on generated three-dimensional hybrid meshes (OpenFoam, 2011-2015).

Although numerical studies of laminar-turbulent mixing layers behind flat plate splitters using structured grids are reported in the literature, (Milane, 2004, Lakehal et al., 2002), no significant study is accessible for far downstream mixing layers generated behind airfoils using a hybrid mesh. Moreover, as far as the author knows, effects of free-stream Reynolds number, temperature, and turbulence intensity on the behavior of laminar-turbulent mixing layers with low values of shape factors have not been addressed extensively in the literature. The current study uses the commercial ANSYS-Fluent® and the open-source OpenFoam® packages to numerically study and visualize the steady and unsteady behaviors of a bounded mixing layer behind a NACA0006 airfoil under different inflow conditions in both laminar and turbulent flow regimes. Three-dimensional behaviors of generated mixing layers are investigated by employing parallel computing in OpenFoam. Furthermore, results of the work are validated against experimental data for mixing layers behind flat plates found in previous works. In addition, Matlab® is utilized to validate the findings with an analytical solution.

1.2. Outline of the Thesis

The current study is organized in the five following major chapters: the review of the existing literature focused on the experimental and numerical studies of mixing layers as well as trailing edge vortices are provided in Chapter 2. The governing equations of laminar and turbulent flows, numerical schemes, and computation procedures are illustrated in the Chapter 3. Development of the mesh by using different grid types as well as setting the boundary conditions are discussed in Chapter 4. In Chapter 5, results of the simulations of steady and unsteady laminar mixing layers in 2D and 3D domains are presented. Moreover, the laminar mixing layer results behind the airfoil are compared with analytical and numerical solutions of the flat plate splitter mixing layers. Numerical simulations of steady and unsteady turbulent mixing layers in 2D and 3D domains, using different turbulence models, are presented in Chapter 6. In addition, accuracy of these models in comparison with the previous experimental studies is discussed. To sum up, a conclusion and a quick review of possible future studies with respect to the present work are given in Chapter 7.

Chapter 2: Literature Review

The steady unbounded laminar mixing layer generated behind a flat plate was studied analytically by Lock (1951) in terms of similarity variables. This flow is well-documented in the literature (White, 2006, pp. 215-236). Görtler (1957) presented an approximation of velocity profiles in an unbounded single-phase turbulent mixing layer. Confined turbulent mixing layers in channels behind splitter plates have been investigated experimentally by different authors including Mehta (1991) and Hollingsworth and Bourgogne (1995). The main focus of all these studies has been on the behavior of the mixing layers such as self-preservation, under different flow conditions, i.e. velocity ratios and turbulence intensities. A subject-based review of fundamental research on mixing layers in both laminar and turbulent flow regimes is provided in this section.

2.1. Stability and Self-similarity in Mixing Layers

Behavior of mixing layers in downstream regions is dependent on the shape of the splitter, which changes streamline curvatures. Furthermore, stability of mixing layers varies based on the momentum difference between high and low-speed sides (Plesniak and Johnston, 1988). Laminar shear layers become unstable above a definite critical Reynolds number where disturbances generated in the flow are amplified uncontrollably.

Primary works of Wazzan et al. (1979) and Arnal (1984) on stability analysis over a range of velocity profiles including the plane wake, Falkner-Skan wedge flows resulted in a universal plot: as seen in Figure 3, critical Reynolds number decreases with increase in shape factor leading instability to start earlier in the flow.

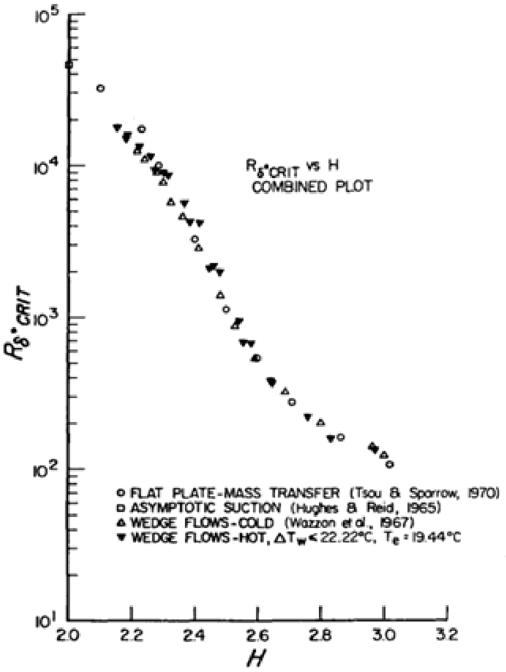

Fig. 3: The universal curve of Wazzan et al. (1979) correlates critical Reynolds number to shape factor

Hughes and Reid (1965) proposed an expression that relates the critical Reynolds number to free-stream velocity profile and displacement thickness. In addition, Reshotko (1987) showed in his experiment that for flows with temperature dependent properties, the stability of the boundary layer is enhanced by imposing more negative pressure gradients, $\frac{dp}{dx} < 0$; this is analogous to cooling the wall, meaning $\frac{dT}{dx} > 0$, in problems where gas flows over an impermeable wall.

Figure 4 depicts the self-similarity of turbulent fluctuations (Reynolds stresses) and velocity profiles achieved in the two-stream mixing layer of Mehta (1991) with initial low streamwise turbulence intensity in the range of 0.1-0.2%. It is observed that the distance required for velocity profiles to fully develop and show self-preservation is increased if higher velocity ratios (low-speed side to high-speed side) are applied. Thus, mixing layers with higher velocity ratio need more streamwise distance to exhibit full self-preservation. This is basically attributed to the lasting effect of the splitter wake interacting with the mixing layer, and also less stability of the layers due to higher critical Reynolds numbers. This might lead turbulent quantities as well as mean velocities measured after occurrence of self-similarity, to not be dependent on initial conditions, provided that inflow turbulence levels in the computational domain (or wind tunnel in the experimental studies) are low enough, $\frac{u'}{U} < 0.2\ \%$ (Oster and Wygnanski, 1982). Such a behavior consequently leads to an increase in peak Reynolds stresses. Also included in this study, are longitudinal distributions of peak Reynolds stresses: at the given velocity ratio, it is shown that the peaks do not change, particularly through the downstream regions. This is mainly because of counterbalancing of the wake behind the splitter that affects the upstream of the mixing layer and is slowly washed out by development of the layer in downstream regions.

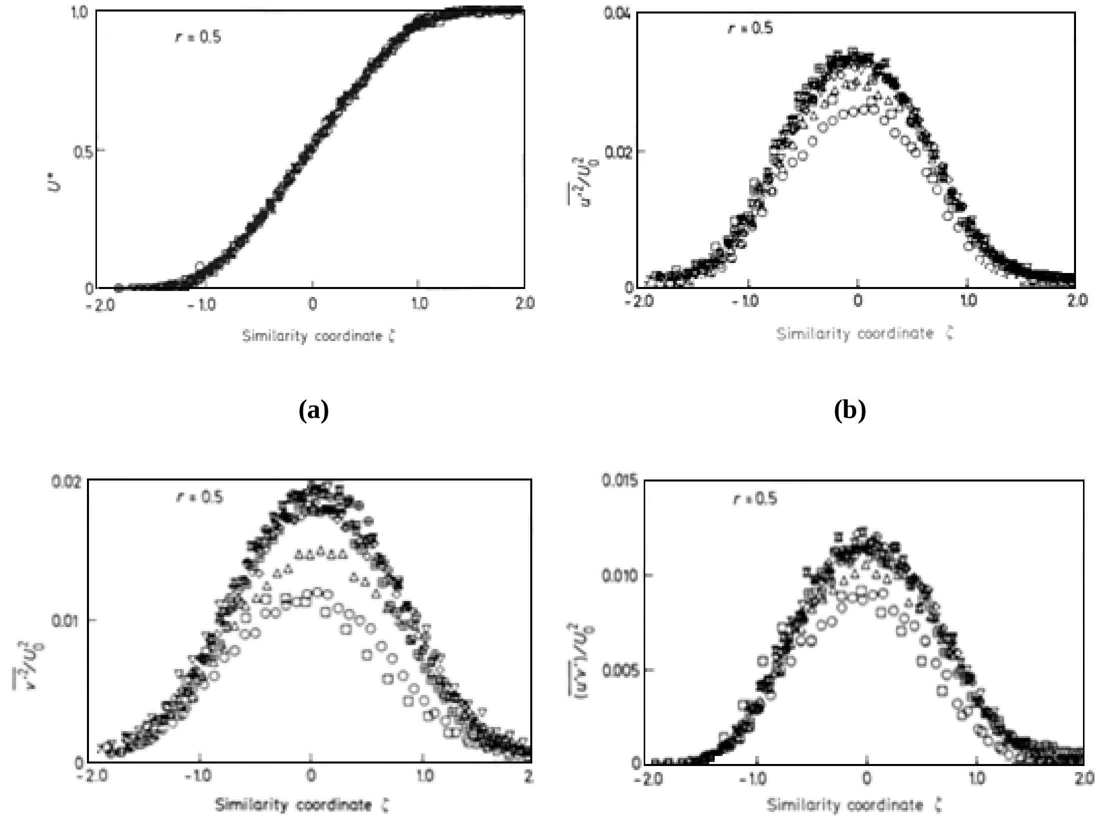

(a) **(b)**

(c) **(d)**

Fig. 4: Self-similarity of profiles in the experiment of Mehta (1991) - low-intensity flow, velocity ratio of 0.5 (low-speed side to high-speed side); a) mean velocity profiles, b) mean-square streamwise normal stress, c) mean-square transverse normal stress, d) mean-square Reynolds primary shear stress.

Although in the case of two-stream mixing layers, the distance needed for velocity profiles to exhibit self-similarity is not confirmed to follow any particular formulation, it is basically dependent on the physics of the flow (White, 2006, pp. 69-73, 406-454). Moreover, in a study of Mehta and Westphal (1986) it is seen that generally two-stream mixing layers reach self-preservation in a shorter distance compared to single-stream flows. Nevertheless, the authors do not comment on the comparison of stability for these two flows. Note that, in their experiment, the initial boundary layer was tripped so that the spanwise variations of turbulence quantities, formed by the streamwise vortical structures being in transition state, are minimized.

In a fundamental study of Townsend (1976), a relation between maximum shear stress and boundary layer growth rate in the governing equations of 2D mixing layers is presented, showing self-similarity at sufficiently high Reynolds number and large streamwise development distance. Furthermore, the experiment of Mehta and Westphal (1986) showed that self-preservation of the velocity profiles in turbulent mixing layers behind a flat plate is guaranteed if mean velocity and Reynolds stress profiles exhibit similarity and also if linear growth of corresponding thicknesses (displacement and momentum) is observed within the domain. It is worthwhile to mention that the self-preserving region can be correspondingly defined as the area in which momentum thickness represents linear growth (Milane, 2004).

2.2. Second Moment Terms in Developing Mixing Layers

Mixing layers contain two-dimensional structures at the beginning of their development. Once the layers develop, side-by-side vortices tend to stick to each other and form well-known large vortices (pairing). With increase in the Re number, these vortices are aligned in the streamwise direction (ribs) and developed flow becomes three-dimensional and consequently fully-turbulent. This initially developing region has considerable influence on the following developed turbulent mixing layer (Westerweel et al., 2009)

In an experiment done by Ito et al. (2013), momentum transfer in developing (transition stage) and developed turbulent mixing layers has been investigated. Results show that mean velocity gradients, $\frac{\partial \bar{u}}{\partial y}$, are steeper in the developed mixing layer compared to the developing mixing layer. Therefore, larger streamwise fluctuations are expected in the former case. This behavior can be violated with regard to Reynolds shear stress magnitudes. The main reason for this contradiction might be due to negative production of turbulent momentum at some small scales which are not stimulated enough to have the rollup frequency. It is also pointed out that in this experiment, the turbulent Reynolds stresses are assumed to be generated mainly by a production term, i.e. $(\overline{v'^2}\frac{\partial \bar{u}}{\partial y})$ in the corresponding RANS equations.

Counter-gradient diffusion ($\overline{u'v'} > 0$) of momentum at relatively small-medium eddy scales in the developing transient mixing layer is also reported in the experiment of Ito et al. (2013). This implies that the production term in the corresponding momentum equation of the developing mixing layer is larger than that in the developed one. However, after development of the mixing layer to turbulent flow, momentum transfer becomes positive mostly at small and large scales. This positivity is spread through all the scales once the mixing layer becomes fully turbulent. Such a behavior was also observed in the experiment of Bell and Mehta (1990): smaller Reynolds shear stresses are present in the tripped (developed) mixing layer than those in the un-tripped (developing) one. Velocity defects due to the presence of the splitter plate in the streamwise direction are estimated to have the major influence on this behavior.

2.3. Development of Turbulent Mixing Layers in Highly Turbulent Environments

Highly turbulent mixing layers, mostly seen in gas turbines or combustion chambers, have shown high levels of velocity fluctuations, namely 20% and above (Koutmos and McGuirk, 1989). The highly turbulent atmosphere leads to an increase in the level of heat transfer rate and skin friction. This rate of increase is predicted to be 20-50% for a medium range of turbulence intensities (10% or less) and more for higher levels of turbulence intensity (Maciejewski and Moffat, 1989). Corresponding experimental findings for such a turbulent flow field report even higher numbers than those found based on boundary layer theories (Dunn et al., 1985). Similarly, in the case of grid-generated turbulent mixing layers, which mostly represent isotropic turbulence in low intensities, increases in heat transfer and skin friction are indicated (Johnson and Johnston, 1989). However, these types of turbulent mixing layers decay more quickly and turbulent structures (secondary structures) are not continuously reproduced in them.

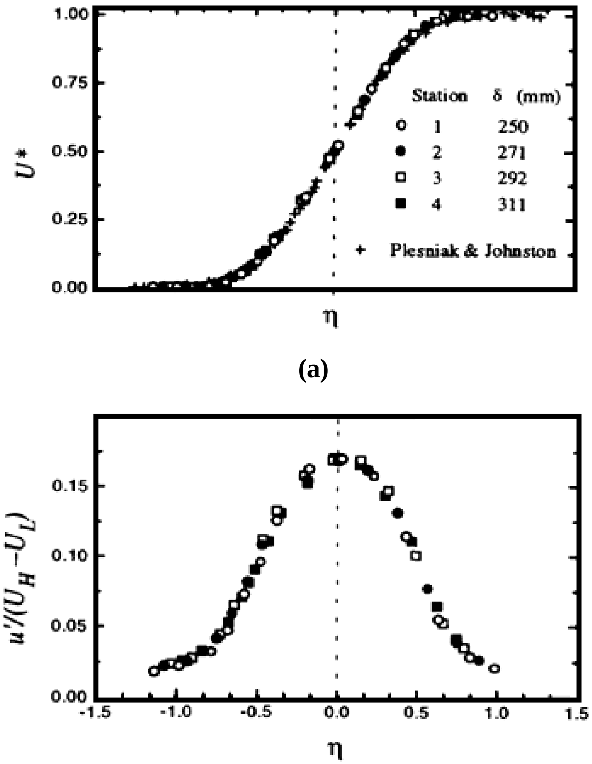

(a)

(b)

Fig. 5: Mixing layer streamwise distributions in the experiment of Hollingsworth and Bourgogne (1995) - low-intensity turbulence, velocity ratio of 2.5; a) mean velocity profiles, b) root-mean-square streamwise normal Reynolds stress

Basically, triggering turbulent flows into higher levels of turbulence intensity makes all turbulent scales become stronger, whereas the mean velocity profiles tend to decrease. This causes the mean streamwise profiles, in particular, to become less spatially uniform, and also leads free-stream turbulence intensity to decay 30-50% in the streamwise direction (Thole, 1992). Such a complex behavior is estimated to be due to the development of anisotropy as well as secondary vortical structures and three-dimensionality (Hollingsworth and Bourgogne, 1995).

In the experimental study of Hollingsworth and Bourgogne (1995), a two-stream mixing layer with a fixed velocity ratio of 2.5 between high-speed and low-speed sides is generated at the trailing edge of a flat plate and then exposed to a range of free-stream flows with low to high levels of uniform streamwise turbulence intensities, i.e. velocity fluctuations. Turbulent flow in this experiment does not show decay of turbulence intensity (dissipation) in contrast with conventional grid-generated turbulence. Also, three-dimensional effects with strong spanwise non-uniformity result in friction enhancement at the interface of the two streams.

Low turbulence intensity (0.5% or less) velocity profiles in the experiment of Hollingsworth and Bourgogne (1995) along with streamwise velocity fluctuations at four different stations, far away from the splitter plate wake, are provided in Figure 6. The mean velocity profile found in the analytical study of Plesniak and Johnston (1989) is also included in the figure for verification.

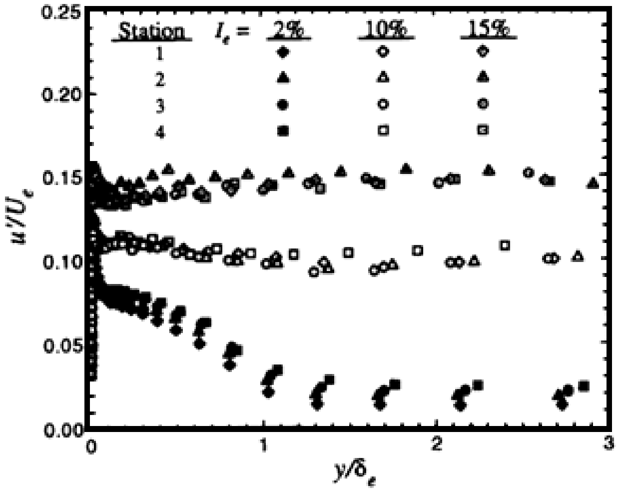

Fig. 6: Variation of dimensionless streamwise velocity fluctuations in transverse direction (Hollingsworth and Bourgogne, 1995)

Also provided in Figure 6 are variations of scaled turbulence intensity, $\frac{u^{'}}{U_{edge}}$, at four streamwise stations in the experiment of Hollingsworth and Bourgogne (1995). As indicated, in low-intensity environments there is a gradual decrease in the streamwise fluctuations toward the low-speed side within the mixing layer core, whereas almost no change is observed for medium and high turbulence intensities.

It should be noted that in this experiment, results are normalized based on the largest velocity achieved in the mixing layer velocity excess region. This choice also determines edges of the mixing layer such that boundary layer thickness can be estimated. However, because velocity at the edge of the mixing layer, U_{edge}, is usually 5-10% more than far-field velocity, U, values of I_{edge} are expected to be almost 2% less than values of free-stream turbulence intensity I (Hollingsworth and Bourgogne, 1995).

2.4. Vortical Structures and Three-Dimensionality

In practical low Re fluid dynamics, mixing layers basically expand from laminar flow regimes (developing mixing layer), through the transient state, and finally turn into turbulent mixing layers if the conditions of turbulence are met. In fully-developed mixing layers, as free-stream Reynolds number increases, these layers are found to generate three-dimensional structures, such as streamwise vortical structures as well as spanwise vortical rollers (Leboeuf and Mehta, 1996). Early investigations of turbulent mixing layers show that production of rollers, i.e., spanwise coherent structures, is accompanied by their pairing and thus considered as a determining criteron for mixing layer growth rate.

Streamwise vortices known as secondary structures have been visualized in plane mixing layer studies. These structures are initiated in the braid region, close to the trailing edge of the splitter, with the least amount of spanwise vortices, and then conquered by large-scale shear stress (Bernal and Roshko, 1986). The produced turbulent spots are concentrated at the beginning of the formation of the earliest spanwise structure pairings and accordingly create rows of streamwise counter-rotating pairs (Tung, 1992). It has also been observed that as principal spanwise rollers stretch, the counter-rotating pairs spread and connect remaining spanwise rollers (Metcalfe et al., 1987). However, as a result of formation of strain fields, the rollers are distorted and produce “cups” of spanwise vortices (Buell and Mansour, 1989).

Measurements of Bell and Mehta (1992) indicate that formation of secondary structures in the streamwise direction could be due to expansion of small-scale disturbances upstream of the mixing layer. Also, because of actual streamwise diffusion and dissipation, these vortices decay as they propagate toward downstream regions. Contours of mean-stream velocity in the experiment of Wiecek and Mehta (1998) on a plane mixing layer are seen in Figure 7. The figure depicts distortion of the vortices from the side view in the crosswise direction, thus representing three-dimensionality of the mixing layer. These distortions, in the form of sinusoidal "wrinkles", are basically due to momentum transfer among secondary structures (Leboeuf and Mehta, 1996). As a result, it is possible to say that the magnitudes of these distortions can be estimated by streamwise vortices strengths (Bell and Mehta, 1992). It should be noted that the wake region generated behind the splitters leads to spatial evolution of three-dimensionality and has direct effects on self-similarity of the velocity profiles further downstream (Weygandt and Mehta, 1995).

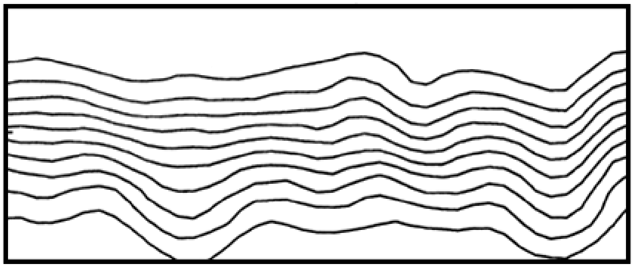

Fig. 7: Three-dimensionality: contours of mean streamwise velocity from the side view in the last station of measurement domain (Wiecek and Mehta, 1998).

Moreover, in the study of Wiecek and Mehta (1998) it is shown that for lower (less than one) velocity ratios (in which the velocity difference between the upper-side and lower-side increases), spanwise rollers are amplified more and accordingly braid region stretching is more distinctive compared to higher velocity ratios. In other words, the rate of amplification of initial disturbances increases as velocity ratio decreases. This kind of behavior leads the streamwise vortices to enlarge at further downstream regions; thus, their magnitudes decrease. Such a behavior is expected to be basically due to increase in the level of mixing, significantly in downstream regions, that improves tendency of the flow to earlier transition.

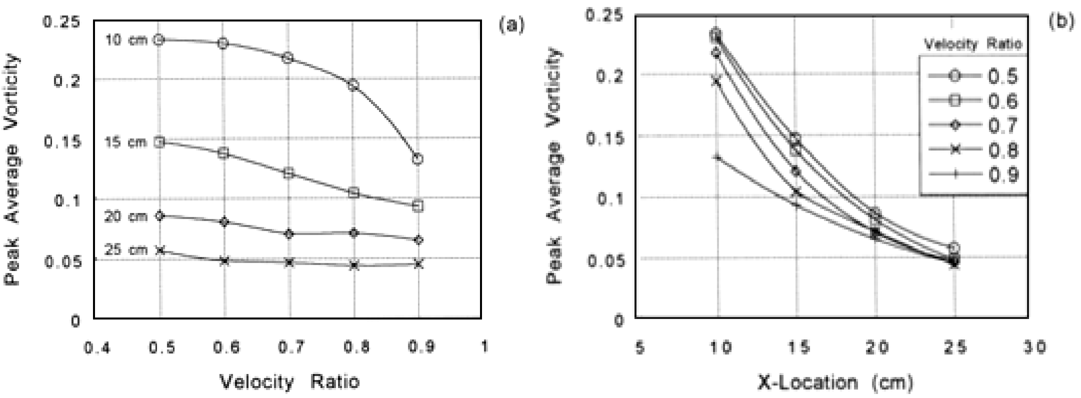

Fig. 8: Streamwise distribution of peak average vorticity: a) versus velocity ratio, b) versus streamwise location (Wiecek & Mehta, 1998)

Another important observation grasped from Figure 8 is that rate of decay of streamwise coherent structures can be approximated as a function of velocity ratio and streamwise location showing its highest value at the most upstream location and for the lowest velocity ratio (Leboeuf and Mehta, 1993).

Because of the lasting effect of the splitter wake, three-dimensional structures in the mixing layer remain dependent on the velocity difference (ratio) even after a long distance of development. This dependence is not negligible in the mixing layer near-field regions, but it decreases significantly downstream of the flow if the effects of the wake are neglected.

The changes of Reynolds stress local peaks in the crosswise direction basically represent varying spanwise reproduction mechanisms of turbulence (Figure 9). In addition to variation of streamwise shear strain, $\frac{\partial \bar{u}}{\partial y}$, in the crosswise direction, secondary spanwise flows along with their own distortions generate further gradients such as $\frac{\partial \bar{u}}{\partial z}$, $\frac{\partial \bar{v}}{\partial z}$, etc. which all lead to reproduction of turbulence in both spanwise and streamwise directions (Wiecek and Mehta, 1998).

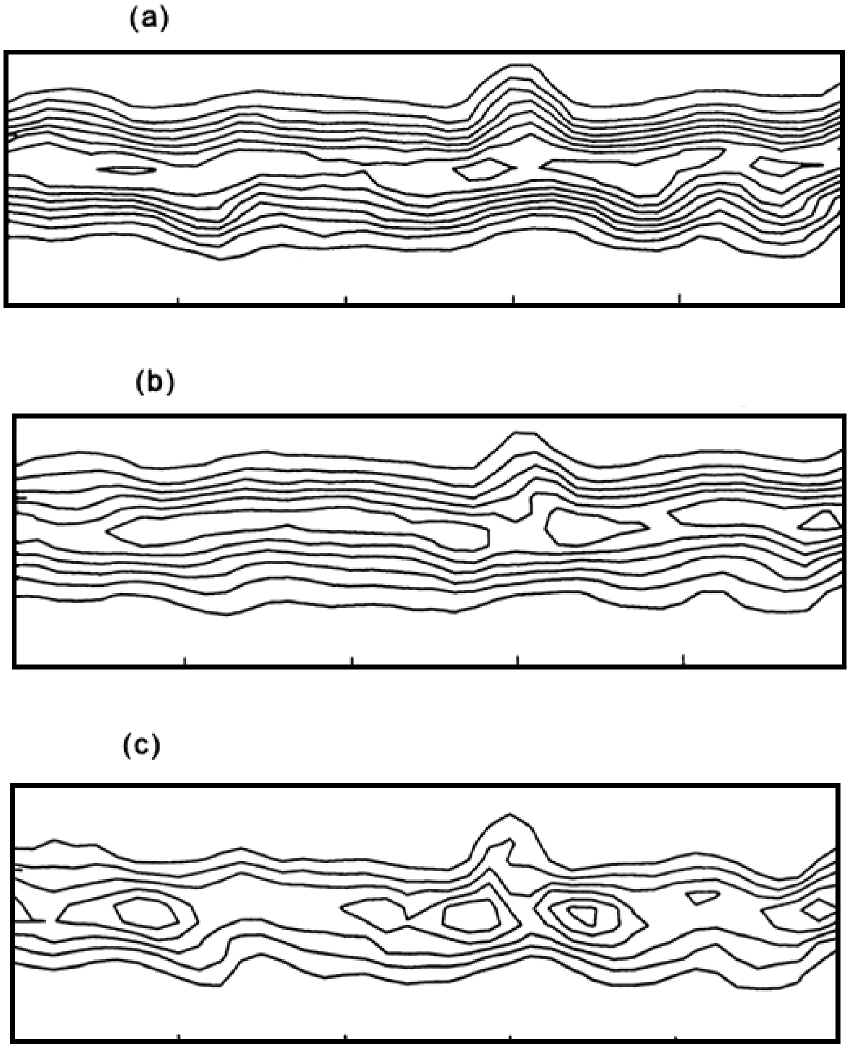

Fig. 9: Normalized Reynolds stresses distributions at x=15 cm, r=0.5 a) streamwise normal stress, $\frac{\overline{u'^2}}{U^2}$ b) transverse normal stress, $\frac{\overline{v'^2}}{U^2}$, c) covariance-Reynolds shear stress, $\frac{\overline{u'v'}}{U^2}$ (Wiecek and Mehta, 1998)

It is also notable that, there is a relation between mean streamwise vorticity and secondary covariance, i.e. $\overline{u'w'}$, as first proposed by Bell and Mehta (1992). As mentioned, in turbulent mixing layers, vortical structures generated in the streamwise direction are distorted in the spanwise direction; this basically results in generation of shear stress in spanwsie z direction, $\frac{\partial \bar{u}}{\partial z}$. The generated shear stress is added to normal stresses,$\overline{w'^2}$, along the centerline of the mixing layer and thus create $\overline{u'w'}$. It is also interesting that the rms values of $\overline{u'w'}$ are reduced with increasing velocity ratio of the low-speed side to high-speed side (Wiecek and Mehta, 1998). This is of course in accordance with reduction of peak rms values of streamwise vortices' strengths.

2.5. Airfoil Trailing Edge Vortices

High-vorticity flow behind an airfoil or wing leads to roll-up of the sheet of fluid such that vortical structures, i.e. wing trailing edge vortices, are formed.

Turbulence in wing trailing edge vortices is estimated to be due to three sources: 1) high-vorticity sheets behind the airfoil; which are able to exhibit higher levels of turbulence after they roll up. As mentioned, this leads to formation of vortical structures; 2) turbulence observed in the mean streamwise flow directs middle-small scales to shape larger scale structures around the core sheet of the flow; this causes an increase in the turbulent fluctuation; and 3) triggering the local instabilities (T-S waves) produces velocity fluctuations, i.e. turbulence, within the vortices (Pentelow, 2014).

Generated turbulence can affect the primary vortical structures which are dominated by hairpins (Brinkerhoff and Yaras, 2014). This effect will change the macroscopic shape of the former structures in a way that secondary hairpins are created. However, presence of turbulent inflow is required so that new structures can emerge. Such behavior has also been confirmed by the DNS study of Melander and Hussain (1993) that shows influence of a columnar vortex on a homogeneous turbulence field: small scale eddies present in the field are rearranged to make growing high-vorticity hairpin structures surround the initial vortex (3D vortical structures).

Understanding the behavior of wing trailing edge vortices can also be reached by study of the turbulent power spectra. As presented in Figure 10, Beninati and Marshall (2005) observed that there is a sharp decrease in energy of the turbulent structures (turbulent kinetic energy) at short wavelength fluctuations further downstream of the mixing layer.

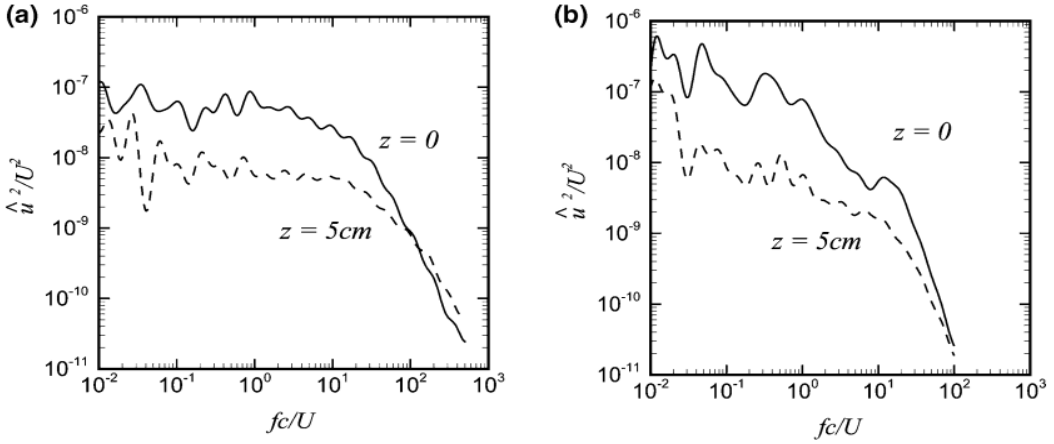

Fig. 10: Power spectra of streamwise velocity: normalized streamwise kinetic energy versus normalized wave number at z=0cm and z=5cm from the vortex core; a) 8, b) 25 chord lengths downstream of the airfoil trailing edge (Beninati and Marshall, 2005)

According to Figure 10, as frequency of the fluctuations increases, turbulent energy within the core of the vortices is conserved in such a way that dissipation (decay) of turbulence occurs apparently more in downstream layers. This can be demonstrated by how fluctuations behave: high frequency streamwise fluctuations are inhibited and damped by inherent stability of the vortex core sheet while low frequency ones convect through and beyond the core, experiencing the least change in corresponding wavelengths (Pentelow, 2014).

2.6. Numerical Simulations in Transitional to Turbulent Shear Layers

Numerical research on shear layers has been carried out along with experimental studies from time to time. Using spectral and higher order finite volume methods for laminar to transitional shear layers, and RANS - LES models for turbulent layers, simulations have become more popular for prediction of mixing layer behavior.

Lakehal et al. (2002) in their LES studies over 2D and 3D turbulent shear layers reported almost the same results for streamwise flow parameters in 2D and 3D simulations. However, the best result was found by using the Smagorinsky SGS model, collapsing well with experimental investigations of Roig et al. (1998). Akhtar (2010) used RANS-based simulations to show that spreading rates in a two-phase turbulent mixing layer are larger in comparison with single-phase mixing layer, even though dissimilar spreading rates were estimated by different RANS models. Among recent numerical research on turbulence, Brinkerhoff and Yaras (2014) used DNS to investigate reproduction mechanisms of coherent vortical structures (hairpin vortices) in a 3D rectangular channel. In this study, in order to generate the first turbulent spot, laminar flow in an assumed primary channel was triggered by a wall-normal jet once the flow was developed. Results of this simulation at a spanwise plane located close enough to the end of the channel, were mapped and set as inflow conditions for a second 3D rectangular channel. As the first turbulent spot convected with the flow, reproduced vortical hairpins were observed.

Furthermore, some recently proposed methods have tried to study turbulence in a Lagrangian-Eulerian frame. These methods, namely Particle-Source-In-Cell (PSI-Cell) and Vortex-In-Cell (VIC), in addition to having the same features as existing numerical schemes, address flow particle behavior, e.g. tracking of vortices. These types of numerical methods could reduce both numerical dissipation errors and computational time (Abdolhosseini and Milane, 2000). Using VIC methods, Milane (2004) studied LES of a spatially growing 2D mixing layer by employing the diffusion-velocity method for the vorticity equation along with the Smagorinsky sub-grid scale (SGS) model for turbulent viscosity. The study reveals that using the SGS model in the LES of 2D mixing layers based on the diffusion-velocity method results in a decrease in rms values of turbulence quantities such as fluctuations, and consequently in the momentum thickness growth rate. This is basically attributed to the dissipative nature of the SGS model, or equivalently eddy viscosity, which increases as time proceeds. Results of this study are also in good agreement with the experimental study of Masutani and Bowman (1986).

Chapter 3: Governing Equations and Numerical Schemes

3.1. Governing Equations

The non-linear Navier-Stokes equations in the case of laminar incompressible flow without considering gravity effects are given by (White, 2006, pp. 69-73, 406-454):

$$\nabla.\mathbf{u} = 0 \tag{1}$$

$$\rho\frac{D\mathbf{u}}{Dt} = -\nabla p + \mu\nabla^2\mathbf{u} \tag{2}$$

where $\mathbf{u} = (u, v, w)$ represents the components of velocity vector, p is static pressure, ρ is density, and μ is dynamic viscosity. The energy equation for laminar incompressible fluid flow with constant properties is given by:

$$\rho c_p\frac{DT}{Dt} = k_h\nabla^2 T \tag{3}$$

in which T is temperature, c_p is heat capacity at constant pressure, and k_h is thermal conductivity. Also, substantial derivative operator, $\frac{D}{Dt}$, is (White, 2006, pp. 59-74):

$$\frac{D}{Dt} = \frac{\partial}{\partial t} + (\mathbf{u}.\nabla). \tag{4}$$

Displacement thickness as well as momentum thickness and shape factor are defined as:

$$\delta^* = \int_0^\delta (1 - \frac{u}{U_\infty})dy \tag{5}$$

$$\theta = \int_0^\delta \frac{u}{U_\infty}(1 - \frac{u}{U_\infty})dy \tag{6}$$

$$H = \frac{\delta^*}{\theta} \tag{7}$$

where δ is the boundary layer thickness and U_∞ is the free-stream velocity.

By decomposition of instantaneous quantities, e.g. u, into mean and fluctuation terms for all the components:

$$u = \bar{u} + u^{'} \tag{8}$$

in which the mean component $\bar{u}$ is found by time averaging of streamwise velocity u:

$$\bar{u} = \frac{1}{N}\int_{t}^{t+N} u dt \tag{9}$$

Reynolds-Averaged equations for turbulent mean quantities are found as:

$$\nabla . \bar{\mathbf{u}} = 0 \tag{10}$$

$$\rho \frac{D\bar{\mathbf{u}}}{Dt} = -\nabla\bar{p} + \nabla . \tau_{ij} \tag{11}$$

where turbulent inertia stress, τ_{ij} , is given by:

$$\tau_{ij} = \mu\left(\frac{\partial u_i}{\partial x_j} + \frac{\partial u_j}{\partial x_i}\right) - \rho\overline{u_i^{'} u_j^{'}} \, . \tag{12}$$

The right hand side of Equation (12) accounts for laminar shear stress and turbulent stress tensors in the case of Newtonian fluids.

By using the same procedure, a mean energy equation for turbulent flows is found as:

$$\rho c_p \frac{D\bar{T}}{Dt} = -\frac{\partial}{\partial x_i}(q_i) + \bar{\varphi} \tag{13}$$

in which the turbulent dissipation function, $\bar{\varphi}$, is:

$$\bar{\varphi} = \frac{\mu}{2}\overline{\left(\frac{\partial \bar{u}_i}{\partial x_j} + \frac{\partial u_i^{'}}{\partial x_j} + \frac{\partial \bar{u}_j}{\partial x_i} + \frac{\partial u_j^{'}}{\partial x_i}\right)^2} \, . \tag{14}$$

Total heat flux, q_i, that includes laminar flux and turbulent flux terms, is defined as:

$$q_i = -k_h \frac{\partial \bar{T}}{\partial x_i} + \rho c_p \overline{u_i' T'} . \tag{15}$$

Note that all of the above equations can be generalized for 3D cases by using the same procedures.

The corresponding growth parameters in the case of turbulent flows become:

$$\delta^* = \int_0^\delta (1 - \frac{\bar{u}}{U_\infty}) dy \tag{16}$$

$$\theta = \int_0^\delta \frac{\bar{u}}{U_\infty} (1 - \frac{\bar{u}}{U_\infty}) dy \tag{17}$$

$$H = \frac{\delta^*}{\theta} . \tag{18}$$

The turbulent kinetic energy (TKE) of the fluctuations in terms of mean-square values is defined as:

$$k = \frac{1}{2} \left(\overline{u'^2} + \overline{v'^2} + \overline{w'^2} \right) . \tag{19}$$

As seen in Equation (19), k is in proportion with the summation of normal Reynolds stresses. Thus, the conservation equation for turbulent kinetic energy k can be found by use of a mechanical energy equation (White, 2006, pp. 69-73, 406-454). So, conservation of turbulent kinetic energy is expressed as:

$$\frac{Dk}{Dt} = -\frac{\partial}{\partial x_i} \left[\overline{u_i' \left(\frac{1}{2} u_j' u_j' + \frac{p'}{\rho} \right)} \right] - \overline{u_i' u_j'} \frac{\partial \bar{u}_j}{\partial x_i} + \frac{\partial}{\partial x_i} \left[\overline{\nu u_j' \left(\frac{\partial u_i'}{\partial x_j} + \frac{\partial u_j'}{\partial x_i} \right)} \right] - \nu \overline{\frac{\partial u_j'}{\partial x_i} \left(\frac{\partial u_i'}{\partial x_j} + \frac{\partial u_j'}{\partial x_i} \right)} \tag{20}$$

where the right hand side of the equations includes convective diffusion, turbulence production, turbulent shear stress work, and turbulent viscous dissipation, respectively. Note that ν is the kinematic viscosity.

The turbulent shear stress term, namely covariance or Reynolds stress, presented in turbulent inertia stress Equation (12), is regarded as the main parameter investigated in turbulence modeling. The corresponding conservation equation for this term can be written as follows:

$$\frac{D\overline{u_i^{'}u_j^{'}}}{Dt} = -\left[\overline{u_j^{'}u_k^{'}}\frac{\partial \overline{u}_i}{\partial x_k} + \overline{u_i^{'}u_k^{'}}\frac{\partial \overline{u}_j}{\partial x_k}\right] - 2\nu\,\overline{\frac{\partial u_i^{'}}{\partial x_k}\frac{\partial u_j^{'}}{\partial x_k}} + \overline{\frac{p'}{\rho}\left(\frac{\partial u_i^{'}}{\partial x_j} + \frac{\partial u_j^{'}}{\partial x_i}\right)} \\ - \frac{\partial}{\partial x_k}\left[\overline{u_i^{'}u_j^{'}u_k^{'}} - \nu\frac{\partial \overline{u_i^{'}u_j^{'}}}{\partial x_k} + \overline{\frac{p'}{\rho}(\delta_{jk}\,u_i^{'} + \delta_{ik}\,u_j^{'})}\right]. \tag{21}$$

According to this equation, temporal variation of Reynolds stress is equal to the sum of production of stress, turbulence dissipation, pressure-strain effects, and turbulence diffusion. Note that, δ_{ij} , δ_{jk}, δ_{ki} are Kronecker deltas.

In two-equation or higher order turbulence models, the turbulent kinetic energy equation is coupled with ϵ, ω, k_l transport equations as well as continuity and momentum transport equations. In the case of dissipation rate parameter, ϵ, the following equation:

$$\frac{\partial}{\partial t}(\rho\epsilon) + \frac{\partial}{\partial x_i}(\rho\epsilon u_i) = \frac{\partial}{\partial x_j}\left[\left(\mu + \frac{\mu_t}{\sigma_\epsilon}\right)\frac{\partial \epsilon}{\partial x_j}\right] + C_{1\epsilon}\frac{\epsilon}{k}G_k - C_{2\epsilon}\rho\frac{\epsilon^2}{k} + S_\epsilon \tag{22}$$

is used with $C_{1\epsilon}$, $C_{2\epsilon}$, $C_{3\epsilon}$ as constant values. Also, G_k is the turbulence production term due to mean velocity gradients; σ_ϵ represents turbulent Prandtl number for dissipation rate, and S_ϵ is the source term. In ANSYS-Fluent, this equation is coupled with the rewritten turbulent kinetic energy equation of Launder and Spalding (1972), who first developed the $k - \epsilon$ model (ANSYS-Fluent, 2014).

In the case of the three-equation laminar kinetic energy (k_l) model, the conservation equation for k_l is written as:

$$\frac{Dk_l}{Dt} = P_{k_l} - R - R_{NAT} - D_l + \frac{\partial}{\partial x_j}\left[\nu \frac{\partial k_l}{\partial x_j}\right] \tag{23}$$

in which P_{k_l} is the laminar kinetic energy produced by large eddies, R reflects the effects of the streamwise fluctuations on the turbulence field in the case of bypass transition, R_{NAT} is the turbulence production term due to natural transition, D_l is the dissipation term, and the last term corresponds to viscous diffusion of laminar kinetic energy (ANSYS-Fluent, 2014). It is noted that, in derivation of this model, the turbulent kinetic energy equation is modified and also a new transport equation for the inverse turbulent time scale parameter is added to the system of equations. This parameter eliminates the effects of the wake on the velocity profiles and also reduces the intermittency in the outer layer region (ANSYS-Fluent, 2014).

The transition SST model was developed based on a modified $k - \omega$ model by adding two further transport equations for turbulence intermittency, γ, and momentum thickness Reynolds number at transition, $\widetilde{Re}_{\theta_t}$, as follows:

$$\frac{\partial}{\partial t}(\rho\gamma) + \frac{\partial}{\partial x_j}(\rho\gamma u_j) = \frac{\partial}{\partial x_j}\left[\left(\mu + \frac{\mu_t}{\sigma_\gamma}\right)\frac{\partial \gamma}{\partial x_j}\right] + P_{\gamma 1} - E_{\gamma 1} + P_{\gamma 2} - E_{\gamma 2} \tag{24}$$

and:

$$\frac{\partial}{\partial t}\left(\rho\widetilde{Re}_{\theta_t}\right) + \frac{\partial}{\partial x_j}\left(\rho u_j \widetilde{Re}_{\theta_t}\right) = \frac{\partial}{\partial x_j}\left[\sigma_{\theta_t}(\mu + \mu_t)\frac{\partial \widetilde{Re}_{\theta_t}}{\partial x_j}\right] + P_{\theta_t} \tag{25}$$

which are almost the same as equations presented before for two-equation RANS-based models. However, $P_{\gamma 1}$, $E_{\gamma 1}$ in Equation (24) , and P_{θ_t} in Equation (25) are transition source terms whereas $P_{\gamma 2}$, $E_{\gamma 2}$ represent relaminarization sources defined in terms of experimental correlations (ANSYS-Fluent, 2014).

The main advantage of this model is utilization of empirical correlations in the derivation of transport equations that control the onset of natural transition as well as the length of the transition region in separated flows based on experimental results.

Reynolds stresses in turbulent flows are modeled based on using a second order closure approach in RANS-based equations. Algebraic stress models (ASM) in the form of partial differential equations (PDE) can also be used in modeling of these stresses (White, 2006, pp. 398-485).

As reviewed by Kline et al. (1982), the general Reynolds stress equation can be given as:

$$\begin{aligned}\frac{D(\overline{u_i^{'}u_j^{'}})}{Dt} = &-\frac{\partial}{\partial x_k}\left(\overline{u_i^{'}u_j^{'}u_k^{'}} + \frac{\overline{p'u_i^{'}}}{\rho}\delta_{jk} + \frac{\overline{p'u_j^{'}}}{\rho}\delta_{ki}\right) - \left[\overline{u_i^{'}u_k^{'}}\frac{\partial \overline{u}_j}{\partial x_k} + \overline{u_j^{'}u_k^{'}}\frac{\partial \overline{u}_i}{\partial x_k}\right] \\ &+ \overline{\frac{p'}{\rho}\left(\frac{\partial u_i^{'}}{\partial x_j} + \frac{\partial u_j^{'}}{\partial x_i}\right)} + 2\nu\overline{\frac{\partial u_i^{'}}{\partial x_k}\frac{\partial u_j^{'}}{\partial x_k}}\end{aligned} \tag{26}$$

where the terms defined on the right hand side of the equation are transport of the turbulence, turbulence production, pressure-strain effects, and viscous dissipation, respectively. It is noted that different correlations either in terms of experiments or DNS studies have been proposed to cover these terms, e.g. the Moin and Mahesh (1998) model for the turbulence transport term and the Wilcox-Rubesin (1980) model for pressure-strain term.

In ANSYS-Fluent, the Reynolds stress turbulence model (RSM) transport equations are coupled with continuity, momentum, energy, and dissipation/specific dissipation rate equations. Also, turbulent shear stresses are computed directly by using appropriate numerical schemes which eliminates solving the eddy-viscosity equation separately. Thus, the corresponding equations are given by:

$$\begin{aligned}&\frac{\partial}{\partial t}\left(\rho\overline{u'_i u'_j}\right) + \frac{\partial}{\partial x_k}\left(\rho u_k \overline{u'_i u'_j}\right) \\ &\quad = -\frac{\partial}{\partial x_k}\left[\rho\overline{u'_i u'_j u'_k} + \overline{p'\left(\delta_{kj}u'_i + \delta_{ik}u'_j\right)}\right] + \frac{\partial}{\partial x_k}\left[\mu\frac{\partial}{\partial x_k}\left(\overline{u'_i u'_j}\right)\right] \\ &\quad\quad - \rho\left(\overline{u'_i u'_k}\frac{\partial u_j}{\partial x_k} + \overline{u'_j u'_k}\frac{\partial u_i}{\partial x_k}\right) + \overline{p'\left(\frac{\partial u'_i}{\partial x_j} + \frac{\partial u'_j}{\partial x_i}\right)} - 2\mu\overline{\frac{\partial u'_i}{\partial x_k}\frac{\partial u'_j}{\partial x_k}}\ .\end{aligned} \tag{27}$$

In Equation (27), the second term on the left hand side represents turbulent convection; and terms on the right hand side are: turbulent diffusion, viscous diffusion, production of stress, pressure-strain correlation, and turbulence dissipation, respectively. In addition to changes applied to kinetic energy and turbulent viscosity equations, there are some terms in Equation (27), including turbulent diffusion, pressure-strain, and dissipation, which are also required to be modeled to close the system of governing equations. It is noted that depending on the type of the turbulent flow, new production and diffusion terms due to swirling (rotation of vortices), and gravity are added to Equation (27) (ANSYS-Fluent, 2014).

It should be mentioned that in OpenFoam, new turbulence models are derived based on modifications applied to RANS-based models. As an example, the LGRSTM (OpenFoam, 2011-2015) model has been developed in terms of corrections in corresponding Reynolds shear stress and turbulent viscosity equations that are also used in ANSYS-Fluent.

In a simple 2D case, the primary shear stress (covariance), $\rho\overline{u_i'u_j'}$, can be approximated by using the Boussinesq assumption that relates covariance to shear strain (gradient diffusion approximation):

$$\rho\overline{u_i'u_j'} = \mu_t \frac{\partial \bar{u}}{\partial y} \tag{28}$$

with μ_t is defined as eddy viscosity. This equation is mostly used in one-equation RANS models and also has been a basis for developing new eddy viscosity definitions in higher-accuracy turbulence models. It is noted that there are some other models for eddy viscosity developed in terms of inner/outer boundary layer concepts (White, 2006, pp. 398-485). For instance, the Baldwin-Lomax (1978) model is one of these models derived for μ_t in the outer layer.

3.2. Initial Conditions for Turbulent Parameters

Turbulence intensity is defined as the ratio of rms value of fluctuations to mean streamwise velocity:

$$I = \frac{u'_{rms}}{\bar{u}}. \tag{29}$$

In the present work, a range of intensities including 2%, 10% and 15% are considered in simulations of turbulent mixing layers. Evidently in the inflow turbulence intensity range of 10-15%, the mixing layer behaves as a fully-developed turbulent flow (Hollingsworth and Bourgogne, 1995). It is also assumed that the mixing layer is treated as an equilibrium turbulent flow, meaning that the pressure gradient across the mixing layer is assumed to be constant. This assumption is related to the pressure gradient parameter defined by White (2006, pp. 69-73, 406-454).

In addition to free-stream velocity and turbulence intensity, the turbulent length scale was used as an independent turbulent initial input. These three parameters are used in determining initial turbulent quantities, e.g. k, ϵ, etc., through the transport equations.

Assuming a fully developed turbulent mixing layer in the channel, the turbulent length scale size (eddy size) in the present work was found by using the following approximation (ANSYS-Fluent, 2014):

$$l = 0.07D_h \tag{30}$$

where D_h represents the hydraulic diameter. In the case of a 3D channel with a span of 1m, the length scale of 1.981m, based on the dimension of the experimental study, was set as one of the initial values to run the simulations. Likewise, choosing this value in the case of the 2D mixing layers gave reasonable results that collapse well with reference data. However, in the latter case, a span of 1cm was also tested as the initial guess; the results were not reasonable. It is also noted that there are several turbulence length scales defined by different authors. These definitions are basically dependent on the streamwise dissipation of fluctuations (turbulence intensity); for instance in the case of high-intensity turbulence, Ames and Moffat (1990) developed a descriptive turbulence length scale Reynolds number (TLR) which concentrates on friction coefficient enhancement.

Initial values of other turbulent parameters such as k and ϵ are calculated in terms of turbulence intensity and other independent initial values mentioned earlier. These quantities are correlated by using the following equations (ANSYS-Fluent, 2014):

$$k = 1.5(\bar{u}I)^2 \tag{31}$$

$$\epsilon = C_\mu^{0.75} \frac{k^{1.5}}{l} \tag{32}$$

where C_μ in Equation (32) is a constant determined by experiments conducted for turbulent flows. Also, in decaying turbulent flows simulated in two and higher order models, as in the present study, dissipation rate as well as turbulent viscosity can be approximated by:

$$\epsilon \cong U_\infty \frac{dk}{dx} \tag{33}$$

$$\mu_t = \rho C_\mu \frac{k^2}{\epsilon} \;. \tag{34}$$

In addition, the specific dissipation rate:

$$\omega = \frac{k^{0.5}}{C_\mu^{0.25} l} \tag{35}$$

is used to determine the turbulent quantities based on the initial inputs of I, U_∞, and l. It is noted that in the case of simulation of turbulence using the SST model, initial intermittency was assumed as 0.1.

3.3. Numerical Schemes

2D simulations in the present work are produced with ANSYS-Fluent® (V15.0). The governing equations of the flow are solved implicitly based on a finite-volume approach by using a pressure-based solver. In order to minimize the artificial diffusion, a second order upwind method was used for discretization of the momentum equations. Applying a

3rd order MUSCL method did not improve the accuracy of the final results significantly. The pressure field is also interpolated by a standard scheme. The computed pressure field is then coupled to the velocity field through a coupling algorithm (“Coupled” method) in which continuity and momentum equations are solved simultaneously through discretization of pressure gradient and mass flux terms in the momentum equation. The Green-Gauss Node-Based method was used to calculate the derivative terms in the governing equations for improved accuracy.

The open-source package, OpenFoam® (V2.3.0), is used for simulations of 3D mixing layers. Generally, in OpenFoam, the unsteady Navier-Stokes equations are discretized and solved explicitly by use of standard Gaussian finite volume integration employing different solvers based on the physics of the flow. In this study, “pisoFoam” and “simpleFoam” were chosen as appropriate solvers for unsteady and steady simulations in laminar-turbulent regimes, respectively. The BuoyantBoussinesqPimpleFoam (BBPF) solver was used to solve the unsteady energy equation (in the 2D laminar mixing layer). As summarized in Table I, 2nd order schemes for discertization of temporal-spatial terms were implemented in each case. Also, Gaussian linear interpolation and explicit correction (“Corrected” method) surface normal gradient (Sn Gradient) schemes were used in discretization of the governing equations. Note that, in the simpleFoam solver, pressure-velocity coupling is achieved by using the SIMPLE algorithm, whereas the PISO is used in the pisoFoam unsteady solver. In the PISO algorithm, operators in the governing equations are divided into predictor steps, resolved implicitly, and corrector steps, resolved explicitly. At each time step, velocity (and temperature) field is predicted at first and then old pressure and velocity fields are corrected. The PISO loop method is more suitable for transient flows (resolved within small time steps) since it reduces the non-linear effects of velocity (OpenFoam, 2011-2015).

Solver	**Scheme** **(Defined for each term in Navier-Stokes equations)**
PisoFoam **BuoyantBoussinesqPimpleFoam** **(Unsteady Simulations)**	Time included terms: CrankNicolson/2nd order Euler backward Gradient included terms : Gaussian-Linear Laplacian included terms: Gaussian-Linear (corrected) Divergence included terms: Gaussian-Linear
SimpleFoam **(Steady-State Simulations)**	Time included terms: Steady State Gradient included terms : Gaussian-Linear Laplacian included terms: Gaussian-Linear (corrected) Divergence included terms: Gaussian-Linear upwind

Table I: Numerical schemes used in OpenFoam for the simulation of mixing layers

3.4. Time Steps

When using the implicit coupled method for 2D simulations in ANSYS-Fluent, corresponding final Courant number was set to 20. This value resulted in more stability, robustness and faster convergence compared to simulations run with higher Courant numbers. Furthermore, underrelaxation factors were decreased and controlled based on monitoring of residuals, in order to minimize numerical diffusive and dispersive errors, particularly in regions with high gradients. In cases of simulations run in OpenFoam, the maximum Courant number was set to 0.8 since the schemes are explicit. Moreover, the OpenFoam adjustable time step command was used to optimize the time steps in terms of behavior of the residuals. It is noted that in simulations of 3D turbulent mixing layers, residuals observed in each of the simulations exhibited a type of sinusoidal behavior with reducing peaks within the computation time. This occurs mainly due to reproduction mechanisms of the turbulence on one hand, and the presence of non-linear convection terms in the governing equations on the other.

Fixed time steps throughout the domain are determined by using:

$$CFL = \frac{\overline{u_i}\Delta t}{\Delta x_{min}} + \frac{\overline{u_j}\Delta t}{\Delta y_{min}} \tag{36}$$

in which Δx_{min} and Δy_{min} are defined as streamwise and transverse distances of the smallest cell with minimum face area in the 2D grid (or minimum volume in the 3D case) and CFL is the maximum Courant number. The second term on right hand side of Equation (36) was neglected since the transverse velocity component of the current mixing layer is very small. Table II shows corresponding time steps for both 2D and 3D cases in terms of free-stream velocity. Note that, the Reynolds number definition in the present work, in both laminar and turbulent regimes, is based on the inflow velocity field and the chord length of the airfoil.

Operating Velocity (m/s)	Time Step Size (s)	Reynolds Number
0.15	0.0938	10,000
1.5	0.00938	100,000
2.25	0.00626	150,000
3.75	0.00375	250000(Turbulent)
7.5	0.00187	500,000(Turbulent)

Table II: Time step sizes in 2D and 3D simulations of mixing layers

In the case of 3D simulations of turbulent mixing layers, the time steps in Table II (labeled by Turbulent) were used as initial guesses. Lowering these time steps to the order of 10^{-4}s for RANS-based modeling at the beginning of the simulations provided convergence and also stability of the results. Likewise, in LES modeling, the initial time step was set as 10^{-5}s, and then increased up to 3×10^{-5}s once first convergence of the residuals was observed.

3.5. Parallel Processing

To reduce computation time of 3D OpenFoam simulations, e.g. LES of turbulent mixing layers, shared memory parallel processing (SMP) was used. In SMP, each processor has access to the overall memory of the machine and consequently spends less computation time compared to distributed memory parallel processing (DMP). However, methods for controlling and updating the data for each processor are complicated for the former type.

The computation domain was decomposed into four sub-domains defined on four processors as depicted in Figure 11. A Simple-Hierarchical method was used to uniformly distribute the grid on four processors based on x-*y*-z order. There are different types of decomposition methods defined in OpenFoam e.g. hierarchical and scotch. The former one defines an order in distribution of the sub-domains whereas the latter one specifies a weighting coefficient to each of the processors as well as a memory distribution strategy so that the computation is concentrated on a particular zone(s).

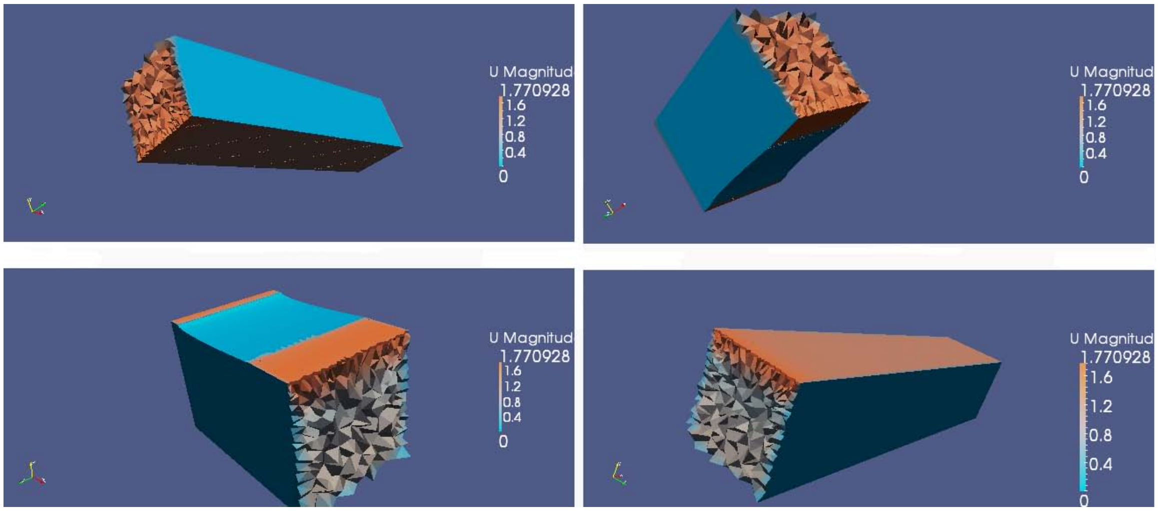

Fig. 11: Four sub-domains resulted from decomposition of the grid by using the Simple-Hierarchical method for 3D simulations of mixing layers

3D numerical simulations of the present study were conducted by means of the standard message passing interface parallel computing method (openMPI) based on a single node - local host - in an Intel-Core i7 Linux-operated machine. Running the unsteady laminar mixing layer simulations on four processors decreased computation time by a factor of three in comparison with a single processing unit, using the same time step size in both cases. This reduction is even more significant in LES of 3D turbulent mixing layers in which computation time was reduced approximately up to four times in comparison with simulations conducted by a single processor.

Chapter 4: Grid Description and Boundary Condition Setup

4.1. Geometry and Grid Generation

Following the experiments of Hollingsworth and Bourgogne (1995) and Mehta (1991), rectangular computational mesh domains around the NACA0006 airfoil, with the dimensions of 4C×7C in the 2D case and 4C×7C×1C in the 3D case, were developed in Gambit. Mesh grids are different from ordinary C-type or O-type meshes frequently used for airfoils. Figures 12 - 14 exhibit grids generated in 2D and 3D domains respectively. The boundaries' names are labeled in Figure 12 for clarity. The airfoil section of chord C=1m with a sharp trailing edge has a zero angle of attack, aligned with oncoming flow. As illustrated in the figures, in order to investigate the gradients across the mixing layer and thin boundary layers precisely, a hybrid mesh consisting of structured quadrilateral elements for near-wall regions and the mixing layer core was generated. An unstructured mesh with triangular elements was used for the rest of the domain, i.e. potential flow field. The resulting hybrid grids were also refined and smoothed-swapped adequately so that any possible deficiencies and skewness in cells were eliminated. Grid refinement was performed by using the skewness-based smoothing method. The total number of elements in the two-dimensional case is about 120,000; that increased up to 630,000 for the three-dimensional grid.

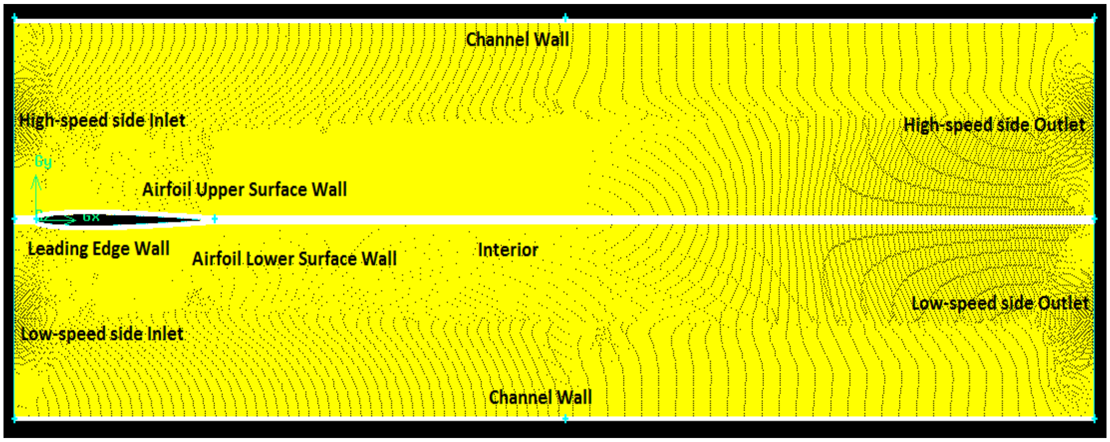

(a)

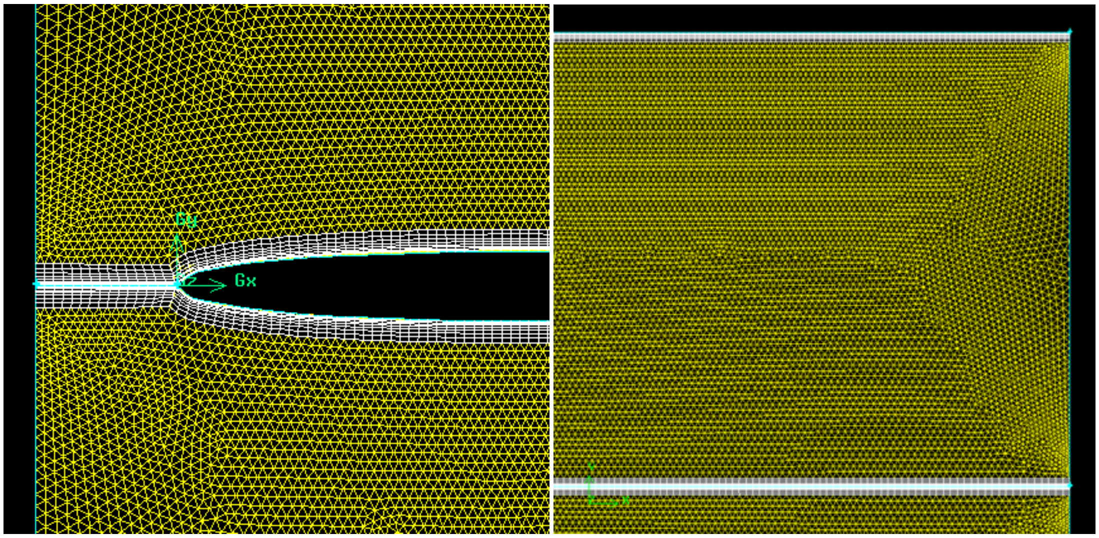

(b) **(c)**

Fig. 12: 2D hybrid mesh for the mixing layers generated by flow past a NACA0006 airfoil; a) boundaries – close-up view of: b) the leading edge wall, c) mesh resolution at the end of domain

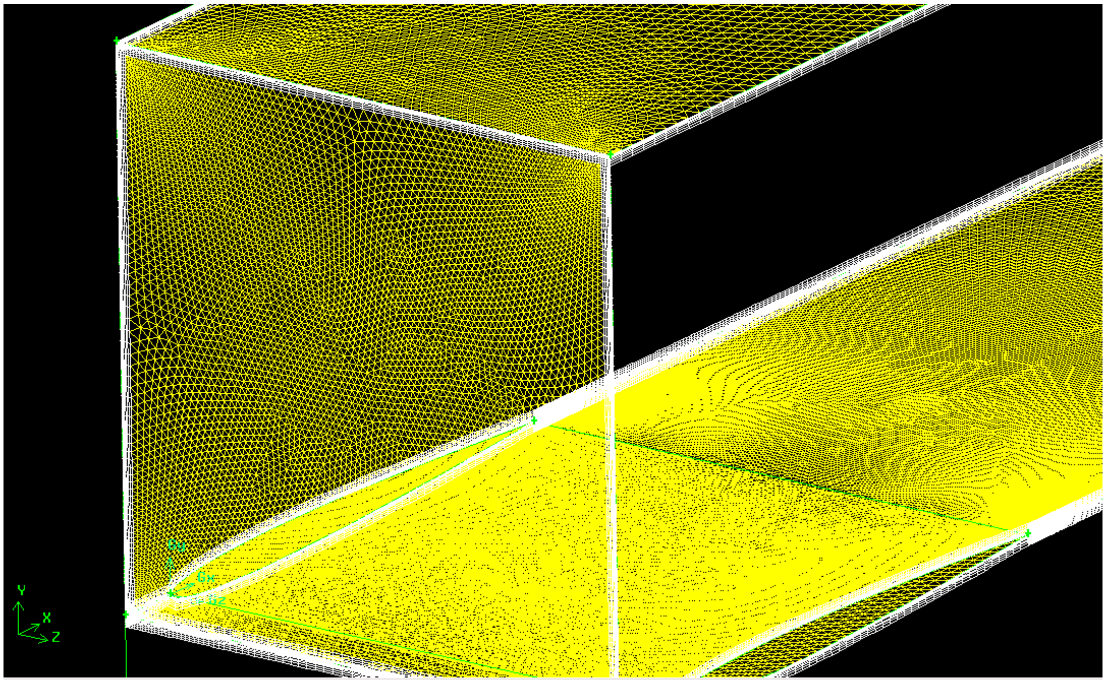

(a)

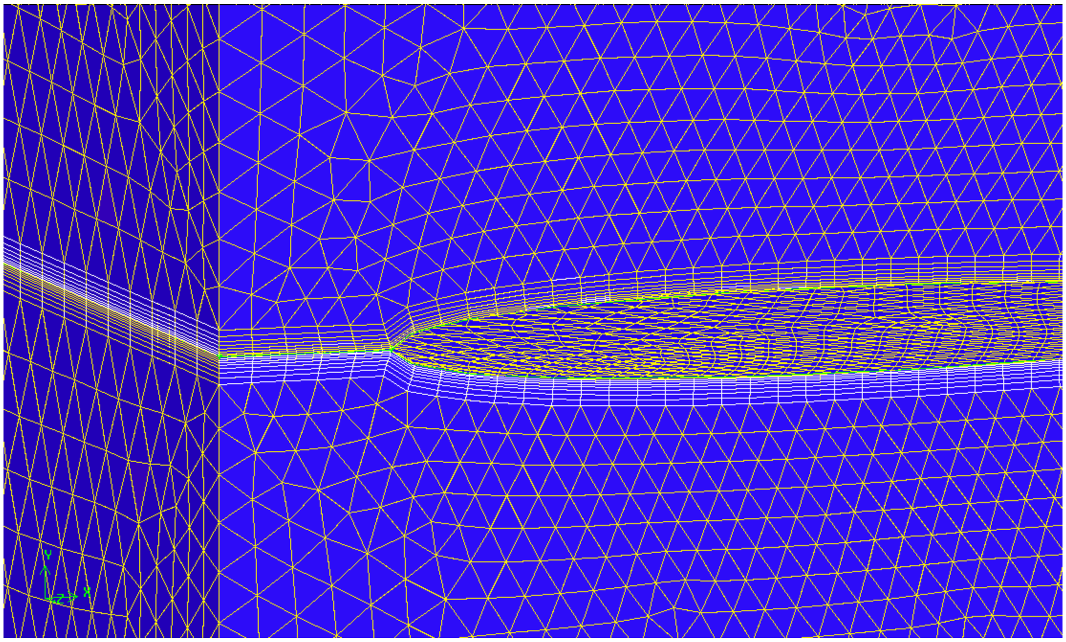

(b)

Fig. 13: 3D hybrid grid for the mixing layers generated by flow past a NACA0006 airfoil – close-up view of: a) upper side (only four planes provided), b) mesh resolution at the airfoil leading edge

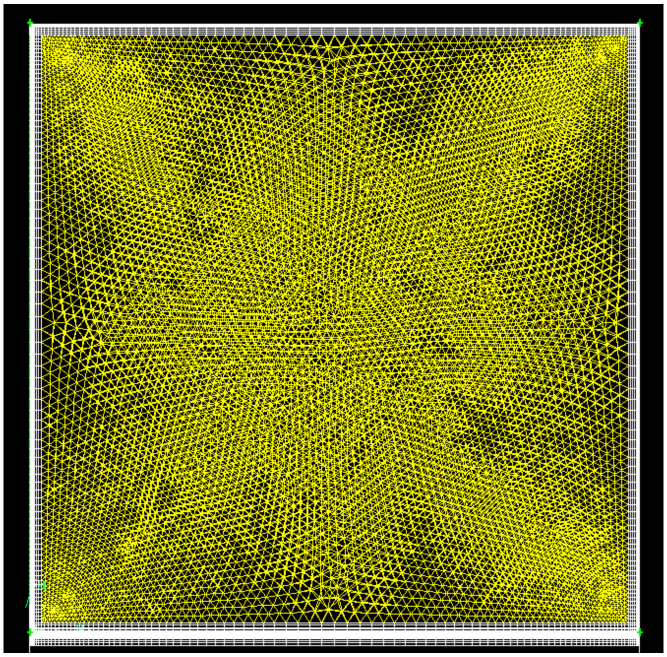

(a)

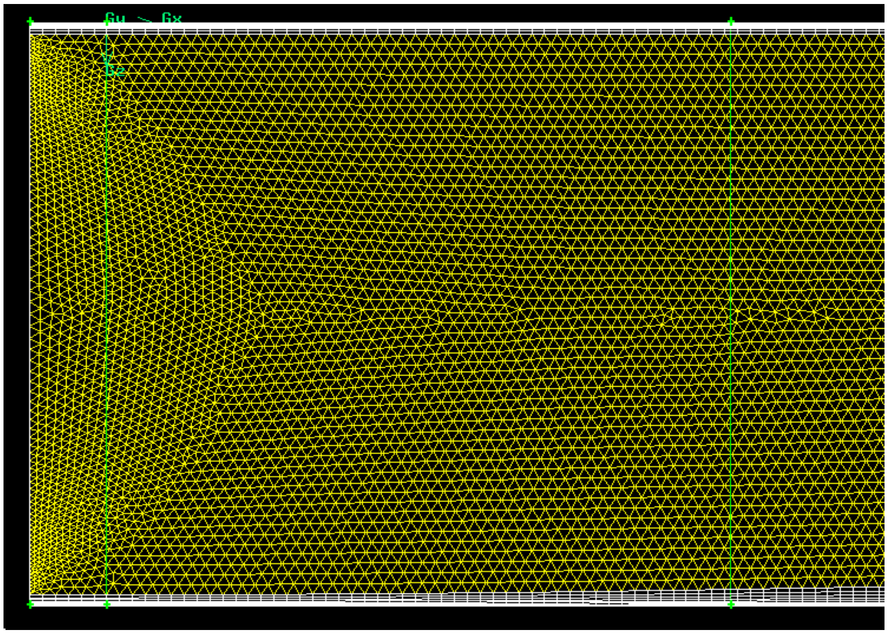

(b)

Fig. 14: 3D hybrid mesh for the mixing layers generated by flow past a NACA0006 airfoil; a) side (frontal) view (*y*z plane - upper side), b) top view (xz plane)

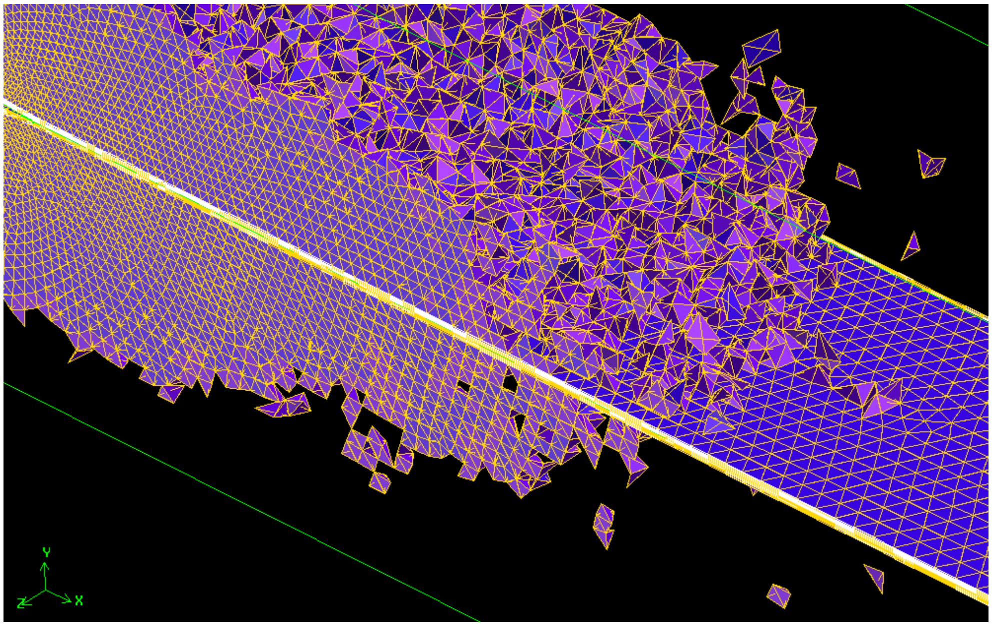

(a)

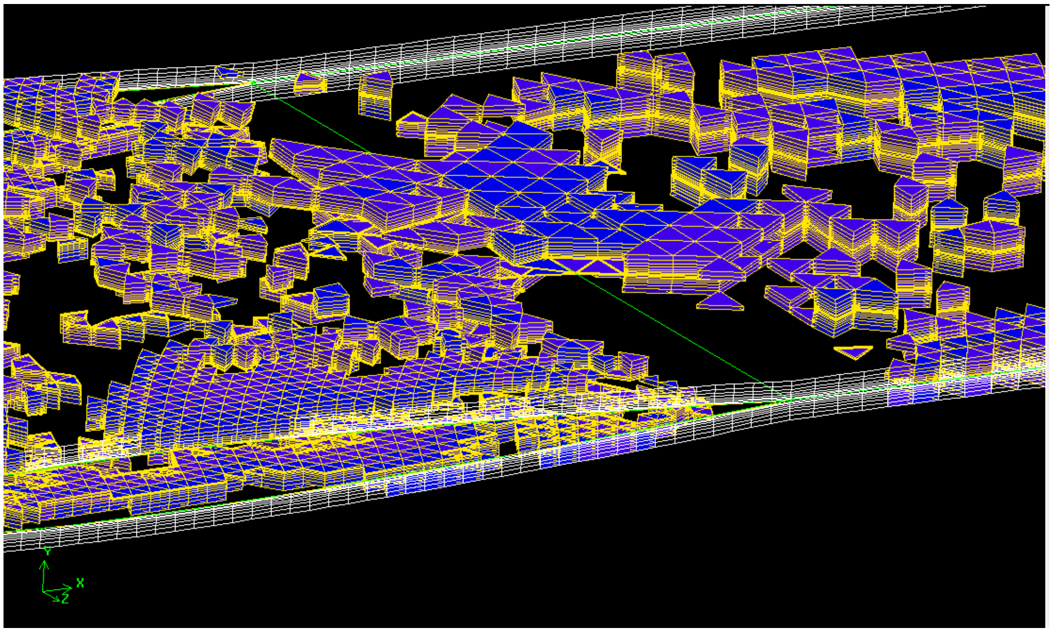

(b)

Fig. 15: 3D hybrid mesh element type; a) tetrahedrons used for potential flow field, b) wedges used for near-wall regions and mixing layer core (boundary layer mesh)

In order to prevent the early mixing of high and low-speed streams ahead of the airfoil leading edge, as shown in Figure 16, a small wall with length of one eighth of the chord (C) was applied in front of the airfoil, between the inlet boundary and the airfoil leading edge. A close-up view of this separating wall is provided in Figure 13.

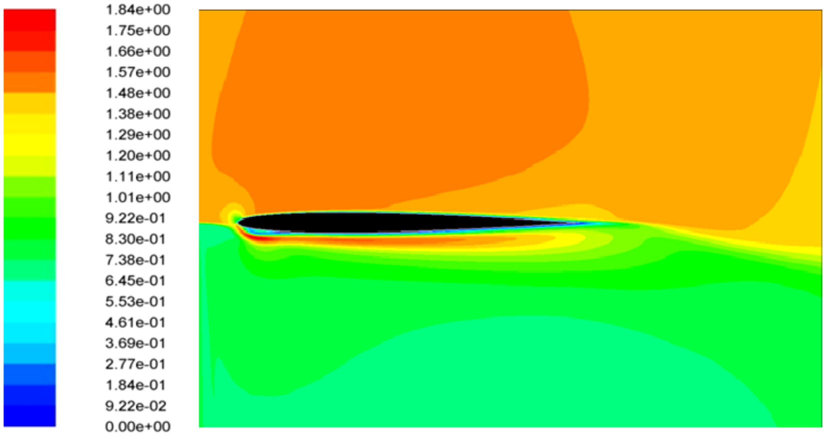

(a)

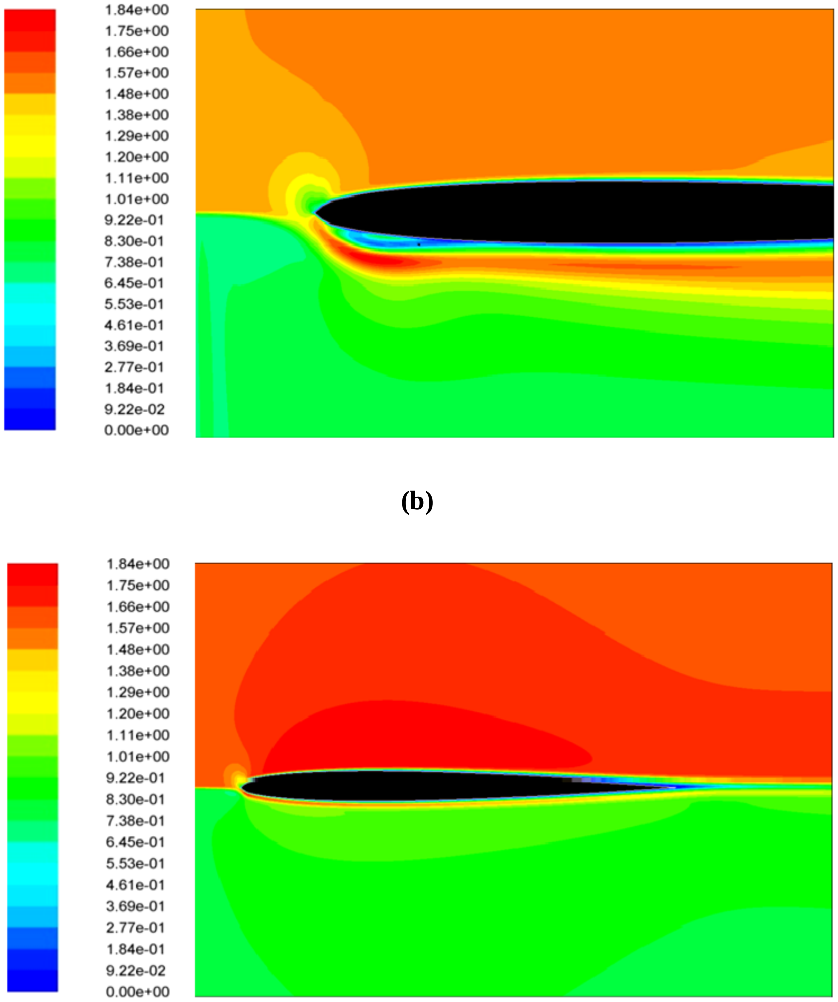

(b)

(c)

Fig. 16: Early mixing of high-speed side and low-speed side streams at high-speed side U_∞=1.5 m/s in the case of using an interior boundary condition at the airfoil leading edge; velocity contours at a) t=2.1s, b) t=2.1s (Close-up view of leading edge), 3) last time step (solution converged)

In order to ensure that results of simulations are not sensitive to the computation domain, dimensions of the surrounding walls around the airfoil in the 2D case were increased up to 3 times the primary distances, as shown in Figure 17. Conducting the new simulations in this extended domain, except for a few cases in the turbulent mixing layer, shows negligible differences with results found in the previous domain. Thus, it is possible to say that domain walls can satisfy approximate far-field conditions. Likewise, in order to check the sensitivity of the mesh to the type of the elements, steady laminar simulations were tested over a structured grid with hexahedral elements with the same number of cells (around 120,000 for 2D case and 630,000 for 3D case) as in the hybrid case. Differences between results of using these two types of meshes were quite negligible. However, due to alignment of the hexahedral cells with free-stream gradients, it is evident that structured meshes generally give smoother results. Figure 18 shows structured meshes in 2D and 3D generated around the airfoil (wing).

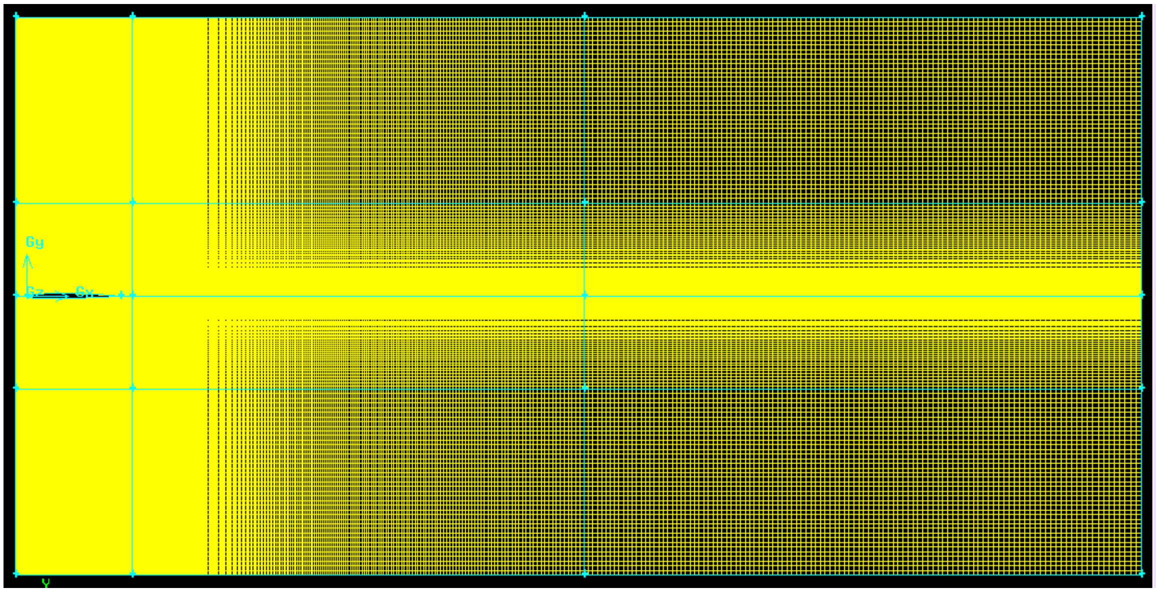

Fig. 17: Structured mesh in the extended domain to examine the sensitivity of results to domain dimensions

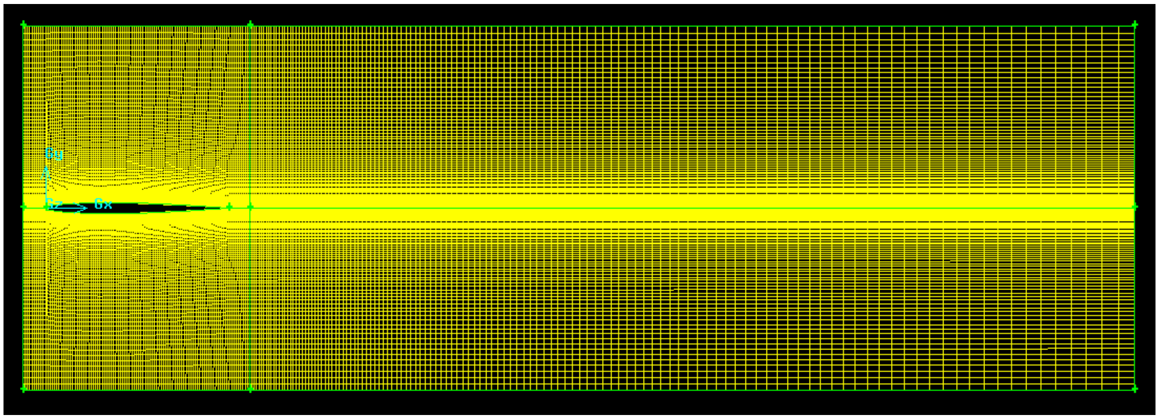

(a)

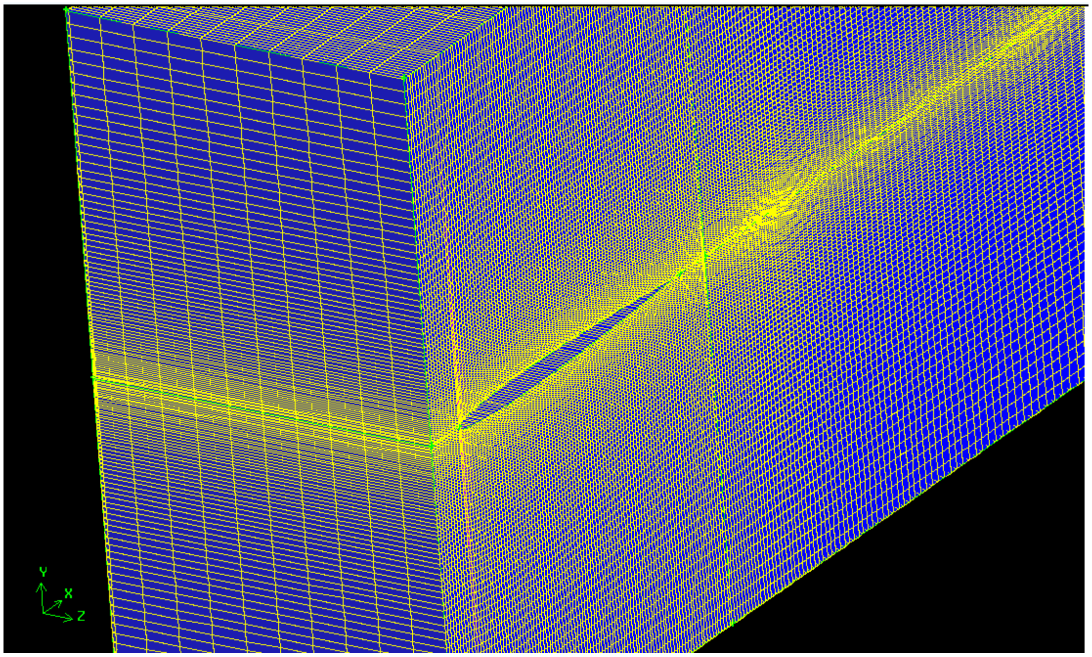

(b)

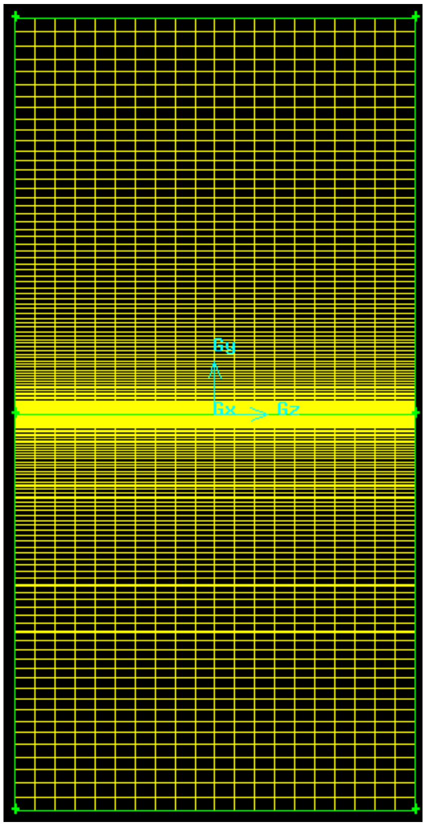

(c)

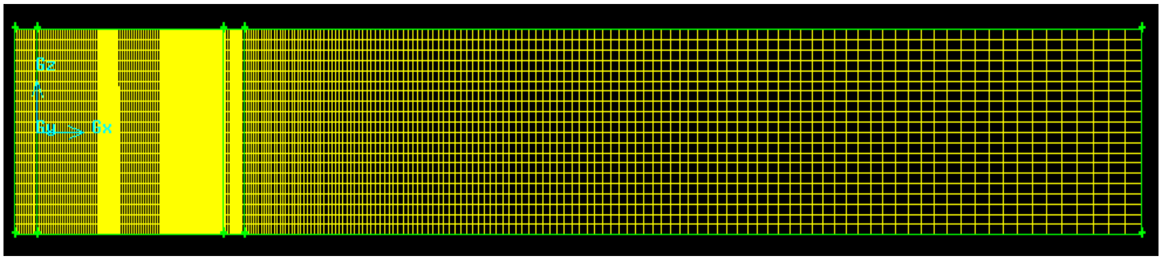

(d)

Fig. 18: Structured grid generated around the airfoil to examine the sensitivity of results to mesh type: a) 2D; and 3D grid: b) isometric view, c) side (rear) view (yz plane), d) top view (xz plane)

In order to minimize truncation errors of numerical simulations (artificial diffusion) and also investigate flow gradients within the mixing layer core more precisely, the transverse distance of the first elements in the boundary layer mesh (structured elements in the hybrid mesh of the present case) was chosen to be small: 0.0021m in the near-wall regions with increasing rate of 0.235m for 8 layers (in the boundary layer mesh generation). This value was found based on the Non-Equilibrium Wall Function rule, $y^+< 5$ (White, 2006, pp. 414-440), so that variations of the flow parameters within the viscous sub-layer in near-wall regions as well as the mixing layer core are fully resolved. This consequently allows use of the Wall Treatment Behavior method (White, 2006, pp. 414-440) in solving the governing equations in the viscous sub-layer in the case of turbulent mixing layers. It is also notable that by using these dimensions for hexahedral elements in the near-wall region (boundary layer grid), the order of the Kolmogorov length scale for small-scale eddies in turbulent flows, i.e. $\eta^+= 2$, is well met (Tavoularis, 2012). In addition, the hybrid grids are generated such that grid anisotropy is fulfilled sufficiently. As studied by Kaltenbach (1997), computation of turbulent shear flows is more economical if an anisotropic grid is used: resulting ratios of Reynolds stresses are adequately bounded to meet uniformity of turbulent properties. Observation of streamwise variations of y^+ in the present study shows a decreasing trend from a maximum value, 4 at the beginning, to about 3.1 at the end of the domain.

4.2. Boundary Conditions

Appropriate boundary conditions with respect to the physics of the mixing layer were applied in 2D simulations conducted in ANSYS-Fluent. These conditions are different in OpenFoam for 3D mixing layer simulations: as described in the following, boundary condition type varied depending on the regimes of the flow as well as the solver used.

Table III illustrates the types of boundary conditions used in ANSYS-Fluent. As seen, in all 2D simulations run in ANSYS-Fluent, two velocity-inlet and two pressure-outlet conditions were chosen at the left and right sides of the mixing layer domain, respectively. The internal boundary condition between the high and low-speed sides was defined as interior so that the conservations of flow parameters at the interface are guaranteed. Also, no-slip, impermeable walls were assumed for the boundaries including the small wall in front of the airfoil leading edge. In all of these simulations, atmospheric pressure was set at the pressure outlet.

Boundary Name	Boundary Type
High/Low-speed Side Inlet	Velocity Inlet
Leading Edge Wall	No-Slip, Impermeable Wall
Channel Walls	No-Slip, Impermeable Wall
High/Low-speed Side Outlet	Pressure Outlet (1atm)
Interior (interface)	Interior

Table III: Boundary condition setup for 2D simulations in ANSYS-Fluent

For 3D simulations run in OpenFoam 2.3.0, at each Reynolds number, two inlet velocity fields were applied upstream of the leading edge and corresponding outlet boundaries were implemented at seven chords lengths downstream of the airfoil, as in the 2D simulations. Table IV represents the boundary conditions and their types used for this study for 3D simulations run in OpenFoam. Note that, depending on the solver, the type of boundary condition changes.

Solver	Model	Boundary Conditions	Type
PisoFoam and BuoyantBoussinesqPimpleFoam (Unsteady Simulations)	**Laminar**	Pressure Outlet	"fixedValue" (atmospheric pressure)
		Velocity Inlet	"fixedValue" for velocity and temperature (vary in terms of Re number and free-stream temperature)
		Wall	“zeroGradient” in scalar boundary fields and “fixedValue” of 0 in vector boundary fields
SimpleFoam (Steady Simulations)	**Laminar**	Pressure Outlet	"fixedValue" (atmospheric pressure)
		Velocity Inlet	"freeStream" (fixedValue in terms of Re number)
		Wall	“zeroGradient” in scalar boundary fields and “fixedValue” of 0 in vector boundary fields
PisoFoam (Unsteady Simulations - Turbulence)	**K-ϵ Realizable**	Pressure Outlet	“InletOutlet” for U, k, ϵ fields, “fixedValue” of 0 for P field, “calculated” for μ_t field. “fixedValue” of 0 for U field,
		Velocity Inlet	“zeroGradient” for P field, “calculated” for μ_t field, “turbulentIntensityKineticEnergyInlet” for k field, “turbulentMixngLengthDissipationRateInlet” for ϵ field
		Wall	“fixedValue” of 0 for U field “zeroGradient” for P field, Appropriate “wallFunction” for k, ϵ, μ_t fields
	Large Eddy Simulation (LES)	Pressure Outlet	“fixedValue” of 0 for P field, “InletOutlet” for U, k field, “zeroGradient” for μ_{t-sgs}.
		Velocity Inlet	“turbulentInlet” with uniform reference field and fluctuation scale for U field, “zeroGradient” for scalar fields, “turbulentIntensityKineticEnergyInlet” for k field.
		Wall	“fixedValue” of 0 for U, k fields, “zeroGradient” for scalar fields

Table IV: Boundary condition setup for 3D simulations of mixing layers in OpenFoam

It should be pointed out that in simulation of 3D turbulent mixing layers appropriate boundary conditions were defined according to the applied turbulence model and solver. For instance, wall function boundary conditions such as epsilonWallFunction are specified for each of the walls in simulations done by use of the $k-\epsilon$ model. The type of the wall function is changed for different turbulent properties. Likewise, in the definition of the outlet conditions for turbulence quantities including ϵ, k, u, μ_t (or μ_{t-sgs} in the LES), "inlet-outlet" boundary conditions are used for the outlet boundary instead of the zero-gradient employed in the laminar case. For clarity, the boundary conditions employed in LES and Realizable $k-\epsilon$ models in the present work simulations are declared in Table IV. It is also noted that different inflow boundary conditions are set for turbulence simulations done by LES. This will be further detailed in Chapter 6.

Chapter 5: Laminar Mixing Layers - Results and Discussion

Two and three-dimensional mixing layers resulting from the numerical simulations of the airflow over the NACA0006 airfoil splitter plate are studied in this chapter. Moreover, based on the theoretical solution of the Falkner-Wedge flows, the 2D laminar mixing layer of the present work is investigated analytically. The ratio of upper stream to lower stream velocities is fixed at 2 while free-stream velocity of the high-speed side changes from 0.15 to 2.25 m/s, corresponding to flow Reynolds number values between 10,000 and 150,000 in laminar regimes. In addition, temperature of the free streams over the airfoil varies between 250 K and 400 K to explore the behavior of the mixing layer in different inflow conditions. Air with temperature dependent properties is considered as the operating fluid in this case. Mixing layer growth rate parameter variation in both streamwise and spanwise directions is also investigated.

5.1. Two-Dimensional Mixing Layers

5.1.1. Analytical Solution - Steady State

For large Reynolds number flows, a thin boundary layer sets up along solid walls. Thus, effects of viscosity are confined to narrow regions near the body in such a way that the rate of downstream convection is larger than the rate of transverse viscous diffusion (White, 2006, pp. 215-236). As used by Schlichting and Gersten (2000, pp. 127-200), boundary layer approximations were employed in the present work to simplify the steady Navier-Stokes equations:

$$\frac{\partial u}{\partial x}+\frac{\partial v}{\partial y}=0 \tag{37}$$

$$u\frac{\partial u}{\partial x}+v\frac{\partial u}{\partial y}=U\frac{\partial U}{\partial x}+\nu\frac{\partial^2 u}{\partial y^2} \tag{38}$$

where,

$$U\frac{\partial U}{\partial x} = -\frac{1}{\rho}\frac{\partial p}{\partial x} \ . \tag{39}$$

Equations (37)-(39) form a system of parabolic partial differential equations. As Blasius proved (Schlichting and Gersten, 2000), in the case of unbounded mixing layers behind flat plates, the system of equations can be changed into an ordinary differential equation by using a similarity variable, η. According to Lock (1951), for the mixing layer behind the flat plate with a ratio of 2 between high and low-speed sides, assuming very small streamwise changes of u compared to transverse variation, the similarity solution procedure gives the momentum equation as:

$$f_i''' + 2f_i f_i'' = 0 \qquad i = 1, 2 \tag{40}$$

where,

$$f_i' = \frac{u_i}{U} \quad , \quad f_i = f_i(\eta) \quad , \quad \eta = y\sqrt{\frac{U}{\nu x}} \tag{41}$$

defined for both high-speed ($i = 1$) and low-speed ($i = 2$) streams. This also can be generalized for thin airfoils. Thus, appropriate boundary conditions to solve Equation (38) are set as:

$$f_1'(\eta_{max}) = 1 \quad , \quad f_2'(\eta_{min}) = 0.5 \tag{42}$$

$$f_1(0) = f_2(0) = 0 \quad , \quad f_1'(0) = f_2'(0) \quad , \quad f_1''(0) = f_2''(0) \tag{43}$$

in which the 2nd derivative of f represents the shear stress generated at the interface of two streams. It is notable that Equations (37)-(43) can be interpreted as simplified forms of the famous Falkner-Skan wedge flows equations analytically solved by Hartree (1937). In the current study, Equations (40)-(43) were solved as a boundary value problem in Matlab.

Of interest are the velocity profiles in the laminar mixing layer of the present study found in the last station, x=7m. In order to validate the results in the last station of the domain with analytical solution data, the boundary value problem, Equations (40)-(43), was solved in Matlab and compared with results of the numerical solution (Figure 19a). As displayed in the figure, dimensionless velocity values found in the laminar 2D airfoil numerical simulations compare relatively well to the corresponding values of the analytical solution for the Falkner-Skan mixing layer behind the flat plate. It is evidently noticed that there is about 10% difference between dimensionless numerical and analytical values, which can be attributed to the wall boundary layer effects, airfoil curved geometry and inexact simulation fidelity. Besides, in the analytical solution, pressure gradient in the streamwise direction is approximated by Equation (39) and therefore is not accurately reflected in the solution. The presence of channel walls makes the simulation case different than the (unbounded) analytical solution case and the overshoots in the velocity profiles could be explained by the retarded flow in the wall boundary layers.

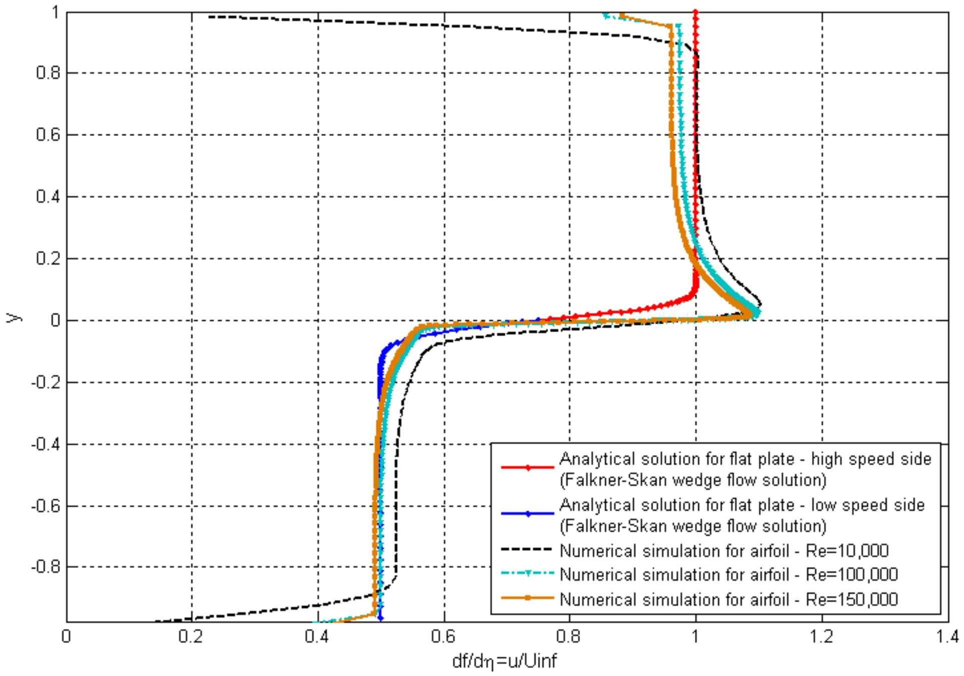

(a)

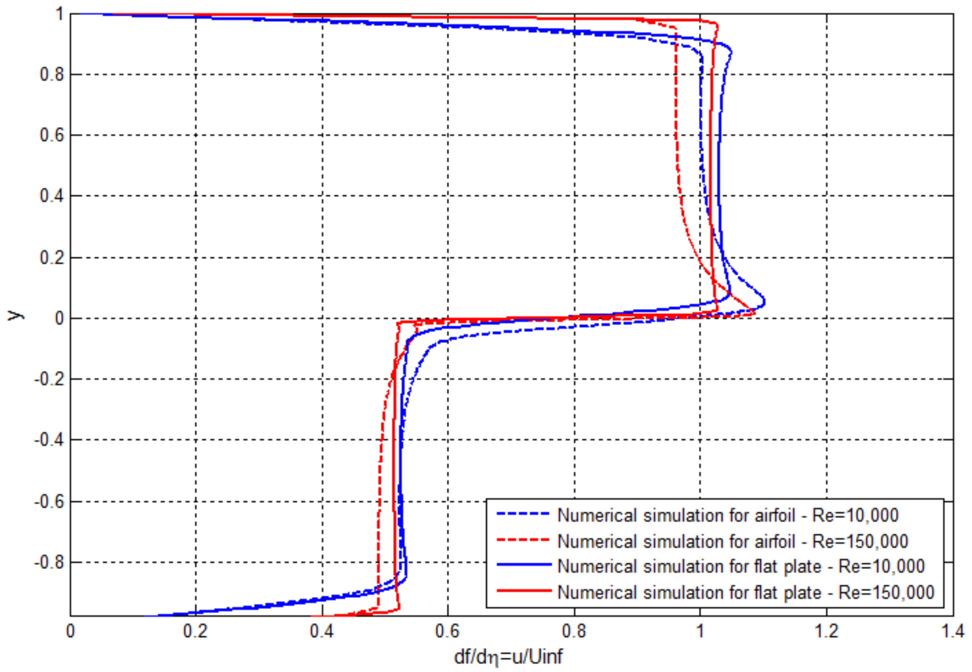

(b)

Fig. 19: Validation of steady dimensionless numerical velocity profiles for the mixing layer behind the airfoil against: a) analytical solution - for high-speed side Re=10,000, 100,000, and 150,000, b) steady dimensionless numerical velocity profiles for the flat plate splitter mixing layer for high-speed side Re=10,000 and 150,000 - at x=7m

In addition to validating the numerical velocity profiles against the analytical solution, a series of 2D numerical simulations for corresponding mixing layers with a flat plate splitter (of length of 1m), instead of the airfoil, were used to validate the solutions. For the flat plate splitter channel a structured mesh was used and the same setup as for the airfoil simulations was employed for these simulations.

Dimensionless velocity profiles for mixing layers behind the flat plate and airfoil at high-speed side Re=10,000 and 150,000 at the end of the domain (x=7m) are shown in Figure 19b. Note that for clarity, velocity profiles at Re=100,000 are not provided in the figure. As indicated, the profiles approximately match each other. However, in the case of the mixing layer behind the airfoil a small momentum excess is observed on the high-speed side compared to the flat plate case. This increase in momentum could be interpreted by the formation of a stronger pressure gradient (Figure 20a) on the high-speed side imposed by the higher speed and the airfoil curved surfaces.

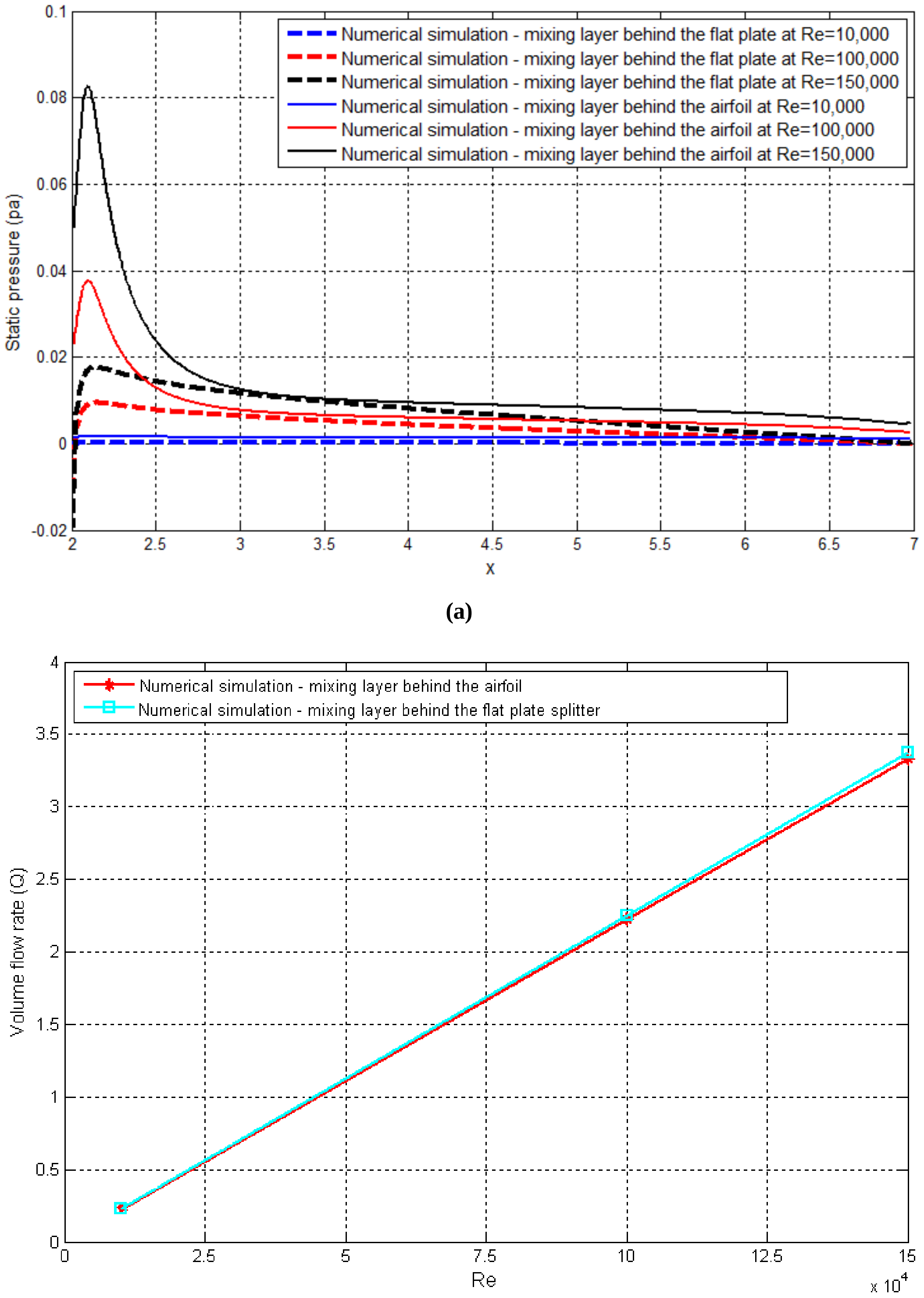

(a)

(b)

Fig. 20: Comparison of flow parameters for numerical mixing layers behind the airfoil and the flat plate splitter: a) static pressure variation in the streamwise direction (at y=0m), b) volume flow rate ($\frac{m^3}{s}$) at x=7m - for high-speed side Re=10,000, 100,000, and 150,000

Integrated velocity profiles show similar but slightly different flow rates (Q) across the x=7m stations as shown in Figure 20b. These flow rate comparisons, for the unbounded analytical flow, confirm that the velocity overshoots are necessary in order to balance the momentum deficits in the wall boundary layers, in order to conserve mass.

5.1.2. Analytical Solution - Unsteady

Using the approximations of boundary layer theory with the assumption of $u = u(y,t)$, the unsteady momentum equation can be written as:

$$\frac{\partial u}{\partial t} = -\frac{1}{\rho}\frac{dp}{dx} + \nu\frac{\partial^2 u}{\partial y^2}\ . \tag{44}$$

It is also possible to assume that pressure gradient in this study is estimated as a function of time by defining the following equation (White, 2006, pp. 128-155):

$$u = \bar{u}_{laminar}\ + \int \frac{1}{\rho}\frac{dp}{dx}dt \tag{45}$$

where $\bar{u}_{laminar}$ is the mean streamwise velocity in the laminar regime. So, Equation (44) is simplified to:

$$\frac{\partial u}{\partial t} = \nu\frac{\partial^2 u}{\partial y^2}. \tag{46}$$

There are several unsteady solution methods for this partial differential equation which are all dependent on the specified initial and boundary conditions. In the present work, boundary and initial conditions for the non-dimensionalized Equations (47)-(49) are specified in terms of the steady solution; it is also suitable to work with the difference between the unsteady and steady velocity solutions; so we define:

$$u_1(y,t) = u(y,t) - u_{steady}\,(y) \tag{47}$$

$$y^* = \frac{y}{h}\ \ ,\ \ t^* = \frac{t\nu}{h^2}\ \ ,\ \ u_1^* = \frac{u_1}{U} \tag{48}$$

giving for Equation (46):

$$\frac{\partial u_1^*}{\partial t^*} = \nu \frac{\partial^2 u_1^*}{\partial y^{*2}} \tag{49}$$

where h is the mixing layer thickness.

For each Reynolds number at different temperatures, the final velocity profile found at the end of the domain in the steady solution is fitted to a Gaussian function:

$$u_{steady}^* = \sum_{1}^{8} \frac{a_i \exp\left[-\left(\frac{(hy^* - b_i)}{c_i}\right)^2\right]}{U} \tag{50}$$

in which, a_i, b_i, c_i are fit constants for each of three Reynolds values. So, initial and boundary conditions were specified as:

$$u_1^*(y^*, 0) = 1 - u_{steady}^* \tag{51}$$

$$u_1^*(0, t^*) = \frac{u(0)}{U} - u_{steady}^*\,(0) \tag{52}$$

$$u_1^*(-1, t^*) = \frac{u(-1)}{U} - u_{steady}^*\,(-1)\ . \tag{53}$$

The unsteady solution can give velocity values for different streamwise stations. In the present work, however, the non-dimensionalized unsteady partial differential equations (49)-(53) were solved to give dimensionless time-dependent velocity profiles in the last station, i.e. x=7m for each Re number. Table V indicates the non-dimensionalized boundary values for each of three velocities.

Reynolds Number	**Boundary Values**
10,000 **(U=0.15 m/s)**	$0 \le t^* \le 0.0051$ $-0.571 \le y^* \le 0.428$ $u_1^*(y^*, 0) = 1 - \frac{u_{steady}^*}{U}$ $u_1^*(0, t^*) = -0.0053$ $u_1^*(-1, t^*) = 0.0086$

100,000 **(U=1.5 m/s)**	$0 \le t^* \le 0.0051$ $-0.571 \le y^* \le 0.428$ $u_1^*(y^*,0) = 1 - \frac{u^*_{steady}}{U}$ $u_1^*(0,t^*) = 0.0015$ $u_1^*(-1,t^*) = 0.004$
150,000 **(U=2.25 m/s)**	$0 \le t^* \le 0.0051$ $-0.571 \le y^* \le 0.428$ $u_1^*(y^*,0) = 1 - \frac{u^*_{steady}}{U}$ $u_1^*(0,t^*) = 0.0071$ $u_1^*(-1,t^*) = 0.0207$

Table V: Boundary values for the analytical unsteady solution of the laminar mixing layer

It is noted that boundary values in Table V are based on the known steady state solution found in the numerical simulations.

Figure 21 shows how the velocity profile changes with time in the last station for Re=150,000. The time-dependent profiles for the other two Reynolds numbers were found to be almost the same as these profiles.

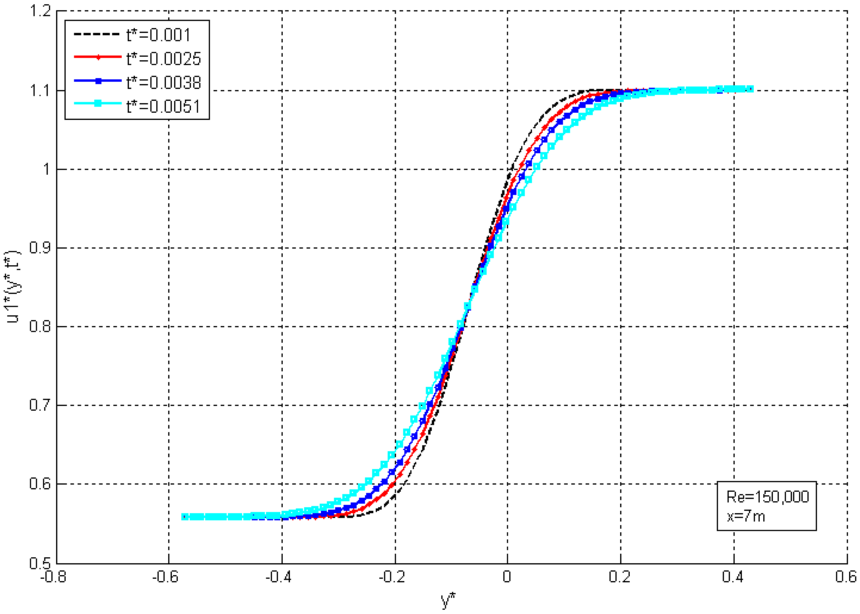

Fig. 21: Evolution of the dimensionless time-dependent velocity profiles at the end of the domain (x=7m) found analytically based on the steady numerical solution for the laminar mixing layer - Re=150,000

Moreover, Figure 21 shows that the velocity profile becomes more stable and less retarded as time proceeds. This can be explained by the fact that flow in the last station and at the last time step is smoothed-out such that the probability of formation of an inflexion point is considerably reduced.

5.1.3. Numerical Solution - Steady State

Contours of steady velocity for Re=100,000 are provided in Figure 22. Red colors in the contours represent the high-speed side. Because of the velocity ratio between the upper and lower sides, flow on the upper surface of the airfoil separates earlier compared to the flow on the lower surface. Although the velocity ratio is fixed at 2, the steady mixing layer in the downstream regions does not display either deflection toward the low-speed side or wavy-like motions.

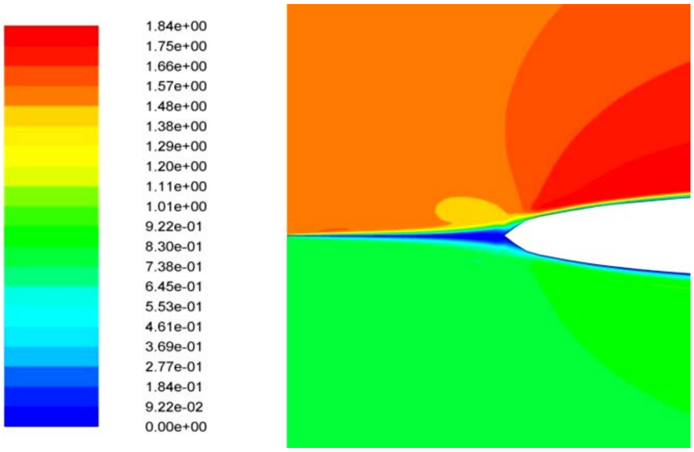

(a)

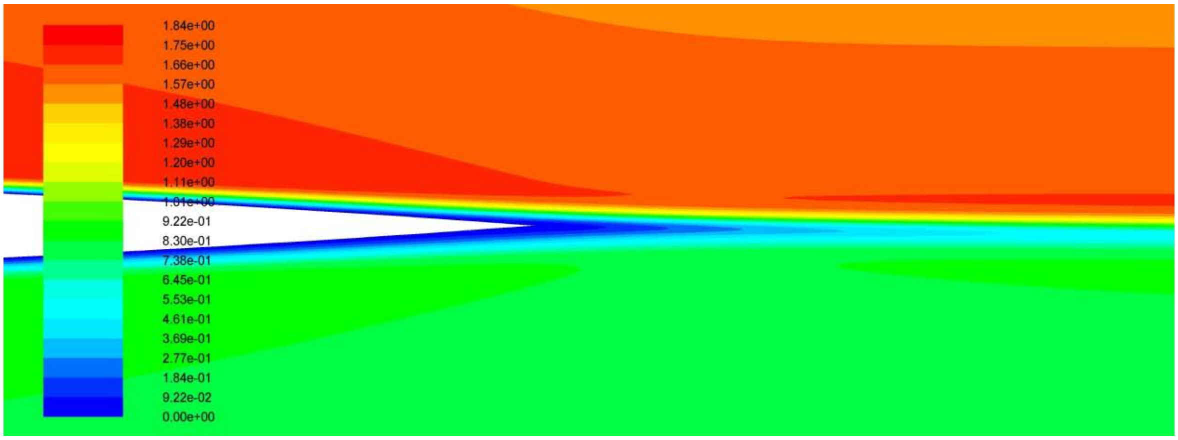

(b)

Fig. 22: Velocity contours (m/s) of steady 2D laminar mixing layer at Re=100,000 - close-up view of: a) front section of domain and airfoil leading edge, b) airfoil trailing edge

It is noted that in the velocity contours of fluid flow with high-speed side free-stream Reynolds numbers of 10,000 and 150,000 (not shown here), other than changes in the mixing layer width, which decreases with increasing the Reynolds number, no other important changes were observed.

Figure 23 shows normalized profiles of velocity against η at six streamwise stations, x=1.25m, 3m, 4m, 5m, 6m, and 7m at three high-speed side Reynolds numbers of 10,000, 100,000, and 150,000. Inflow velocity field magnitude of the high-speed side was chosen as a reference to normalize the velocity profiles.

In the wake region, the profiles show the known double-peak behavior with the tendency of the upper side streams toward the lower side. On the other hand, as will be discussed, the presence of higher values of velocity defect in early stations is evidently seen in the results. This occurs mainly due to the effects of the wake behind the airfoil. The double-peak (local minima and maxima) behavior of the profiles in the early stations is gradually eliminated in further downstream regions showing a smoothed-out, well-known S-shape velocity profile in the last station. It is also understood that for higher Reynolds numbers, with decreasing wake thickness behind the airfoil - which increases diffusivity of the wake within the mixing layer core (Figure 24) - streamwise retardation of the velocity profiles is recovered more quickly. Moreover, for the lowest Reynolds number there is a small overshoot of the high-speed side velocity profiles even in the last station that causes the velocity profiles of both sides to reach their asymptotic values (approximately 1.1) later and in higher η; this is expected to be because of the excess in pressure gradient and momentum which are imposed to the regions close to the airfoil forcing the profiles to need more time to recover.

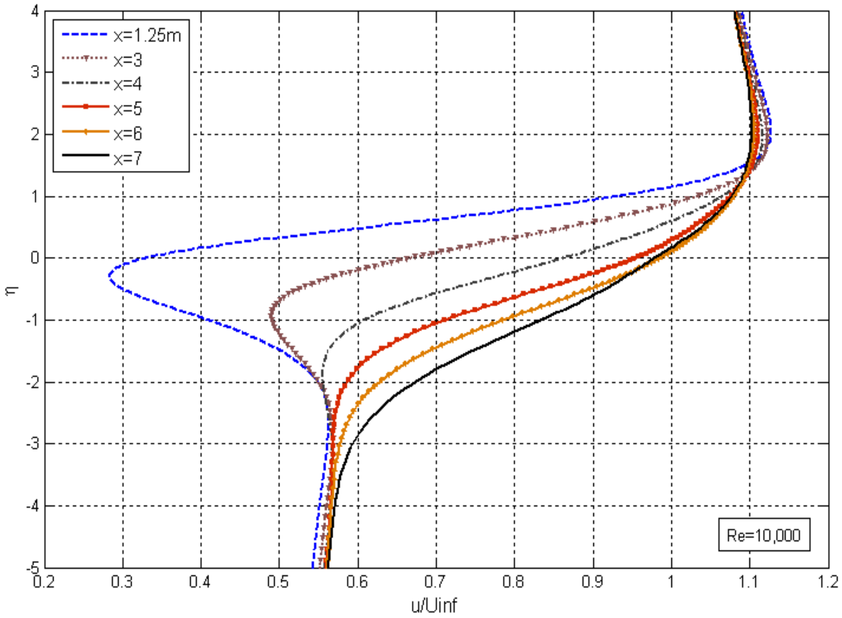

(a)

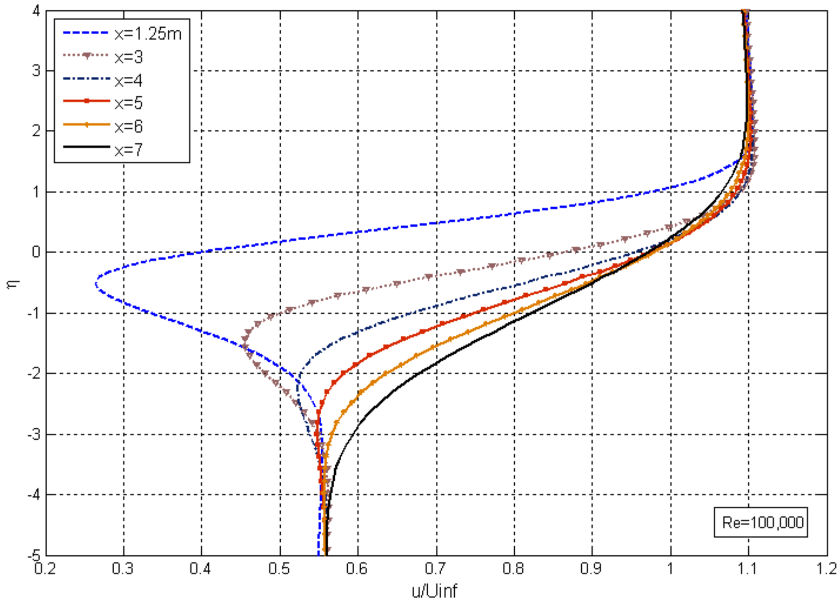

(b)

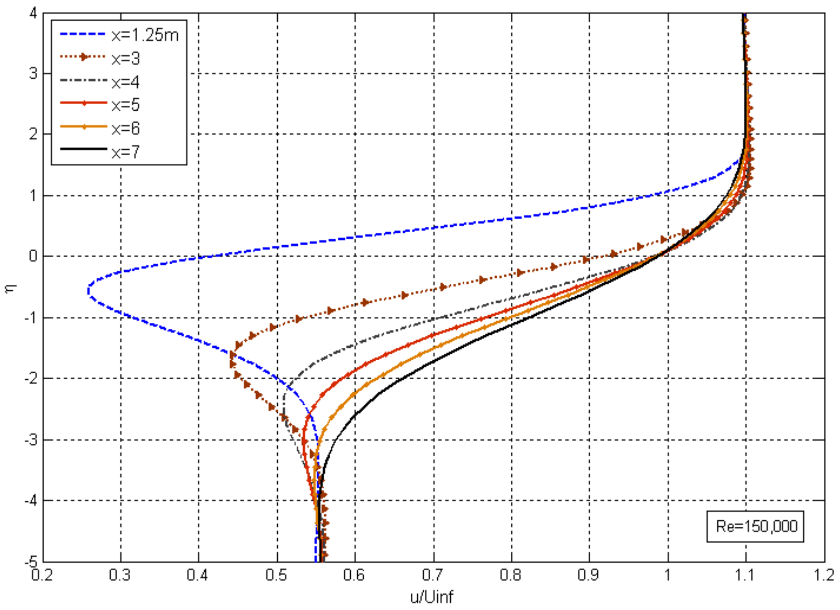

(c)

Fig. 23: Evolution of steady dimensionless velocity profiles in the streamwise direction for the 2D laminar mixing layer: (a) Re=10,000, (b) Re=100,000, (c) Re=150,000

It should be added that increasing the length of the channel in the case of laminar-turbulent mixing layers did not show any significant effect on the development of the velocity profiles. However, extension of the domain in the mainstream direction is expected to relatively eliminate the overshoot seen in the lowest Reynolds number velocity profiles. This conclusion, as mentioned earlier, is because of the nature of the developing boundary layer in near-wall regions around the airfoil - at low Re=10,000 - that requires a longer distance for the velocity profile to become fully-developed.

Another important observation of Figure 23 is that velocity profiles after a certain downstream point do not change and the global structure of the flow becomes insensitive to inflow conditions. This implies that self-similarity of velocity profiles in the laminar regime is achieved.

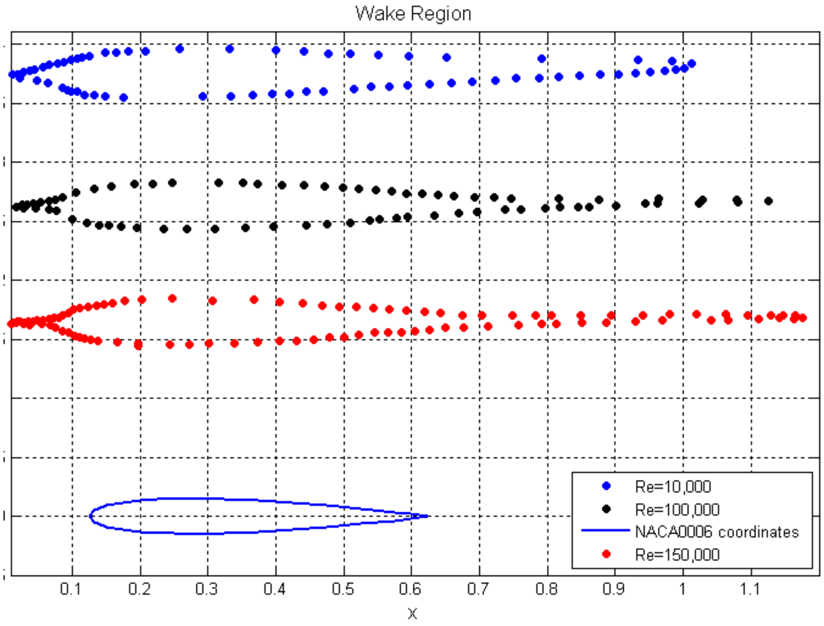

Fig. 24: Airfoil wake region bounds at different Re numbers - image processing of velocity contours in Matlab

Furthermore, transition to turbulence does not occur in either of the above cases. This is evidently because of two reasons: the Reynolds number is not large enough to guarantee formation of primary turbulent structures, and also there is no triggering mechanism such as initial disturbances to make the laminar mixing layer unstable enough and turn it into turbulent flow. In other words, T-S waves formed in the laminar case undergo a reverse transition and are back to their previous smooth laminar shape (Yarusevych et al., 2004).

It is noted that, the last station to plot the velocity profiles is taken at x=7m in the case of 2D laminar mixing layers. For turbulent mixing layers, x=6.75m is used so that any possible effect of the outlet boundary condition on the behavior of the velocity profiles is minimized. The laminar mixing layer results at x=6.75m were found the same as those taken at x=7m.

Velocity defect profiles in the streamwise direction at different Re numbers are depicted in Figure 25. As seen, defects are more apparent in upstream regions and then are washed-out slowly as the flow proceeds to the end of the domain. Needless to say, it is evident that velocity defects are generated due to the wake behind the airfoil. The geometry of the airfoil, the Re number and turbulence instabilities (fluctuations) are dominant parameters affecting the wake shape. There is a tendency of these defect profiles toward the low-speed side of the mixing layer. In addition, it is observed that velocity defect in the streamwise direction increases with increasing free-stream Reynolds number. This observation, as indicated before, causes an increase in the momentum loss (θ) in the streamwise direction and consequently results in increasing the shape factors. Note that, for clarity, different scales were used in the figures.

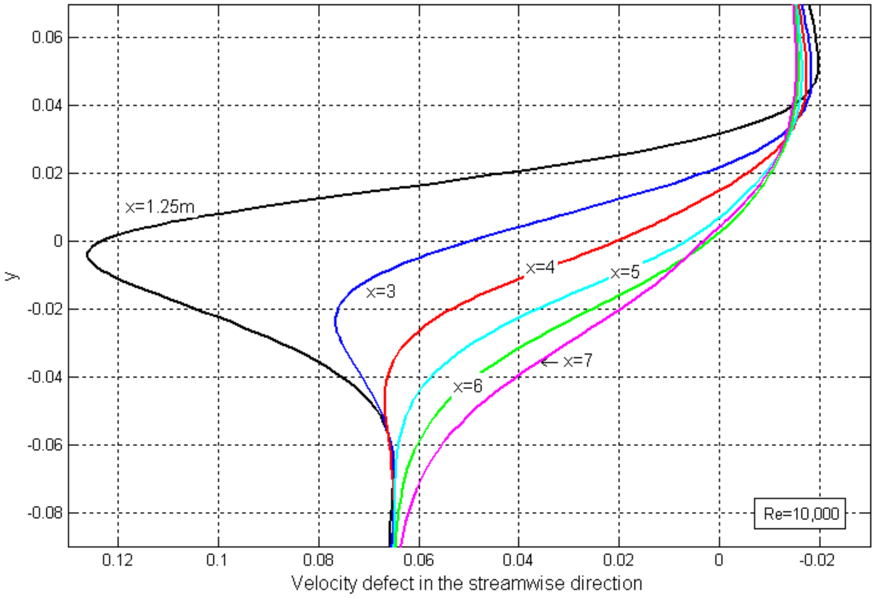

(a)

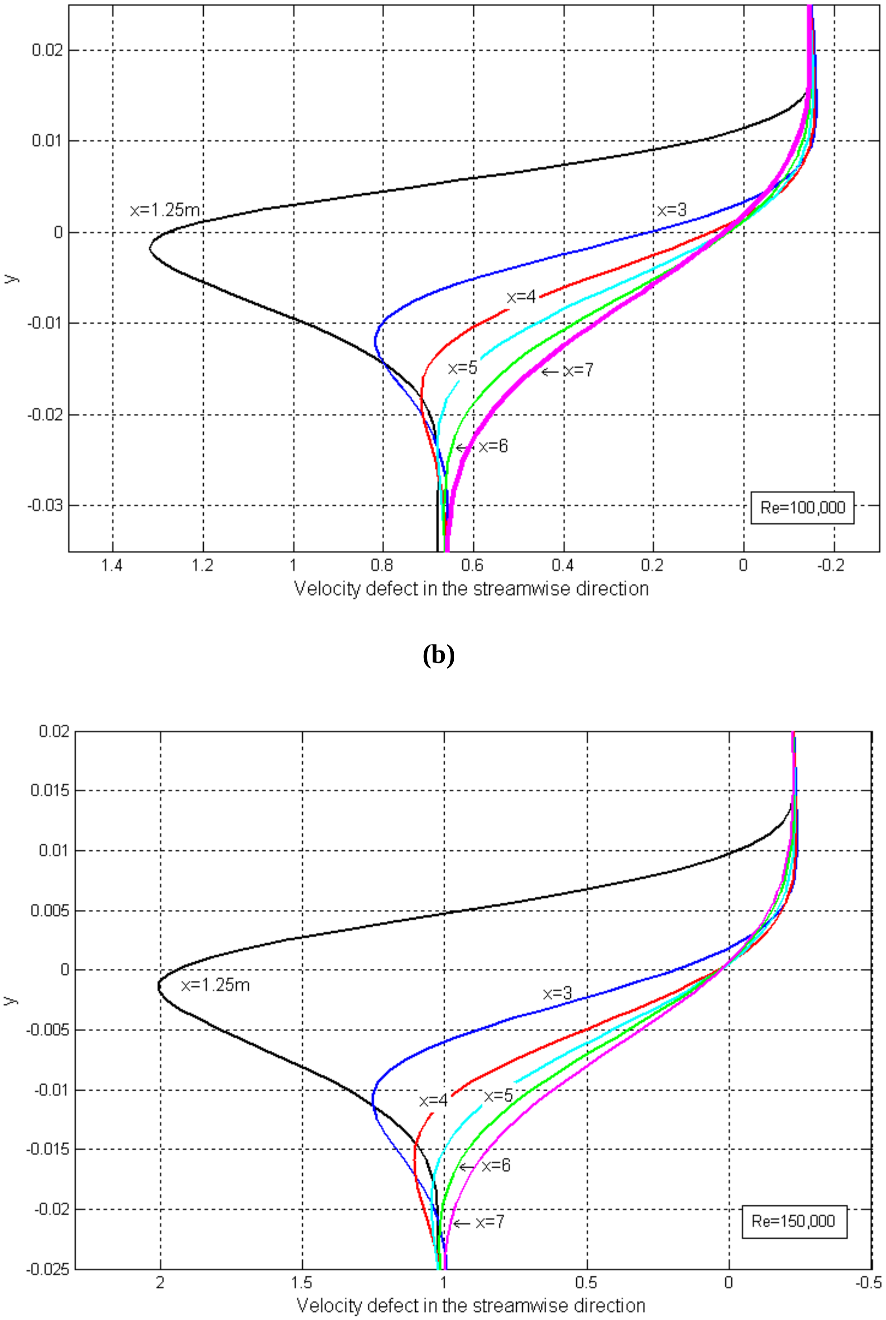

(b)

(c)

Fig. 25: Laminar mixing layer velocity defect profiles at different stations in the streamwise direction (x=1.25, 3, 4, 5, 6, 7m): a) Re=10,000, b) Re=100,000, c) Re=150,000

Generally in plane wakes, velocity-defect is estimated to decay as $\frac{1}{\sqrt{x}}$ in the streamwise direction (Weygandt and Mehta, 1995). Even so, in the case of mixing layers because of more entrainment of the flow, the streamwise decay is expected to be faster (Mehta, 1991). Moreover, decreasing the velocity difference between the two sides of the mixing layer basically produces a stronger wake (with higher vorticity magnitude) behind the splitter and leads the mixing layer to become weaker. Thus, distance and time required for the wake to wash out increase. Figure 26 represents streamwise changes of velocity defects at y=0m with inflow Re numbers for the current mixing layer.

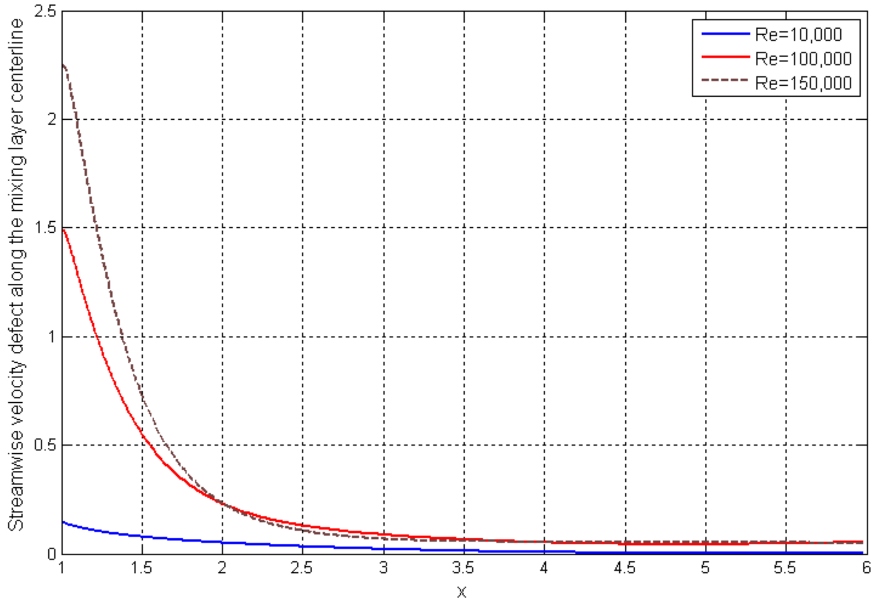

Fig. 26: Streamwise changes of the laminar mixing layer velocity defect with different free-stream Re numbers at y=0m

Variation of strain rate ($\frac{\partial u}{\partial y}$) along the centerline of the laminar mixing layer in terms of free-stream Reynolds number is illustrated in Figure 27. Due to the high magnitude of vorticity just downstream of the airfoil trailing edge, which occurs because of the wake formation, strain rate experiences a sharp decrease (small non-sheared region) and then starts increasing (sheared region), reaching a peak value at which maximum vorticity magnitude occurs. This trend is followed by gradual decrease of shear strain with streamwise distance. It is also evident that with increase in the free-stream Re number, higher values of strain rate - and vorticity magnitude - are observed.

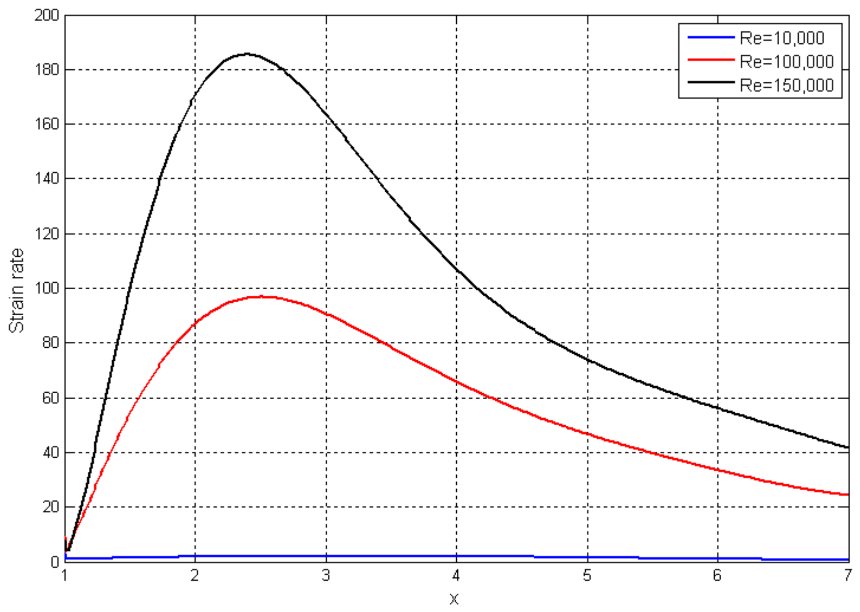

Fig. 27: Variation of strain rate at different free-stream Re numbers in the streamwise direction along the laminar mixing layer centerline

5.1.4. Mixing Layer Growth

Deflection of streamlines outside the mixing layer and hence the mixing layer growth rate can be expressed non-dimensionally by substituting the Blasius similarity parameters into the boundary layer displacement thickness as well as momentum thickness definitions:

$$\delta^{**}(x^*,t^*)=\sqrt{\frac{x^*\nu}{U}}\int_{\eta_1}^{\eta_2}(1-f^{'}(\eta))d\eta \tag{54}$$

$$\theta^*(x^*,t^*)=\sqrt{\frac{x^*\nu}{U}}\int_{\eta_1}^{\eta_2}f^{'}(\eta)\big(1-f^{'}(\eta)\big)d\eta \tag{55}$$

where $x^*={}^{x}/_{L}$, L represents the length of channel and t^* is defined in Equation (48). Figure 28 shows the variation of dimensionless momentum and displacement growth rates in the streamwise direction at different inflow Reynolds numbers. Free-stream temperatures of the mixing layer sides are fixed at 300K. An increase in rate of $\delta^{**}$and θ^* values is observed further downstream of the flow in such a way that they grow approximately two times faster for the lowest Re number in comparison with those at higher Re numbers. Much lower values of $\delta^{**}$and θ^{*} are estimated in the highest free-stream velocity than those in the lowest one.

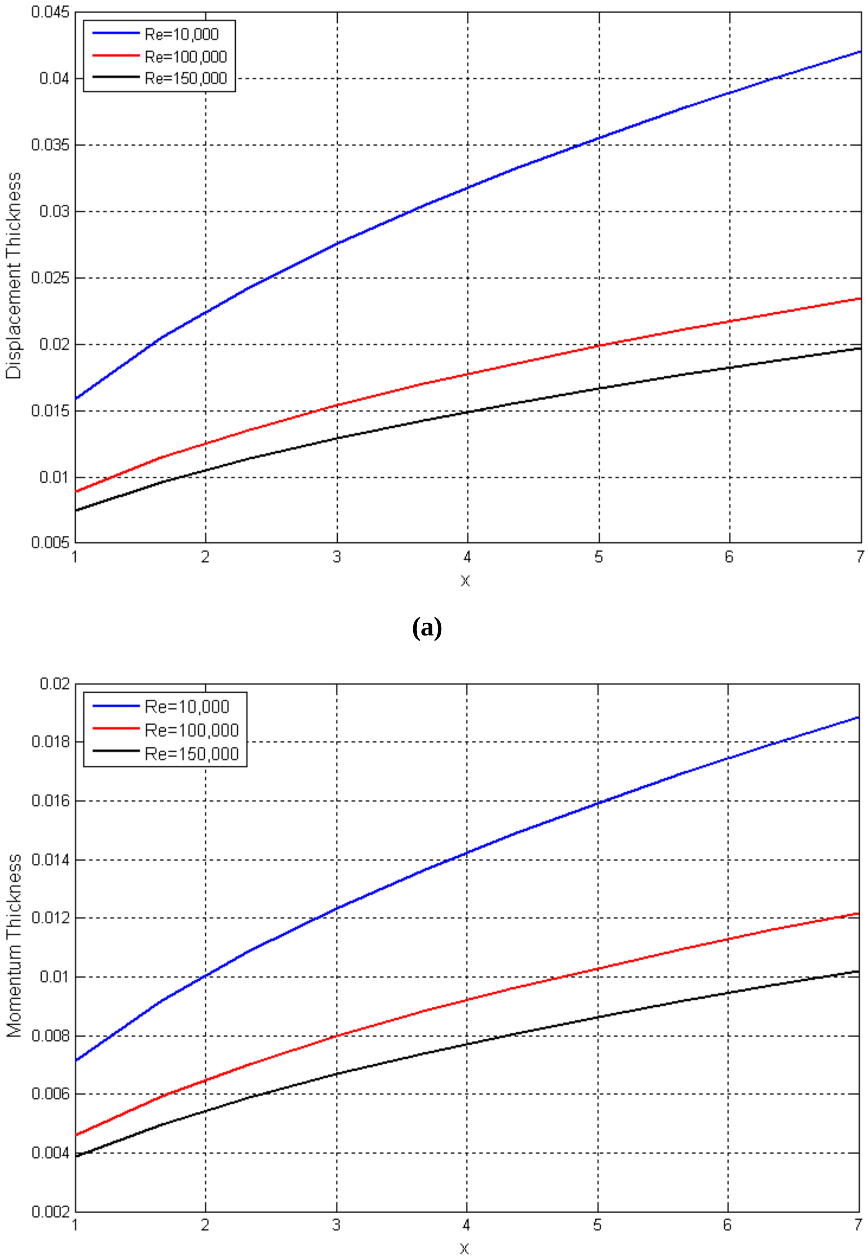

(a)

(b)

Fig. 28: Variation of the laminar mixing layer growth parameters in the streamwise direction with free-stream Reynolds number: a) displacement thickness, b) momentum thickness

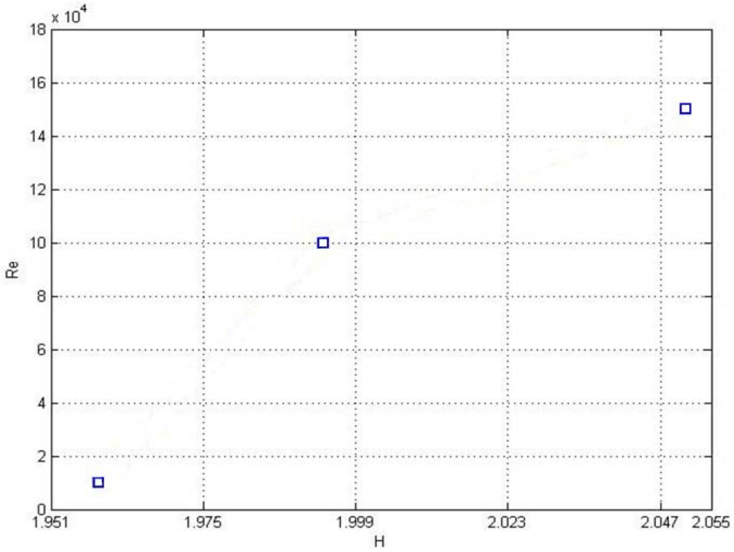

Fig. 29: Free-stream Reynolds number vs. shape factor for the laminar mixing layer

It is also important to assess the stability of the mixing layer by utilizing the well-known parameter, shape factor H, defined as the ratio of displacement thickness to momentum thickness. As plotted in Figure 29, shape factor increases with increase in the free-stream velocity. This confirms that the laminar mixing layer becomes unstable earlier in further upstream regions as free-stream Re increases.

Visual inspection of the plots also indicates approximately linear growth of displacement and momentum thicknesses after x=4m representing a self-preserving region within the laminar mixing layers (Milane, 2004). However, depending on the free-stream Re number, this location changes.

5.1.5. Effects of Free-Stream Temperature and Reynolds Number

In order to investigate the effects of the high-speed side free-stream temperature on mixing layer stability, numerical simulations were conducted in a range of high-speed side free-stream Reynolds numbers of 10,000, 100,000, and 150,000 with four different high-speed side temperatures: 250, 300, 350, and 400K. Growth rate parameters and shape factor were used to compare the results. Note that, low-speed side free-stream temperature is fixed at 300K.

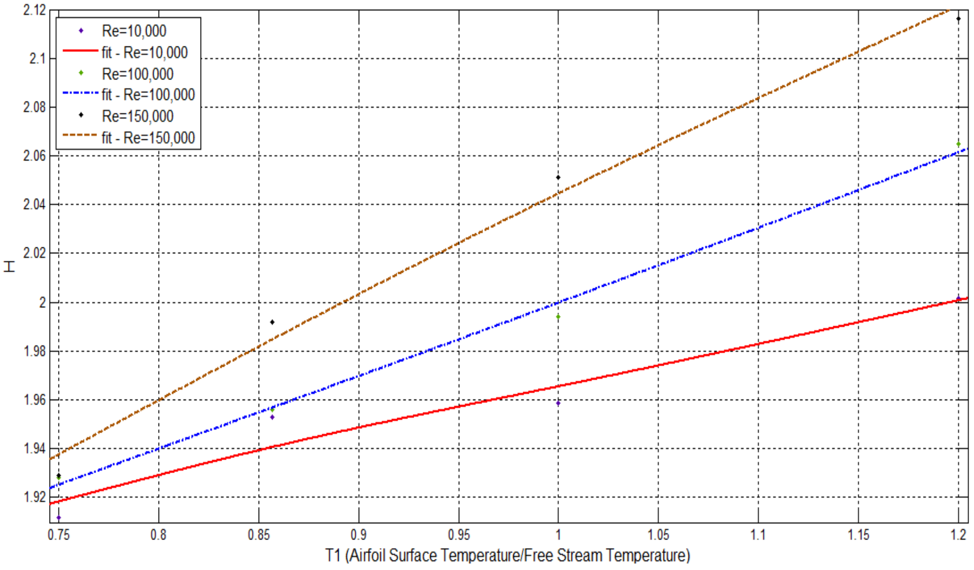

Fig. 30: Variation of shape factor vs. dimensionless temperature scale T1 for the laminar mixing layer

Figure 30 reveals the variation of shape factors for different operating free-stream velocities and temperatures. For all three Re numbers, shape factor increases with increasing T1. As illustrated, the rate of increase is higher for the highest Reynolds number. Note that dimensionless parameter T1, introduced by Lees and Lin (1964), is defined as ratio of airfoil surface temperature to high-speed side free-stream temperature.

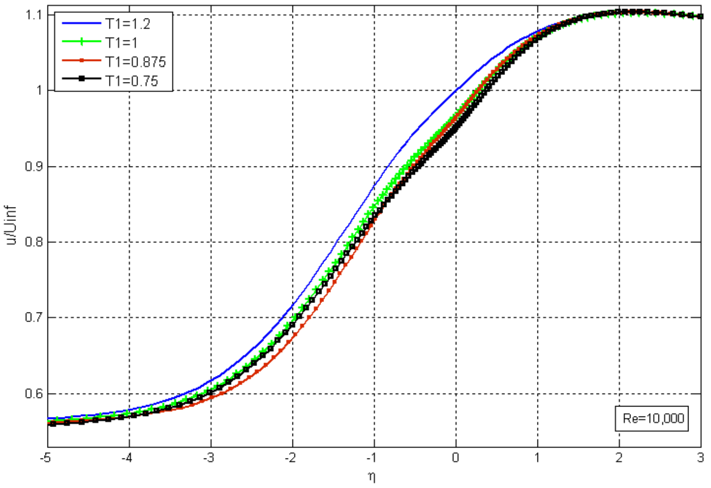

(a)

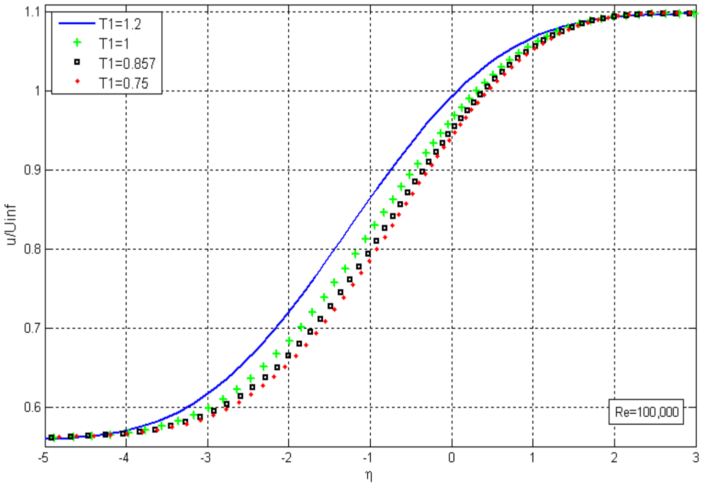

(b)

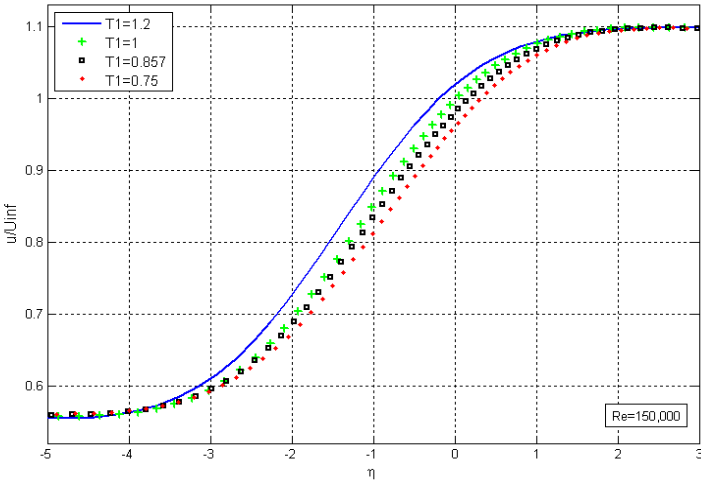

(c)

Fig. 31: Dimensionless velocity profiles of the laminar mixing layer at x=7m for different temperature scales T1=1.2, 1, 0.857, and 0.75: (a) Re=10,000, (b) Re=100,000, (c) Re=150,000

Corresponding velocity profiles at the end of the domain for different Re and temperatures are depicted in Figure 31. As shown, velocity profiles for all three Re numbers become retarded with increase in temperature. In other words, as expected, the studied mixing layer exhibits more stability for higher T1, i.e. for lower free-stream temperatures. Thus, velocity magnitudes indicating the onset of instability, and accordingly transition to turbulence, occur earlier and further upstream in the flow. The most stable profile is observed for the lowest free-stream temperature in all cases. At Re=10,000, increase in temperature over T=300K does not affect the shape of the profile as much as it does for the other higher Re cases. As a result, for the lowest Re number, velocity profiles show the least dependence on free-stream temperature. This dependence is more significant for higher Reynolds numbers.

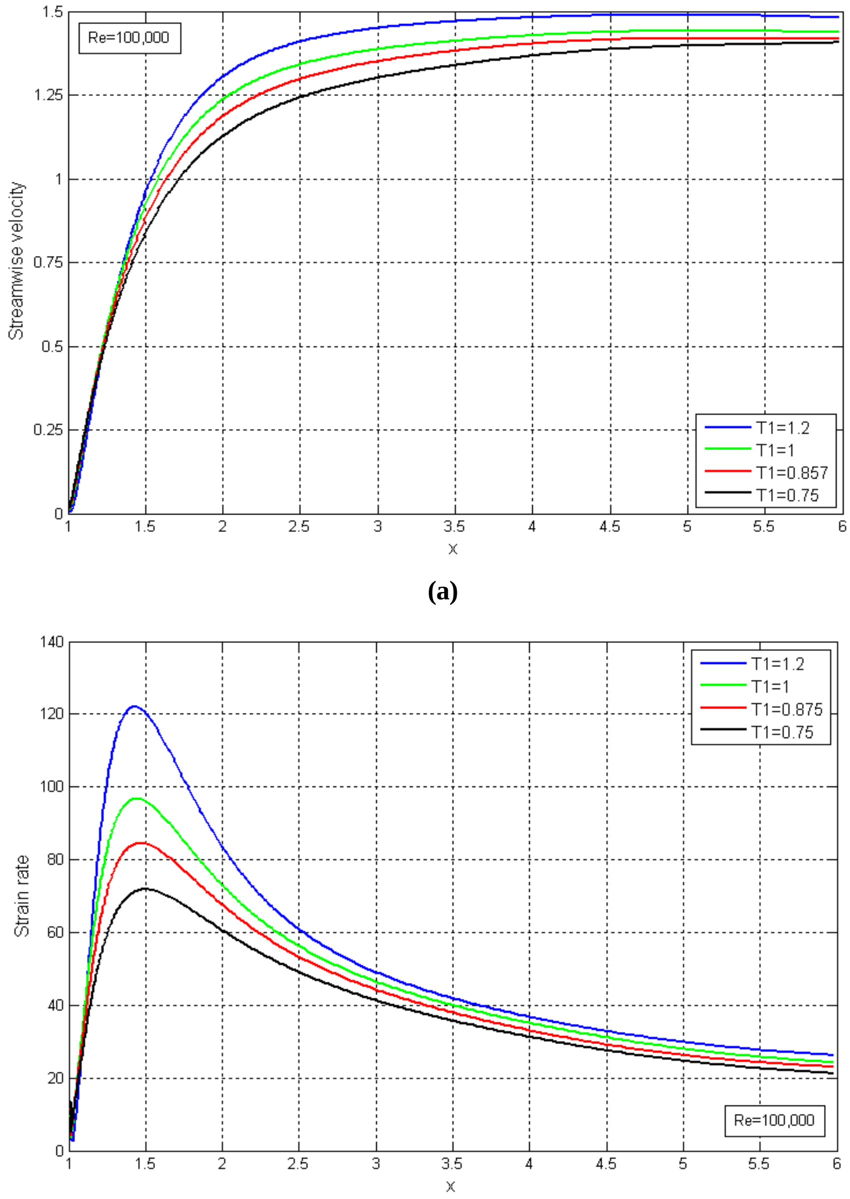

(a)

(b)

Fig. 32: Streamwise variation of flow parameters with free-stream temperature for the laminar mixing layer at Re=100,000; and *y*=0m: a) velocity magnitude, b) strain rate

Streamwise evolution of velocity magnitudes and strain rates with different free-stream temperatures at Re=100,000 along the centerline of the mixing layer are depicted in Figure 32. With regard to stabilizing effects of cooling the airflow on the mixing layer behavior, it is concluded that strain rate (and velocity magnitude) increases as the mixing layer becomes more stable. This increase is more apparent at the beginning of mixing close to the trailing edge of the airfoil. Such a behavior is attributed to the stabilization of the vortices due to decreasing the free-stream temperature. The same trends of velocity magnitude and strain rate variations were observed for the other two Reynolds numbers.

5.2. Three-Dimensional Mixing Layers

5.2.1. Numerical Solution - Unsteady

Unsteady three-dimensional mixing layers behind the 3D airfoil (wing) were studied using OpenFoam. Temporal evolution of the laminar mixing layer at free-stream Re=100,000 is provided as velocity contours in front, side (rear), and top views in Figure 33. As depicted, the most prominent features of 3D laminar mixing layers are: 1) roll-up of the layers just downstream of the trailing edge, due to the adverse pressure gradient that causes separation of the boundary layers on the airfoil; and 2) the presence of small three-dimensionality effects (spanwise coherent structures) produced mainly due to the curved airfoil geometry and its intersection with channel walls. However, because the flow regime is laminar (no inflow fluctuations) and there is no assumed initial crossflow in the spanwise z direction, mixing layer convection and diffusion in the streamwise direction are not affected considerably throughout the domain. In other words, the resultant mixing layer velocity profiles (and streamlines) can be estimated to be independent of the z coordinate and approximated by Blasius similarity solutions. Nevertheless, small values of spanwise velocity, $w(x,y)$, as shown in Figure 34, are reported. It is noted that reported flow times in the figures are non-dimensionalized by using a dimensionless time scale parameter, $\tau = \frac{tU_0}{\delta_0^*}$ (Brinkerhoff and Yaras, 2014) where U_0 and δ_0^* are free-stream velocity and its corresponding displacement thickness, respectively.

$\tau_1 = 21.52$

$\tau_2 = 210.2$

$\tau_3 = 421.4$

$\tau_4 = 646.1$

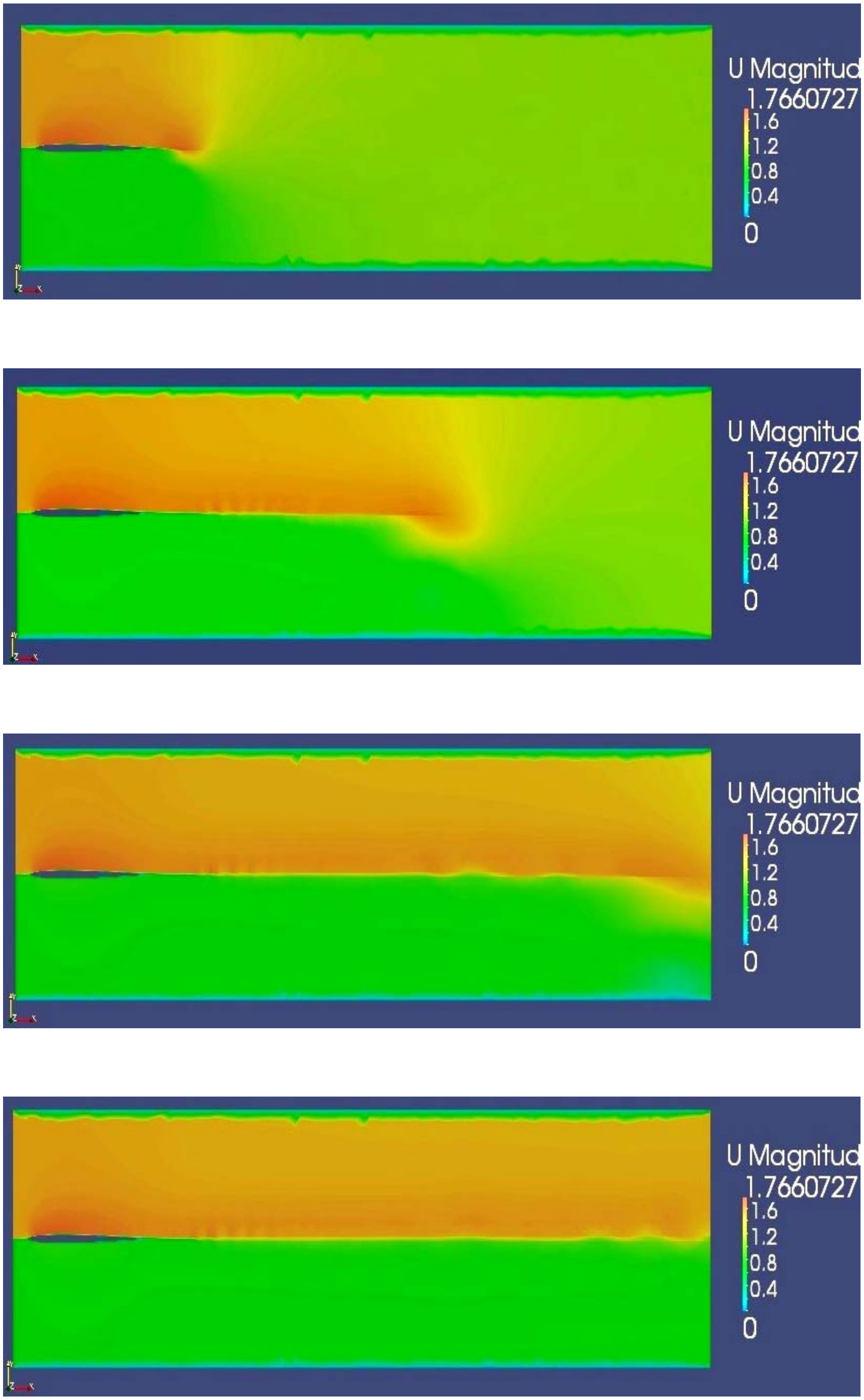

(a)

$\tau_1 = 21.52$

$\tau_2 = 210.2$

$\tau_3 = 421.4$

$\tau_4 = 646.1$

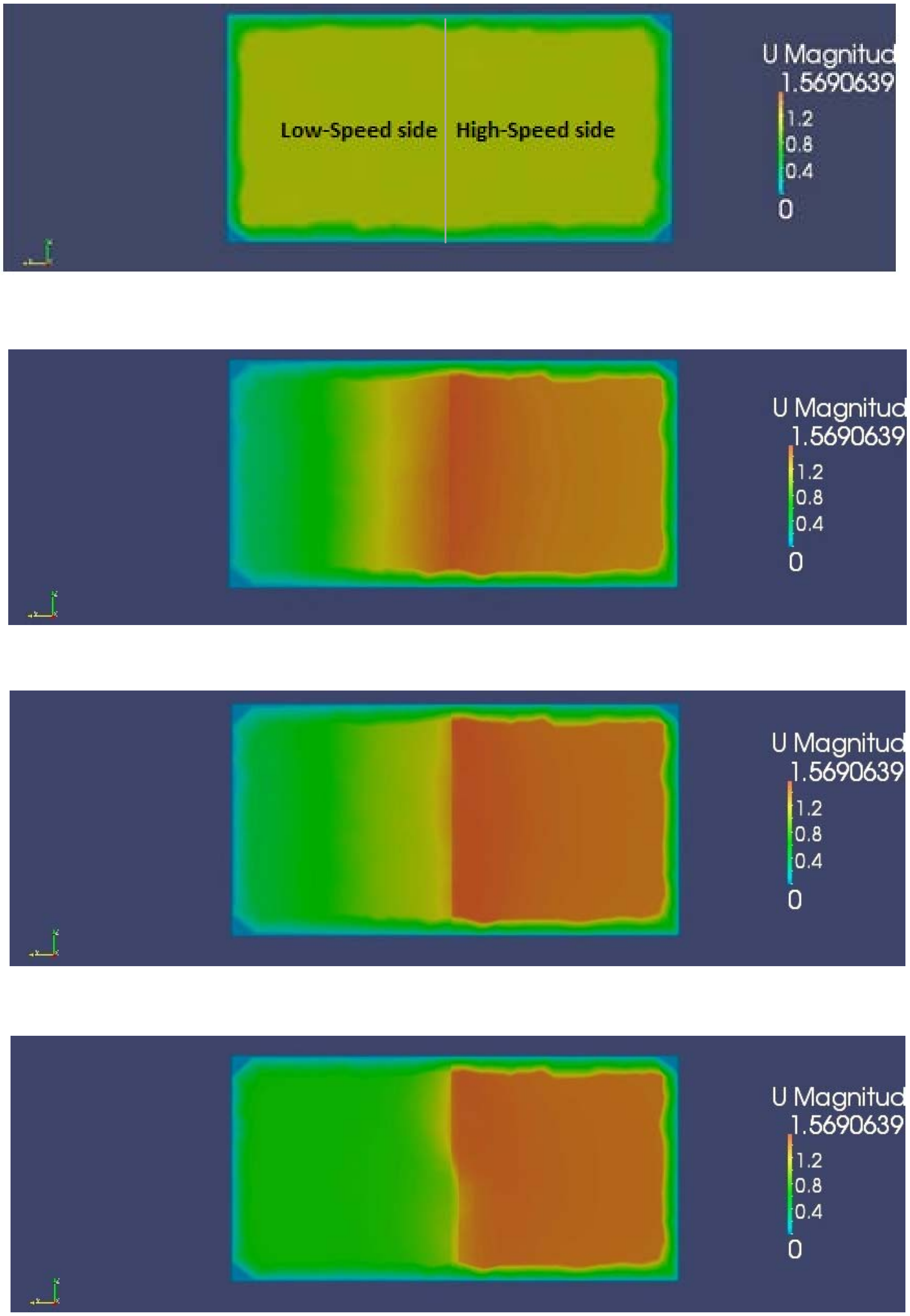

(b)

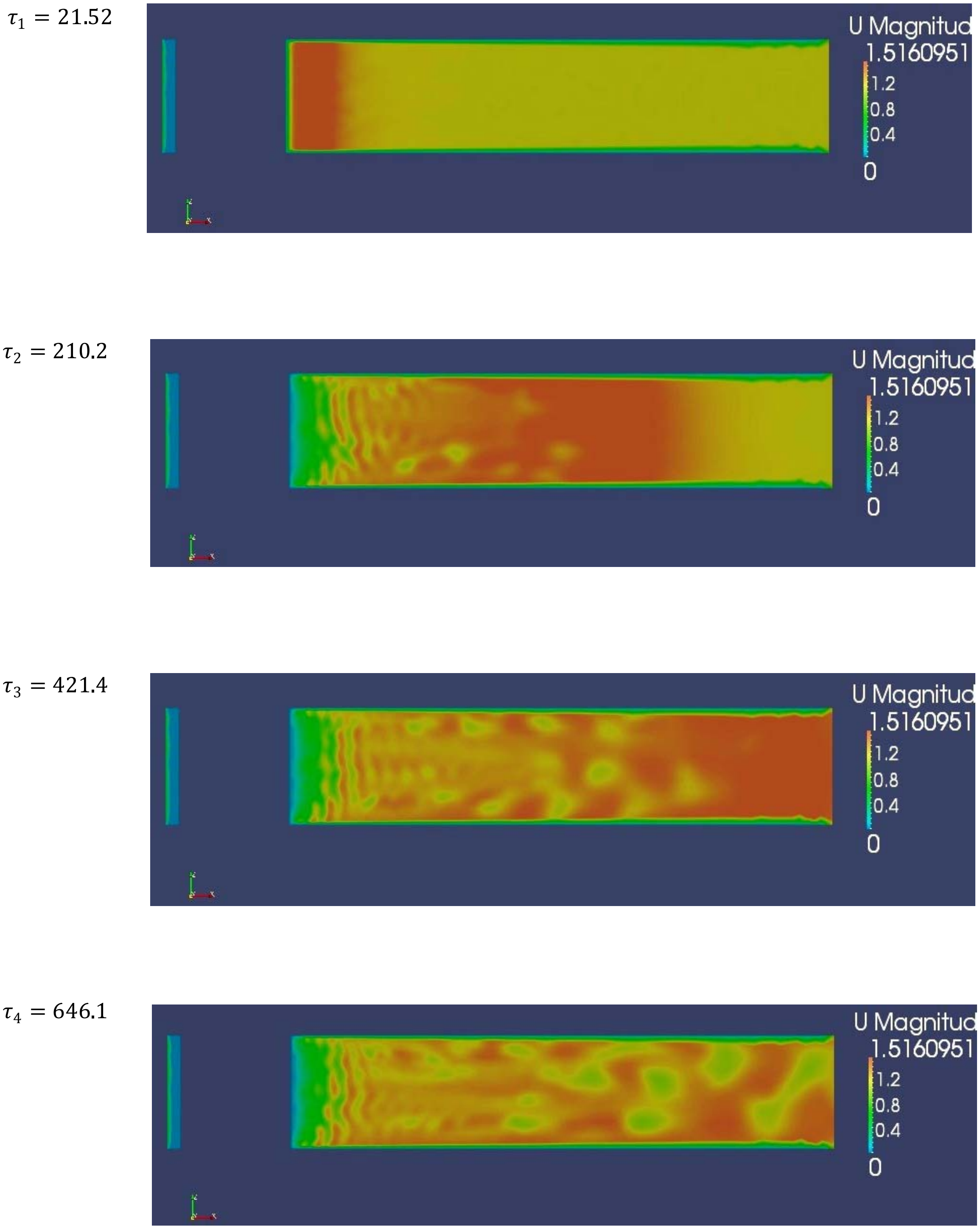

$\tau_1 = 21.52$

$\tau_2 = 210.2$

$\tau_3 = 421.4$

$\tau_4 = 646.1$

(c)

Fig. 33: Temporal evolution of the 3D laminar mixing layer in the streamwise direction - velocity contours for Re=100,000: a) front view (xy plane at z=0m), b) side (rear) view (yz plane at x=7m), c) top view (xz plane at y=0m)

The wavy-like behavior of the mixing layer (T-S waves) in both streamwise and spanwise directions in Figure 33 implies that the mixing layer at the trailing edge of the airfoil is initially accelerated and then stabilized as time proceeds. So, as will be illustrated later, the unsteady laminar mixing layer shows neither unstable nor alternate shedding in far downstream regions in comparison with the turbulent case. Besides, spanwise variation of the vortical structures decays quickly in the streamwise direction such that three-dimensionality effects are almost completely eliminated within a short distance.

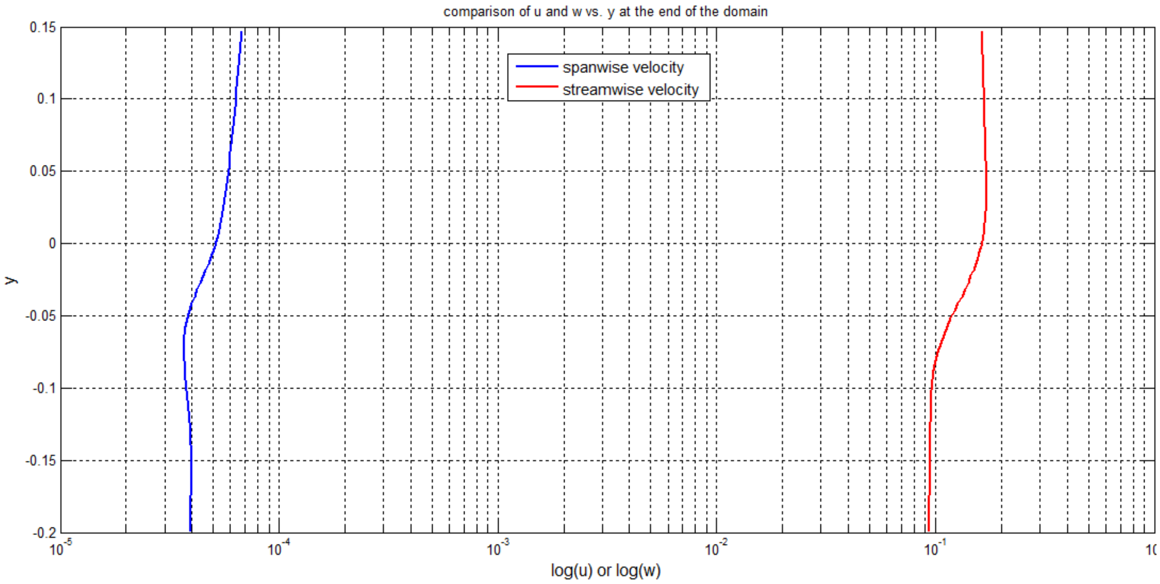

(a)

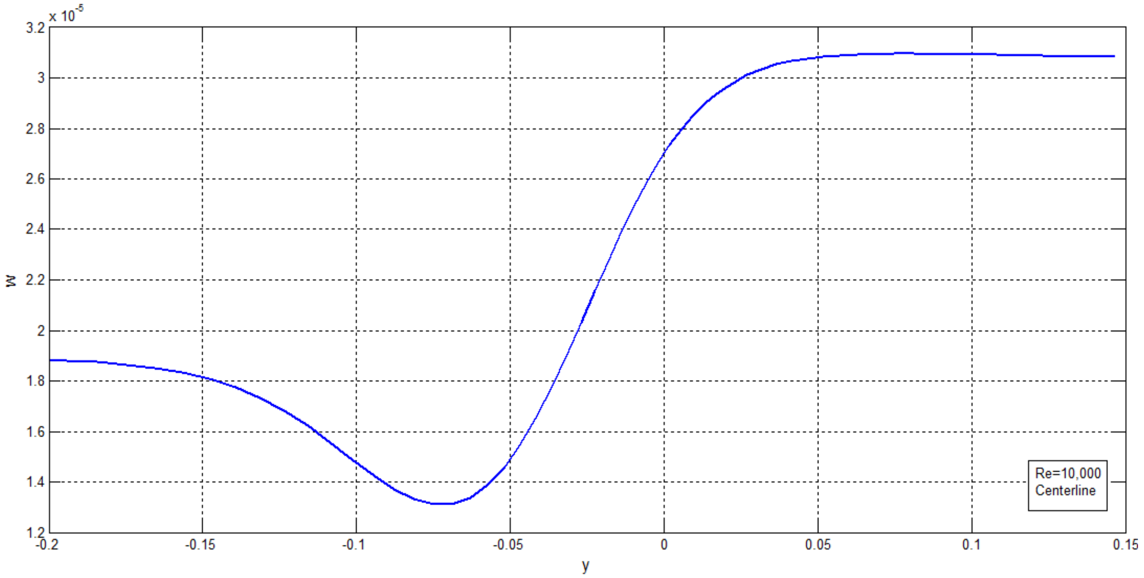

(b)

Fig. 34: Presence of three-dimensionality in the 3D laminar mixing layer at Re=10,000 – at the end of the last time step τ_4 =174.41: a) comparison of streamwise and spanwise velocity profiles, and b) $w(x, y)$ at x=7m, z=0m

5.2.2. Effects of Free-Stream Reynolds Number

Streamwise variations of velocity magnitudes and strain rates for Re=10,000 at the end of the last dimensionless time step τ =174.41 along the centerlines of three uniformly spaced planes z=0m, z=-0.2m, and z=-0.4m are shown in Figure 35. Included in the figure is also spanwise variation of velocity profiles in terms of y at the end of the domain. It is observed that corresponding curves at z=0m and z=-0.2m collapse pretty well on each other. This behavior changes clearly for the flows in the near-wall regions: for the streamlines adjacent to the channel wall (z=-0.4m), strain rate as well as velocity magnitude are reduced considerably compared to those on planes z=0m, z=-0.2m.

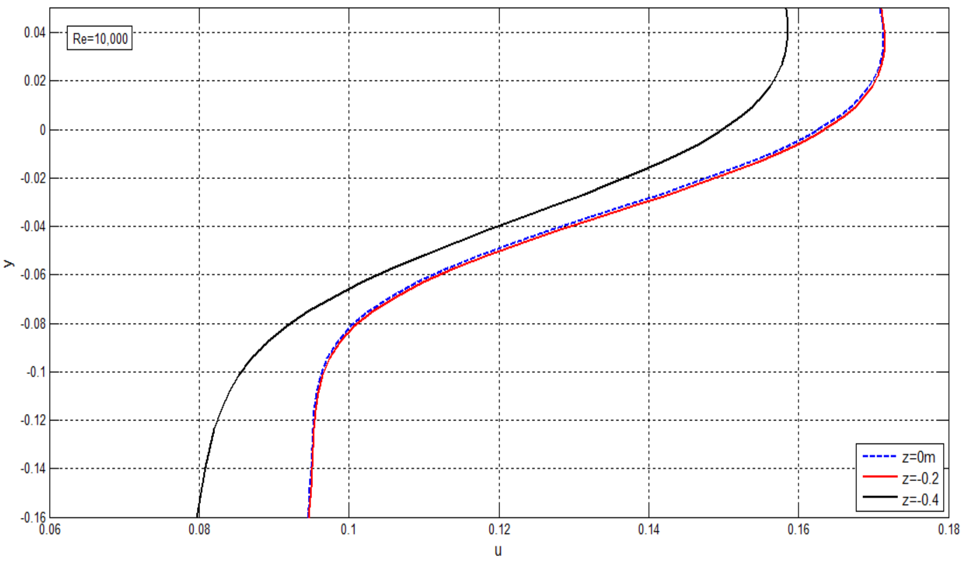
Re=10,000
y
u
0.04
0.02
0
-0.02
-0.04
-0.06
-0.08
-0.1
-0.12
-0.14
-0.16
0.06
0.08
0.1
0.12
0.14
0.16
0.18
z=0m
z=-0.2
z=-0.4

(a)

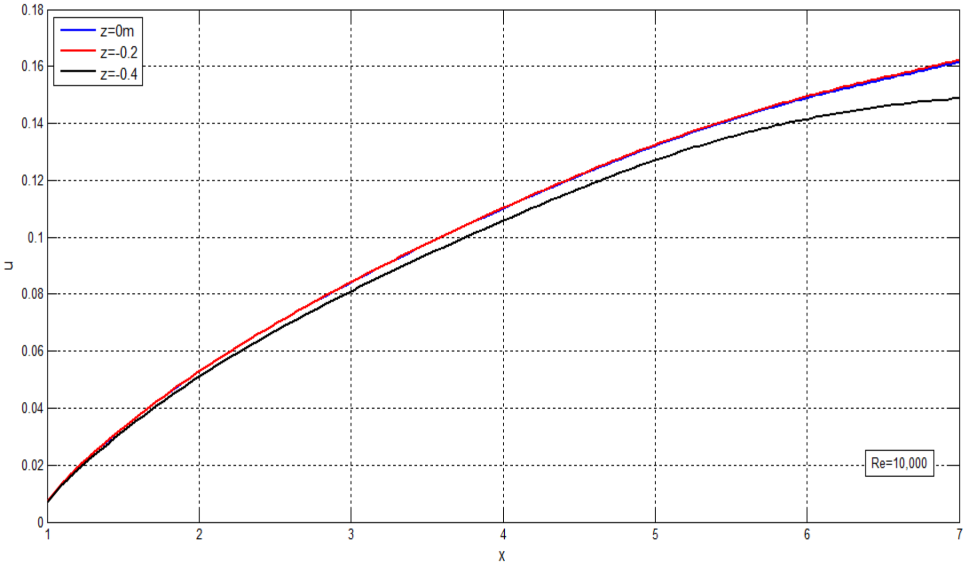
z=0m
z=-0.2
z=-0.4
Re=10,000
u
x
0.18
0.16
0.14
0.12
0.1
0.08
0.06
0.04
0.02
0
1
2
3
4
5
6
7

(b)

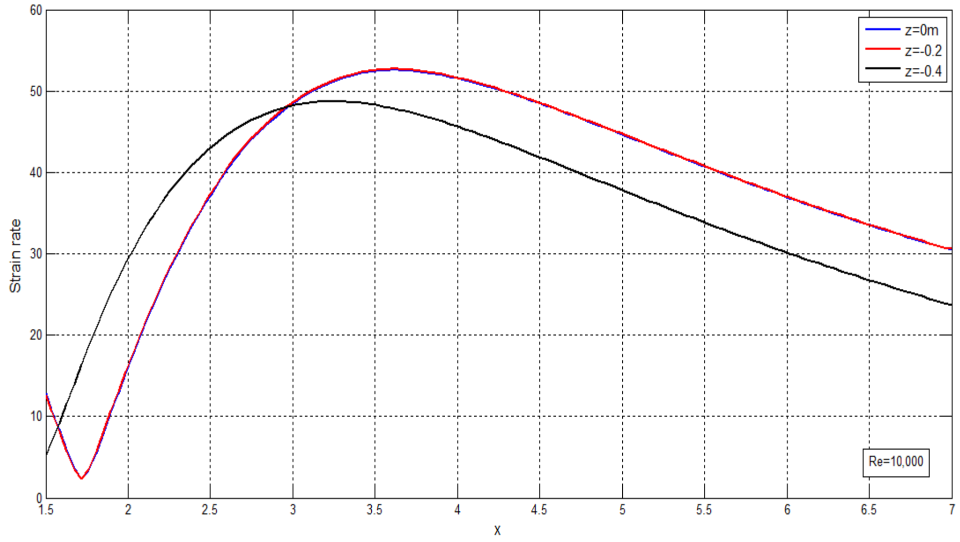

(c)

Fig. 35: Streamwise variations of flow parameters in spanwise direction for the 3D laminar mixing layer at Re=10,000 and τ =174.41: a) velocity profiles at the end of the domain in terms of y coordinate - b) velocity magnitudes, and c) strain rate, along the centerlines of planes z=0m, z=-0.2m, z=-0.4m

Moreover, maximum and minimum values of strain rate occur further upstream of the mixing layers. This can be explained by the fact that, in near-wall regions, additional interaction between the growing boundary layers on the channel walls and incoming free streams does not allow the strain rate to increase as much as it does on planes z=-0.2m and z=0m. Changing the free-stream Re number did not noticeably affect this trend.

Spanwise variation of streamwise velocity magnitudes for different high-speed side free-stream Re numbers at x=7m, y=0m is given in Figure 36. As shown, increasing the Re number causes the resistant viscous forces to decrease in comparison with the convective accelerating forces. It is therefore deduced that boundary layer development on the walls for Re=10,000, has the largest influence on the distribution of the velocity profiles. In other words, streamwise velocity magnitudes at Re=10,000 within the core of the mixing layers on plane y=0m are most affected by boundary layers formed on the channel walls. This observation is altered with increasing free-stream velocity.

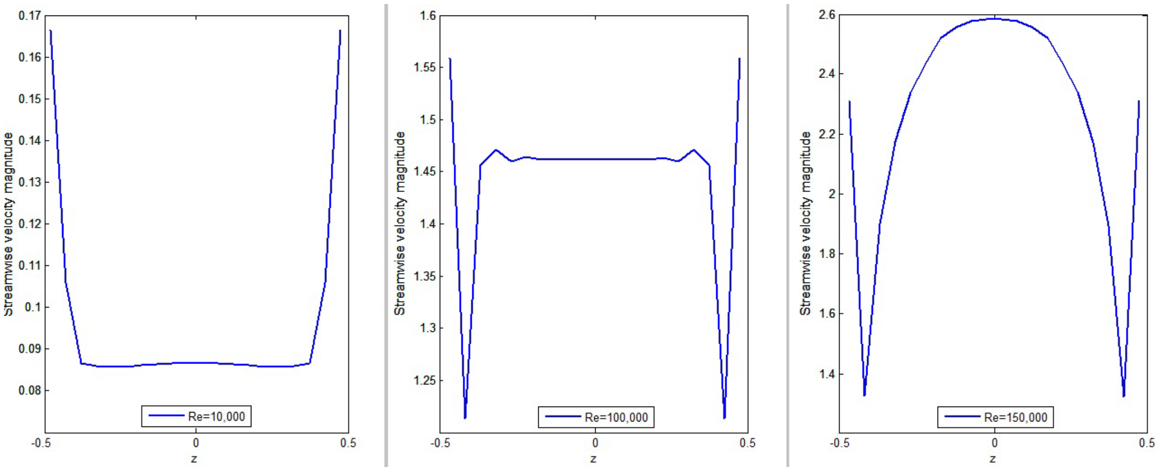

Fig. 36: Spanwise variations of streamwise velocity magnitude for the 3D laminar mixing layer at different Reynolds numbers (at x=7m, y=0m); and at the end of the last time steps $\tau_{Re=10,000}$ =174.41, $\tau_{Re=100,000}$ =326.06, and $\tau_{Re=150,000}$ =450

5.2.3. Mixing Layer Growth

Displacement and momentum thickness growth rates in the case of 3D laminar mixing layers were found for each of the Re numbers at $\tau_{Re=10,000}$ =174.41, $\tau_{Re=100,000}$ =326.06, and $\tau_{Re=150,000}$ = 450 by using Equations (5)-(7) as in the 2D case.

Spanwise variation of shape factors within the laminar mixing layer is given in Table VI. The shape factors were calculated in terms of the velocity profiles found at the last stations (x=7m) of three equally-spaced planes z=0m, z=-0.2m, z=-0.4m.

Reynolds Number	z - Spanwise Plane (m)	Shape Factor - H
Re=10,000	z=0	2.2353
	z=-0.2	2.2677
	z=-0.4	2.2576
Re=100,000	z=0	1.9297
	z=-0.2	1.9343
	z=-0.4	1.9409
Re=150,000	z=0	1.9334
	z=-0.2	1.9433
	z=-0.4	1.9565

Table VI: Variation of shape factor in the spanwise direction for the 3D laminar mixing layer at different Reynolds numbers; and at the end of the last time steps $\tau_{Re=10,000}$ =174.41, $\tau_{Re=100,000}$ =326.06, and $\tau_{Re=150,000}$ =450

As illustrated in the table, shape factor increases slowly in the spanwise direction for the streamlines closer to the channel walls. However, in the lowest Re number, the opposite behavior is seen at z=-0.4m. This is expected to be due to formation of a thick boundary layer adjacent to the channel wall (z=-0.5m). It is also evident that at higher Re, where the channel wall boundary layer thickness decreases, this contradiction is eliminated. Furthermore, streamwise changes of the growth parameters on the plane z=0m do not show any significant distinction from the 2D case.

Chapter 6: Turbulent Mixing Layers - Results and Discussion

6.1. RANS-Based Turbulence Models

Steady and unsteady solutions to the RANS equations in the case of 2D and 3D turbulent mixing layers are presented in this section. Numerical studies are conducted by utilizing corresponding RANS-based models in ANSYS-Fluent (2D cases) and OpenFoam (3D cases) to determine the behavior of the flow for different inlet turbulence intensities and high-speed side Reynolds numbers. The following turbulence models were applied in ANSYS-Fluent:

- **Spalart-Allmaras (S-A):** A one-equation RANS-based model in which the turbulent viscosity equation is added and solved by use of Boussinesq's theory. This model is used for external turbulent flows with low Re number and high adverse pressure gradients. The S-A model gives lower accuracy in calculations of gradient terms in the governing equations and consequently is less sensitive to the type and resolution of the grid (ANSYS-Fluent, 2014).
- **$\boldsymbol{k-\epsilon}$:** A quasi-empirical model that adds two equations to the RANS system of equations, one for dissipation rate and one for turbulent kinetic energy. The “Realizable $k-\epsilon$ model” is a developed model in this category solving new equations for turbulent viscosity (instead of Boussinesq's theory used in the S-A model), kinetic energy (k), and dissipations rate (ϵ). These new equations are derived from exact solutions for transport equations of mean squared vorticity fluctuations. In addition, this model imposes mathematical limits on Reynolds stress production in terms of applied turbulent flow specifications. The model is mostly used for flows with high Reynolds number and works well for boundary layer flows with adverse pressure gradients (ANSYS-Fluent, 2014).
- **$\boldsymbol{k-\omega}$:** An empirical two-equation RANS-based model developed in terms of the Wilcox model. The model is used for separating flows with low Reynolds number, e.g. bounded or free shear flows in addition to high-Re flows. To do that, corresponding transport equations for turbulent kinetic energy and specific dissipation rate are solved based on experimental correlations. Accuracy of the model is increased by adding turbulent production terms to the k and ω equations. This results in fewer dependencies

of the flow quantities, especially in the shear layers, on free-stream conditions (ANSYS-Fluent, 2014).

- **Transition $\boldsymbol{k-k_l-\omega}$:** A three-equation eddy-viscosity type model which solves the laminar kinetic energy (k_l) transport equation as well as corresponding turbulent kinetic energy and specific dissipation rate equations. An inverse turbulent time scale is also included in this model. Although the $k-k_l-\omega$ model works well for the prediction of laminar to turbulent transition onset, using this model in the case of fully turbulent flows might lead to non-feasible results (ANSYS-Fluent, 2014).
- **Shear Stress Transport (SST):** A four-equation RANS-based model that uses a blending function for the $k-\epsilon$ model for regions far from the walls and the $k-\omega$ model for near-wall regions to cover both high and low Reynolds number flows. The model is essentially developed in terms of the $k-\omega$ model. In spite of possible instabilities which may occur between the switching of the models, the SST gives more reliable results compared to the $k-\epsilon$ and the $k-\omega$ models, collapsing well with experimental results. In addition to solving the k and ω equations, a new definition of the turbulent viscosity equation and a Damped-Cross-Diffusion (DCD) derivative term are included in the governing equations of this model. Two equations are solved separately for the "turbulent intermittency" and "transition momentum-thickness Reynolds number" by which the onset of instability is estimated (ANSYS-Fluent, 2014).
- **Reynolds-Averaged Stress (RAS):** A second-moment closure RANS-based model adds five equations in 2D, and seven equations in 3D, to the Reynolds-Averaged Navier-Stokes transport equations. The efficiency of this model is mostly reported in simulations of flows with inhomogeneous/anisotropic Reynolds stresses i.e. highly-swirling, rotating flows. However, due to the presence of deficiencies in the initial assumptions of viscous and pressure-strain terms in the governing equations of this model, reliability of the results for different flow applications may change. The “Low Reynolds stress-Omega RAS” model is derived for separating flows on highly-curved geometries and wakes. Results of this type of RAS model, for different turbulent flow applications, are estimated to be in better agreement with analytical and experimental findings. This conclusion is due to the low Reynolds corrections and the existence of the $k-\omega$ model assumptions used in developing this model (ANSYS-Fluent, 2014).

Based on the accuracy of the results in the 2D case, **“Realizable $\boldsymbol{k-\epsilon}$”**, **“SST based on $\boldsymbol{k-\omega}$”**, and **“LGRSTM”** models were chosen to run the 3D simulations in OpenFoam. Among the mentioned RANS models, Spalart-Allmaras, with the lowest number of equations, was expected to show the least accuracy whereas RAS and LGRSTM were expected to show the highest level of accuracy. Note that, the initial conditions used in the S-A model are assumed to hold for the other RANS-based models. Self-similarity of the mean velocity and Reynolds stress profiles were also verified with previous experimental investigations.

6.1.1 Two-Dimensional Mixing Layers

6.1.1.1. Numerical Solution - Steady State

Figure 37 displays non-dimensional mean velocity profiles at x=6.75m which are found by applying the RANS-based models. The figure shows the mean velocity profiles at high-speed side free-stream Re=500,000 and the following range of inflow turbulence intensities: I=2%, I=10%, and I=15%. In order to determine accuracy and reliability of the various models, experimental results of Hollingsworth and Bourgogne (1995) are provided in the figure. Moreover, the present findings are comparable with experimental investigations of Mehta and Westphal (1986) and Plesniak and Johnston (1988) on mixing layers behind flat splitter plates. Note that in order to normalize the results, the dimensionless scale parameter defined by Hollingsworth and Bourgogne (1995) was used:

$$\xi = \frac{y - y_0}{\delta_w} \qquad (56)$$

where the center of the turbulent mixing layer, y_0, is determined by $\bar{u}(x, y_0) = \frac{U_{high-speed\ \ side} + U_{low-speed\ \ side}}{2}$ and vorticity thickness of the turbulent mixing layer, δ_w, is given by:

$$\delta_w = \frac{U_{high-speed\ \ side} - U_{low-speed\ \ side}}{(\partial \bar{u}/\partial y)_{max}} \; . \tag{57}$$

Additionally, to minimize the effects of upper and lower walls of the channel, velocity profiles are taken within y range of -0.5 and 0.5m, as done in the laminar case. It should be mentioned that the RANS-based model results are reliable in flow regions far enough from the walls (Akhtar, 2010). Thus, the focus of the present validations is on the velocity profiles found in the core regions of the mixing layers. Note for clarity, only velocity profiles found by RAS, SST, and $k-\omega$ models are shown in Figure 37.

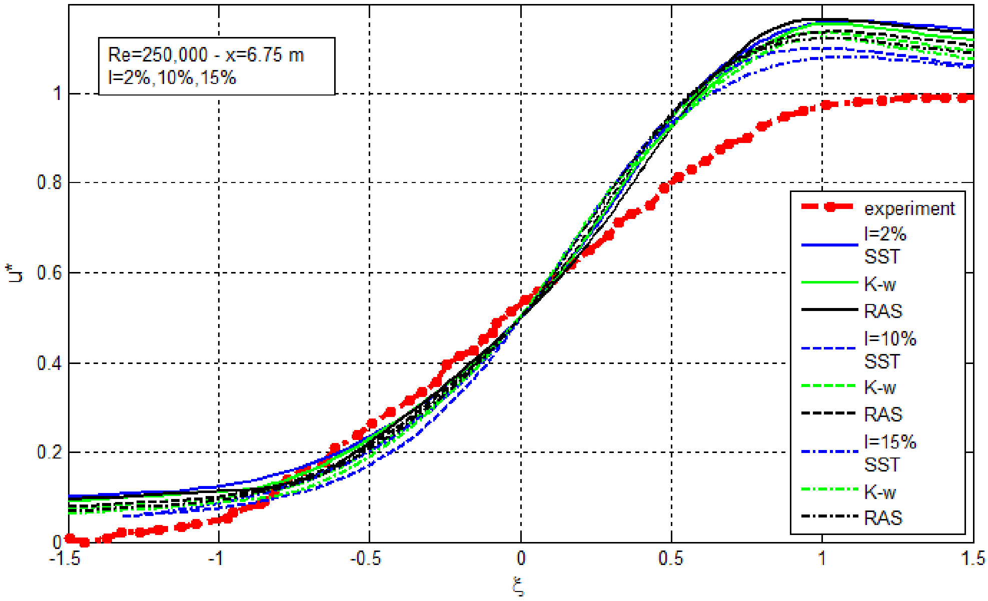

Fig. 37: Comparison of dimensionless mean velocity profiles for the turbulent mixing layer at free-stream Re=250,000 and different turbulence intensities *I* at the last station of domain: RANS-based models RAS, SST, k − ω with experimental data of Hollingsworth and Bourgogne (1995)

Although different models predict the same trend for mixing layer behavior at x=6.75m, the S-A model over predicts this behavior. The reason for this is due to the nature of the Spalart-Allmaras model which is an accurate means to predict external flow problems (i.e. airfoil subjected to far-field boundary conditions). In addition, sudden changes of the turbulent length scales, particularly in bounded shear flows, cannot be predicted by S-A. Likewise, two-equation RANS-based models, such as $k-\epsilon$ and $k-\omega$, over predict the eddy viscosity values because turbulent shear stress is not precisely resolved in these models (Akhtar, 2010). The transition $k-k_l-\omega$ model predicts the velocity profiles well, but shape factors found by using this model are in an unrealistic reversed trend in comparison with the other four RANS-based models. This can be interpreted by the presence of a turbulent time-scale variable in the governing equations of this model that decreases intermittency in the outer regions of the turbulent boundary layers. Thus, the wake region effects on the mean velocity profiles are approximately excluded. Despite the expectation of highest level of accuracy for RAS modeling, results of the SST model collapse relatively better with the experimental data. This conclusion could be explained by the fact that in the SST model, onset and amount of flow separation on smooth surfaces, and also shear strains in different pressure gradients are computed more precisely in comparison with other lower order models. These models do not account for the turbulent shear stress transport (Akhtar, 2010). Furthermore, the empirical correlations used in deriving "turbulence intermittency" and "transition momentum-thickness Reynolds number" governing equations of this model control the transition region length and onset of instability. It should be pointed out that critical Reynolds number can be estimated at the point where the turbulent intermittency starts increasing (ANSYS-Fluent, 2014).

With regard to accuracy of the results found by SST and RAS models, Figure 38 depicts the non-dimensional mean velocity profiles at the last station of the domain (x=6.75m) at high-speed side free-stream Re=500,000 and different free-stream intensities, obtained by the SST model. Note that the behavior of the mean velocity profiles is approximately the same as for the RAS model results. Included in the figure is the data of Görtler’s study (1957), which employed an eddy-viscosity analytical solution for an equilibrium turbulent mixing layer behind a flat plate:

$$u_G^* = \frac{\bar{u} - U_1}{U_2 - U_1} = \frac{1}{2}\left[1 + \mathrm{erf}\left(\frac{\sigma y}{x}\right)\right] \tag{58}$$

where U_1 and U_2 are lower and upper side free-stream velocities, respectively.

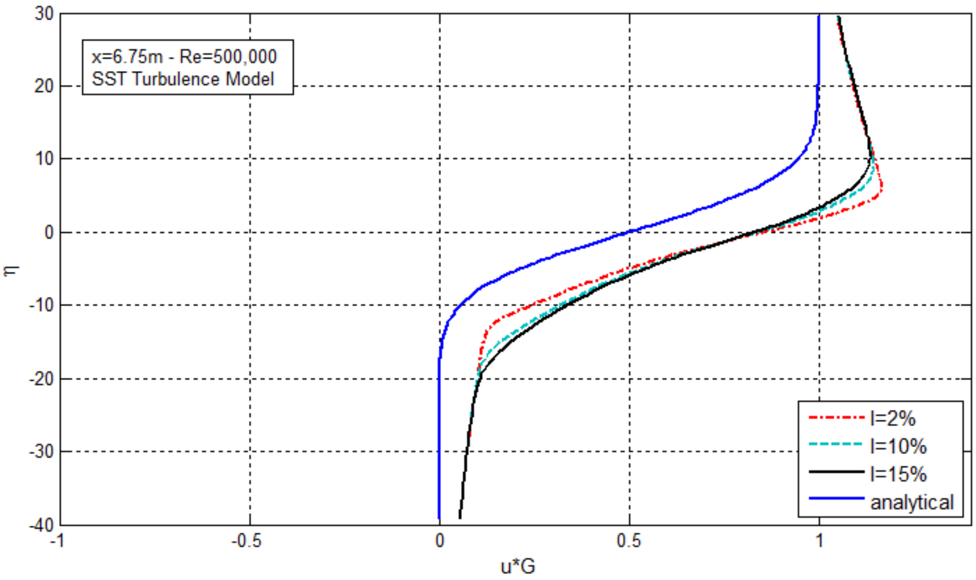

Fig. 38: Comparison of dimensionless mean velocity profiles of the turbulent mixing layer at x=6.75m for Re=500,000 and different free-stream intensities - found by using SST turbulence model - with approximated analytical solution of Görtler (1957)

Although the mixing layer of the present study is estimated to be non-equilibrium, the results obtained match relatively well with Görtler's data. The difference may be due to gradual changes of the gradients across the mixing zone, particularly in further downstream regions. In using Görtler's solution, the best value for the spreading parameter (σ) was determined by examining different values of σ iteratively and then visually inspecting the findings to attain the best fit among the mean velocity profiles (Akhtar, 2010). Thus, σ=21 was selected for the present study, which is close to the suggestion of Roig et al. (1998). However, according to Birch and Eggers' (1973) approach, the spreading parameter could be 11 or even less in the tripped mixing layers.

6.1.1.2. Mixing Layer Growth

In order to find mixing layer growth rate, Equations (5)-(7) were used to investigate streamwise variation of displacement, momentum thicknesses, and shape factor. Steady-state simulations were conducted in ANSYS-Fluent by examining different turbulence models. As indicated in Figure 39, shape factor H decreases in the streamwise direction. Such a decreasing trend, also reported in Thole's study (1992) on high-intensity turbulence, illustrates a faster increasing rate in displacement thickness in comparison with the momentum thickness due to gradual increase of the streamwise pressure gradients. Note that, an increasing trend of the momentum thickness across the turbulent boundary layers on the flat plate is also reported in the analytical work of Das (1988) and the RAS turbulence modeling of Kline et al. (1982). As shown in Figure 40, the increasing trend of the momentum thickness is triggered by increasing free-stream turbulence intensity whereas displacement thickness declines. Figure 39 also suggests that the variation of the shape factor, for the assumed range of the intensities, is negligibly affected by free-stream Reynolds number. Moreover, it is illustrated that all models, except S-A and $k - k_l - \omega$, predict relatively the same trends for shape factor, displacement and momentum thicknesses.

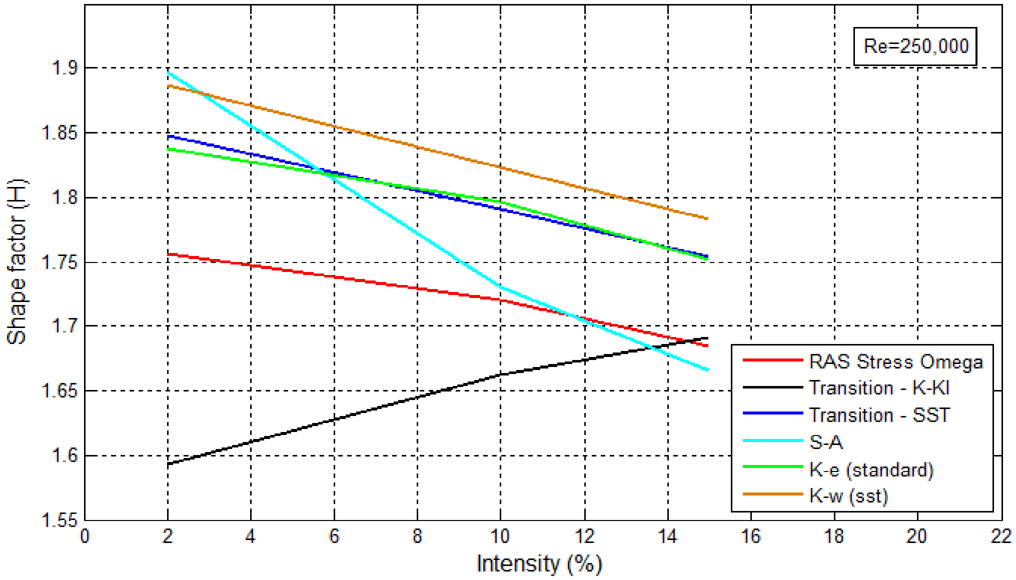

(a)

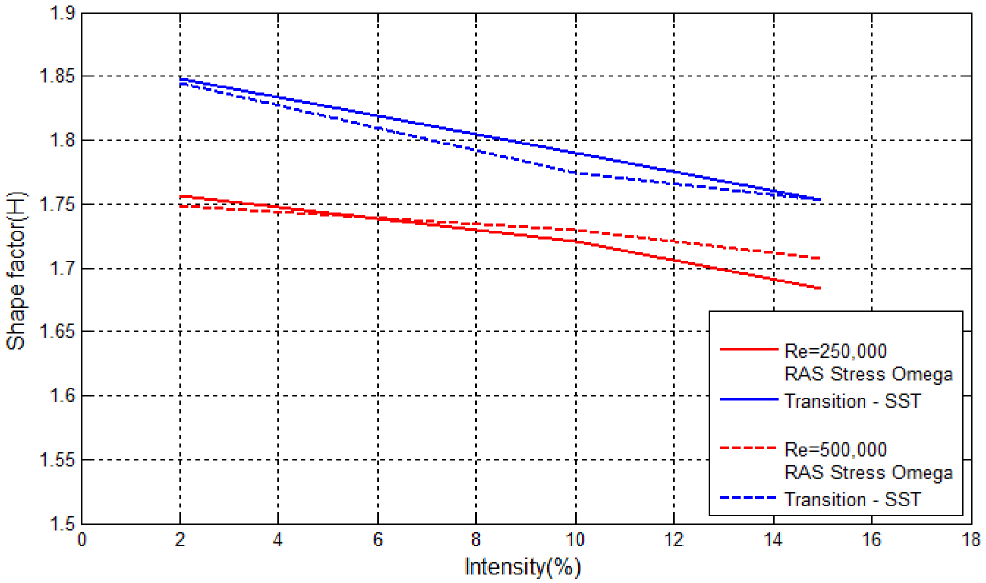

(b)

Fig. 39: Variation of shape factor with turbulence intensity for the turbulent mixing layer: a) at Re=250,000 using different RANS-based turbulence models, b) at Re=500,000 and Re=250,000 using RAS and SST turbulence models

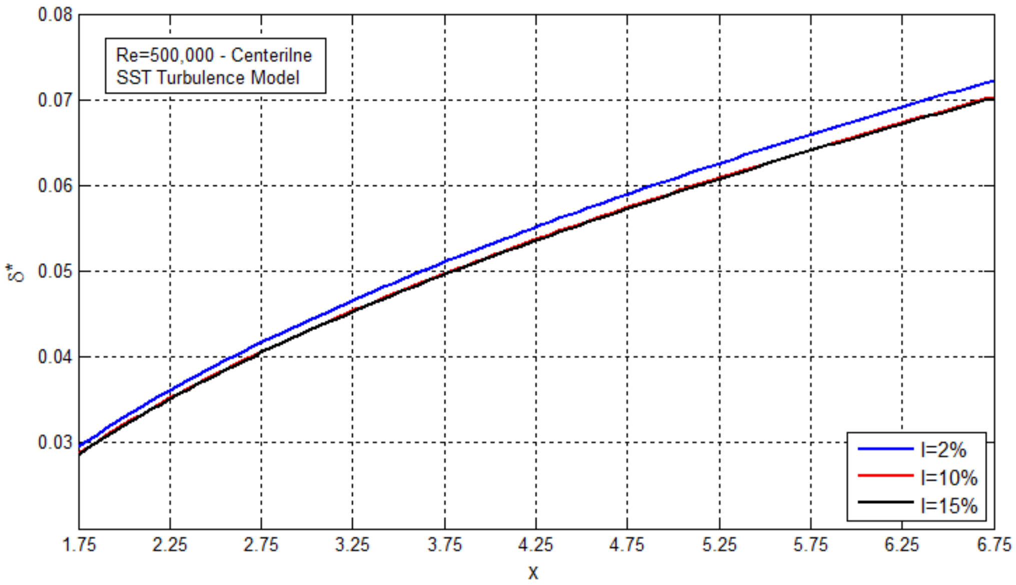

(a)

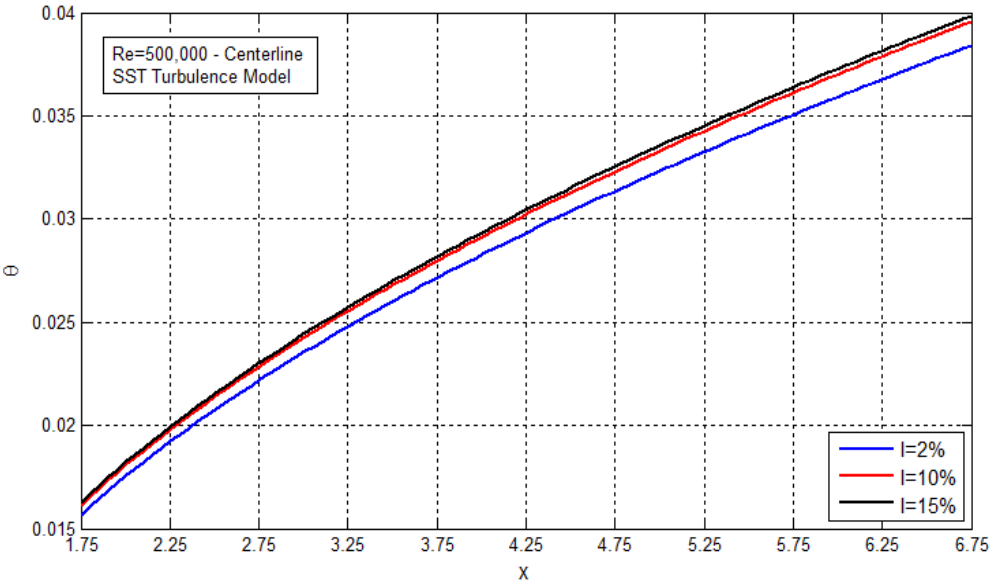

(b)

Fig. 40: Streamwise variation of a) displacement thickness, b) momentum thickness, for the turbulent mixing layer at Re=500,000 and different free-stream intensities using the SST turbulence model

The observed behavior for growth rate parameters along with increase in the momentum thickness Reynolds number, Re_θ, in the streamwise direction are also reported in the experiment of Hollingsworth and Bourgogne (1995). In addition, the results indicate that the mixing layers in the turbulent regimes are relatively thicker than those in the laminar regimes.

6.1.1.3. Effects of Free-Stream Reynolds Number and Turbulence Intensity

Streamwise evolution of the dimensionless mean velocity profiles for high-speed side Re=500,000 and a range of free-stream intensities at different stations x=1.25m, 3m, 4m, 5m, 6m, 6.75m is provided in Figure 41. The SST turbulence model was used to explore these variations. Mean velocity profile variation in the low-speed side display almost the same shapes as in the laminar case. In the high-speed side portion of the profiles, asymptotic behavior at x=1.25m is observed to be deviated toward the upstream regions as streamwise (x) distance increases. This observation is in contrast with previous observations of laminar mixing layers, and occurs due to global distribution of the turbulent viscosity, acting as a resistant shear force for the outer-layer regions of the turbulent mixing layers.

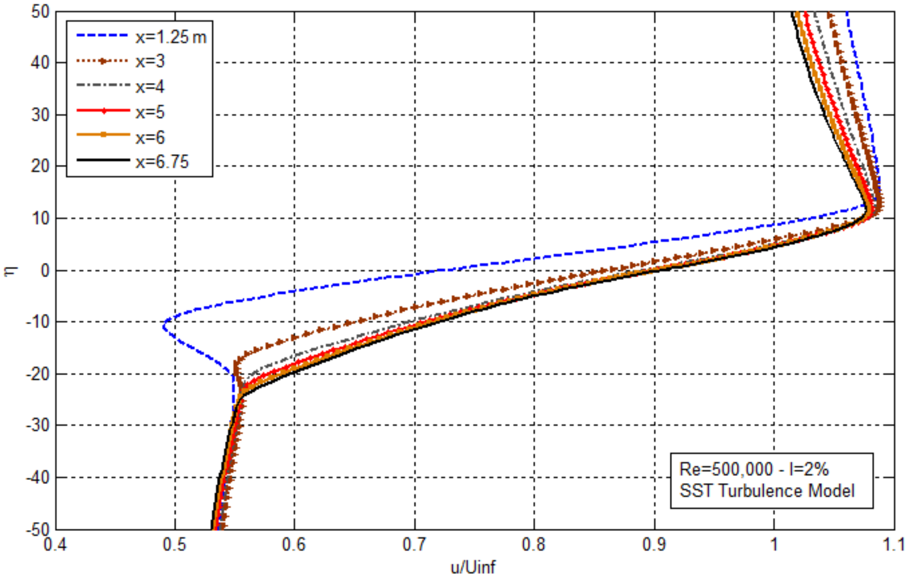

(a)

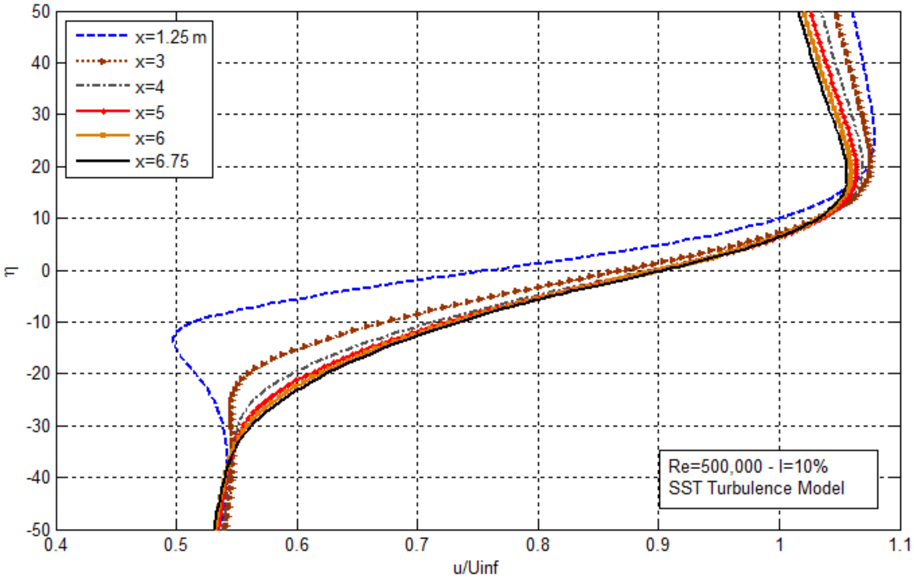

(b)

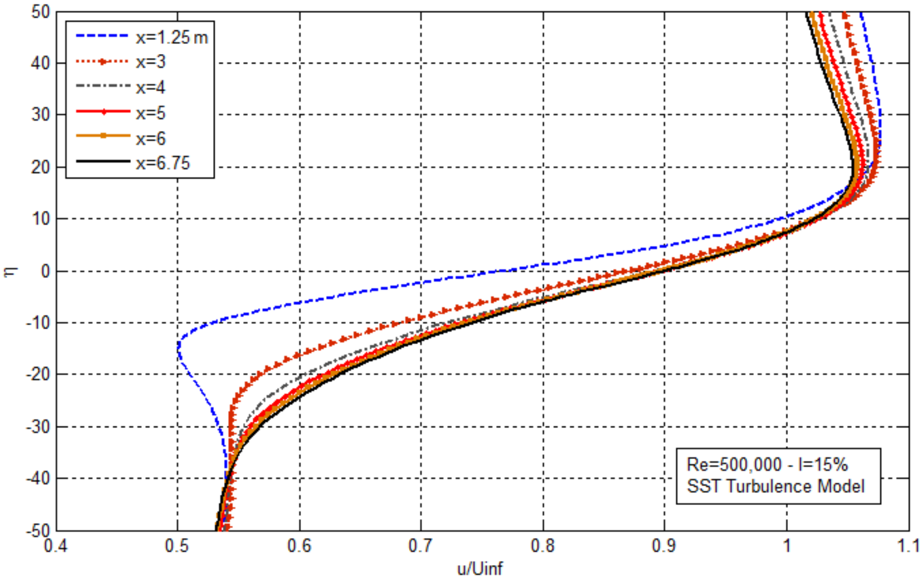

(c)

Fig. 41: Streamwise distribution (x=1.25, 3, 4, 5, 6, 6.75m) of dimensionless mean velocity profiles for the turbulent mixing layer at Re=500,000 and a range of turbulence intensities using the SST turbulence model: a) *I*=2%, b) *I*=10%, c) *I*=15%

Compared to the laminar case, due to the turbulent nature of the flow, steeper slopes of the profiles are observed as shown in Figure 41. In addition, effects of the boundary layer growth along the channel walls are such that the mean velocity profiles, particularly in the high-speed side, need more time to show an asymptotic behavior. Nevertheless, increasing the domain length is estimated to improve this approach. A negligible difference is observed between the profiles at free-stream turbulence intensities of 10% and 15%, respectively. Distinction becomes evident in the velocity profiles at *I*=2%.

Influence of the free-stream Reynolds number on the last station (x=6.75m) velocity profile at *I*=15% is depicted in Figure 42. As seen, for higher Re numbers, dimensionless mean velocities of the high-speed side become closer to their asymptotic value (around 1.1) such that the overshoot seen in the upper portion of the graph is reduced. This approach was similarly observed in the laminar mixing layers results. The same variations were observed for other intensities.

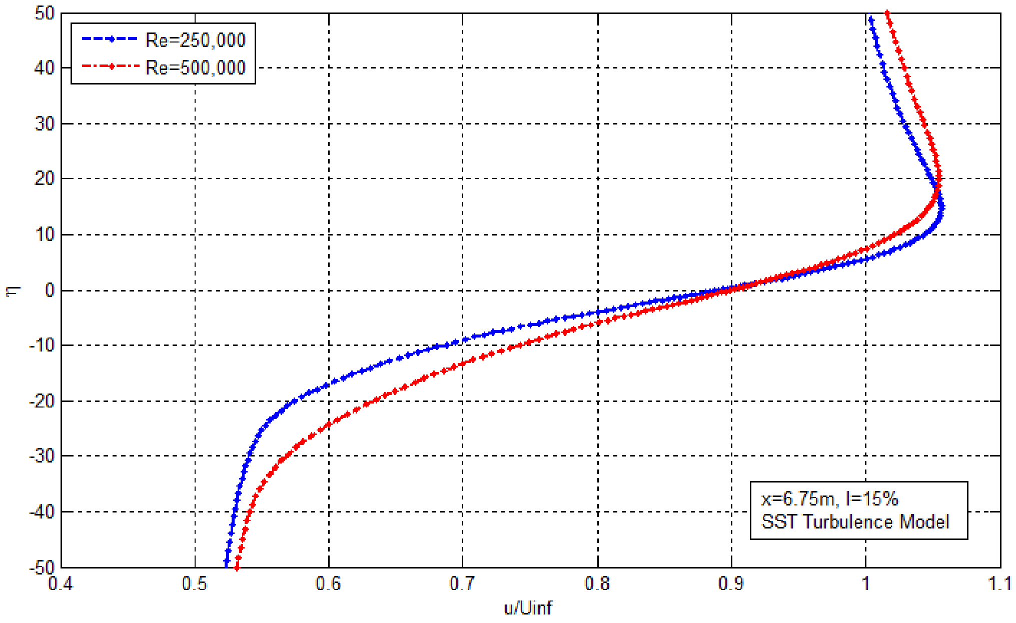

Fig. 42: Behavior of dimensionless mean velocity profile for the turbulent mixing layer at different free-stream Reynolds numbers with *I*=15% at x=6.75m, using the SST turbulence model

Furthermore, the self-preservation of the velocity profiles for higher Reynolds numbers (or in higher turbulence intensities) occurs at longer distances in comparison with the laminar cases. This conclusion can be explained by the fact that streamwise pressure gradients, and consequently streamwise velocity gradients, in turbulent flows are higher than those in laminar flows. Thus, mixing layers in turbulent regimes are accelerated more and carry more momentum. As a result, more time and distance are required for the flow to exhibit self-similarity.

For high-intensity turbulent mixing layers, higher growth rate of the mixing layer thickness can be predicted. This occurs because of the higher entrainment caused by stronger fluctuations (Pui and Gartshore, 1979).

Figure 43 displays the changes of mean velocity, strain rate, turbulent kinetic energy, and turbulent viscosity with free-stream turbulence intensity for Re=500,000 along the centerline of the mixing layers using the SST model. Variation of the strain rate $(\frac{\partial \bar{u}}{\partial y})$ for all of the cases shows a very sharp increase upstream regions of the mixing layer, right after the airfoil trailing edge, and then starts decreasing with streamwise (x) distance. In other words, the small non-sheared region just behind the airfoil, observed in the case of the laminar mixing layers, does not distinctly appear in the turbulent case. Strain rates display almost the same trends in mixing layer upstream regions up to a maximum, at which vortical structures are produced. Soon after that, they decrease with increased intensity. This is estimated to occur mainly due to the streamwise reduction of vorticity strength in the wake area behind the airfoil at higher turbulence intensities. Furthermore, in the highly-turbulent environment where I=15%, viscous forces produced at the interface of the mixing layers are dominated extensively by convective forces that are accelerating the flow. This consequently causes a decrease in the shear forces (strains) at the interfacial region. Needless to say, higher vorticity magnitudes and strain rates are predicted at higher Re numbers.

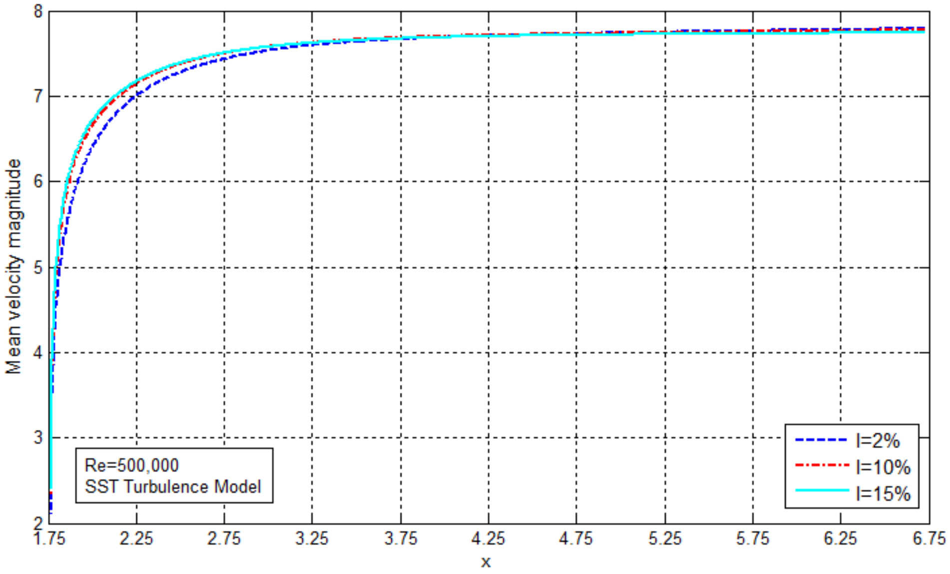

(a)

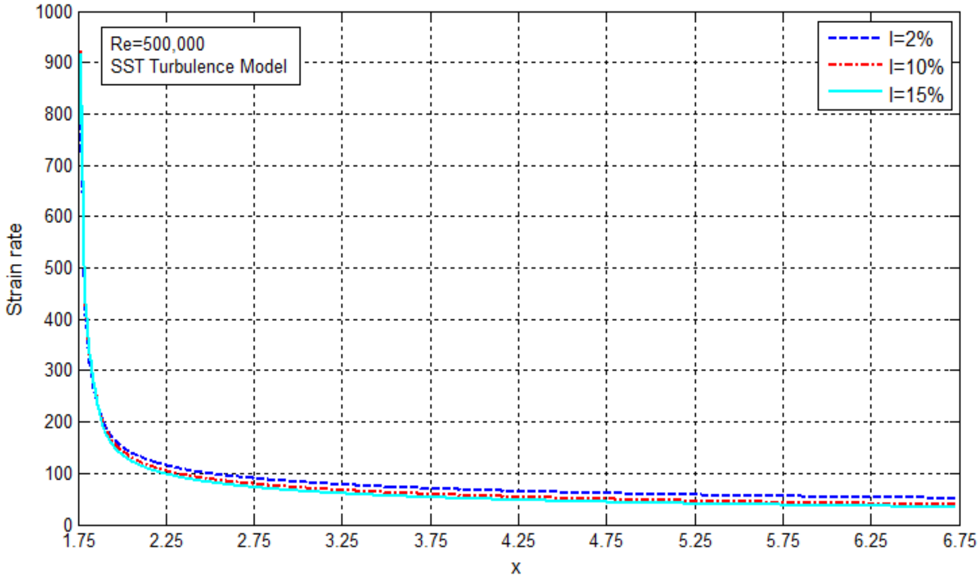
Re=500,000
SST Turbulence Model
I=2%
I=10%
I=15%
Strain rate
x
1000
900
800
700
600
500
400
300
200
100
0
1.75
2.25
2.75
3.25
3.75
4.25
4.75
5.25
5.75
6.25
6.75

(b)

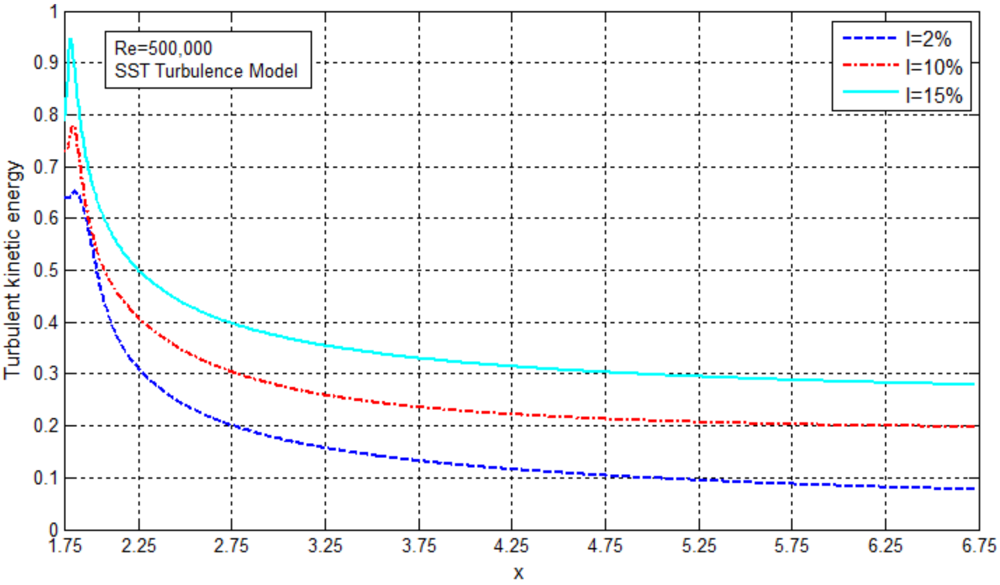
Re=500,000
SST Turbulence Model
I=2%
I=10%
I=15%
Turbulent kinetic energy
x
1
0.9
0.8
0.7
0.6
0.5
0.4
0.3
0.2
0.1
0
1.75
2.25
2.75
3.25
3.75
4.25
4.75
5.25
5.75
6.25
6.75

(c)

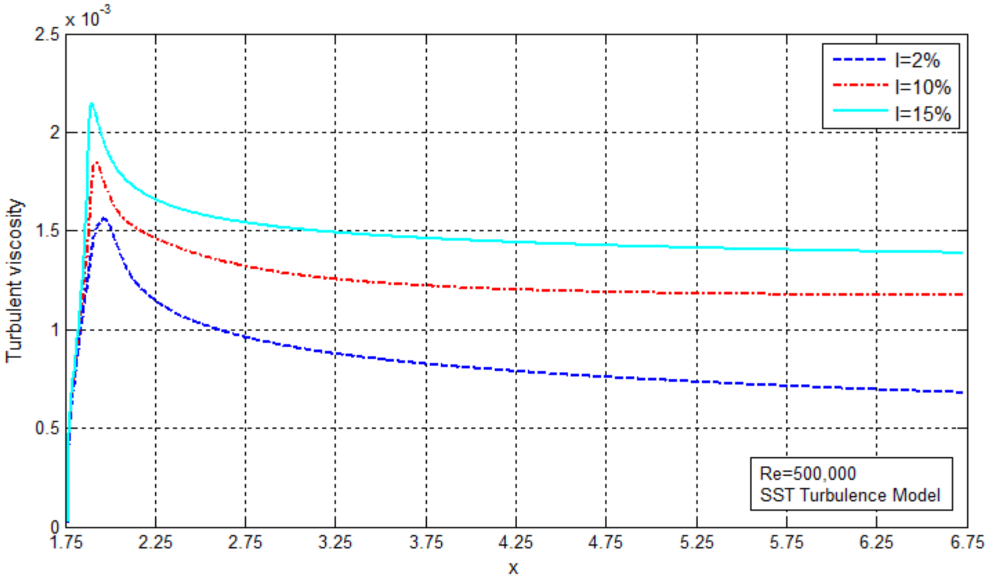

(d)

Fig. 43: Streamwise variation of turbulent flow parameters along the centerline of the turbulent mixing layer core at Re=500,000 for different free-stream turbulence intensities *I* predicted using the SST turbulence model: a) mean velocity magnitude, b) strain rate, c) turbulent kinetic energy, and d) turbulent viscosity

In Figure 43a, streamwise distribution of the mean velocity magnitudes along the centerline of the mixing layers does not illustrate significant variation for the assumed range of turbulence intensities. The velocities start increasing just downstream of the airfoil trailing edge to reach a maximum value, and then display a uniform variation despite the changes of free-stream turbulence intensity. However, smaller mean velocity magnitudes for the lowest intensity (2%) are slightly more apparent upstream of the mixing region. This observation can be explained by streamwise distribution of the turbulence intensity and turbulent viscosity across the mixing layer centerline in Figure 43d. As indicated in this figure, in the steady-state simulations, turbulent viscosity, μ_t, and streamwise fluctuation, u'_{rms}, decline gradually with streamwise (x) distance approaching approximately a constant value in the middle of the mixing region. Therefore, the u'_{rms} variation becomes negligible compared to the mean velocity magnitudes. As a result, the leading mean velocities become unaffected by streamwise fluctuations. This behavior is estimated to change considerably in the unsteady solutions conducted by DNS or LES. Note that, the same distributions of the flow parameters (not shown here), with differences in magnitudes, were observed at Re=250,000.

Included in Figure 43c is streamwise variation of the turbulent kinetic energy, $k,$ that represents nearly the same trend as turbulent viscosity along the mixing layer core. The main reasons for decrease of k are: 1) energy dissipation of the highly-fluctuating small eddies along the core of the mixing layers. This energy is converted to the internal energy of the turbulent eddies as mixing layers proceed toward the end of the domain; and 2) absence of unsteady turbulent reproduction mechanisms (inflow disturbances). Another observation in the figure is a sharp increase of k right after the trailing edge of the airfoil. This sudden increase, which is mainly due to the roll-up of the mixing layers (highly turbulent region) interacting with wake regions, is evident in the streamwise behavior of the other turbulence parameters shown in Figure 43. It is also shown that with increasing turbulence intensity, higher turbulent kinetic energies emerge.

It is notable that monitoring the intermittency (γ) evolution in the streamwise direction (not shown here) indicates a uniform distribution throughout the entire centerline of the mixing layer core. This illustrates that in the steady solution of the mixing layers, intermittency in the core region is evidently constant and not affected by varying the inflow conditions. This observation can also be demonstrated by the fact that the thin mixing layers (streamlines) along the centerline of the flow (core) behave as an inviscid potential core. Such a behavior will be clearly observed in the LES results of the unsteady 3D turbulent mixing layers.

6.1.1.4. Numerical Solution - Unsteady

Temporal evolution of the unsteady 2D turbulent mixing layer is displayed in Figure 44. The figure shows contours of the mean velocity magnitudes (a), turbulent kinetic energy (b), and turbulent viscosity (c) at different flow times for high-speed side Re=250,000 and I=2% using the SST turbulence model in ANSYS-Fluent. As expected, μ_t in the core region of the mixing layers (excluding the inviscid potential core) increases in the streamwise direction as time proceeds. Moreover, turbulent viscosity becomes larger than molecular viscosity in the outer layers of the mixing layers, depending on the local values of Reynolds number (White, 2006, pp. 398-485). This, in turn, causes the eddy diffusivity to decrease from its maximum in the core to approximately zero at the edge of the mixing layers, in the transverse direction. Such a behavior was similarly reported in the study of Sabin (1965). It should be mentioned that turbulent reproduction mechanisms basically cannot be resolved by the steady-state SST (and generally by RANS-based) turbulence model. Note that, in the figure, the mixing layer has nearly reached a steady state at τ_4=126.81.

τ_1=39.1

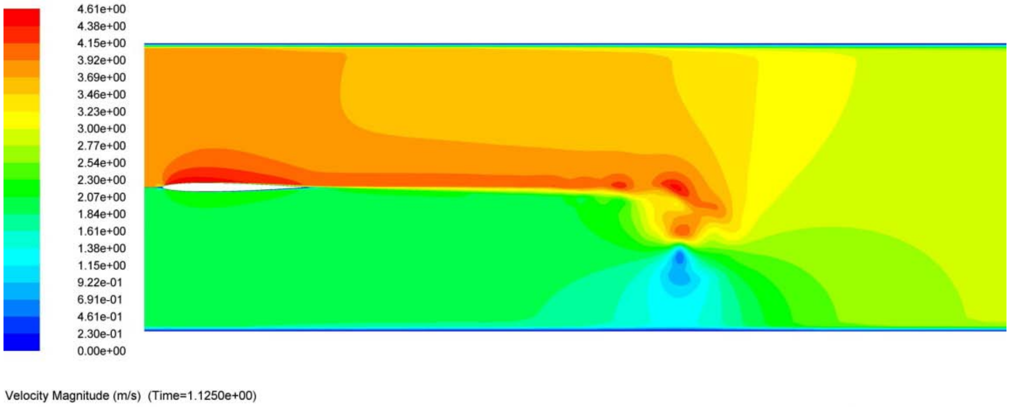

τ_2=75.2

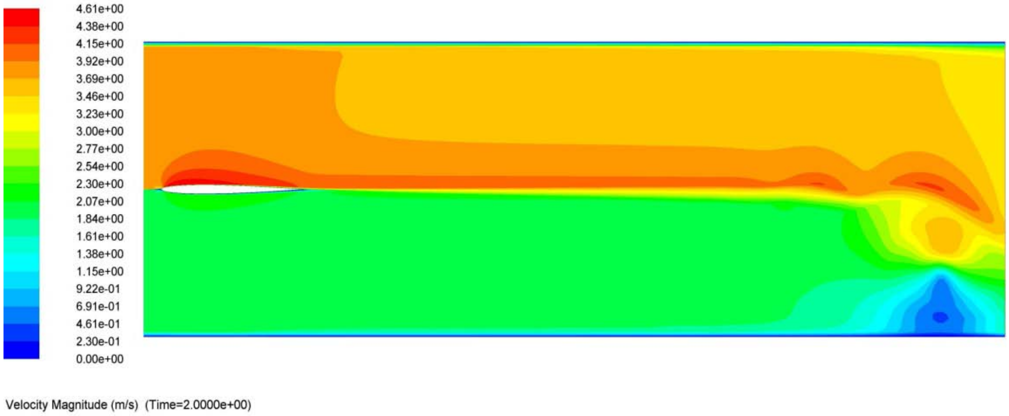

τ_3=101.5

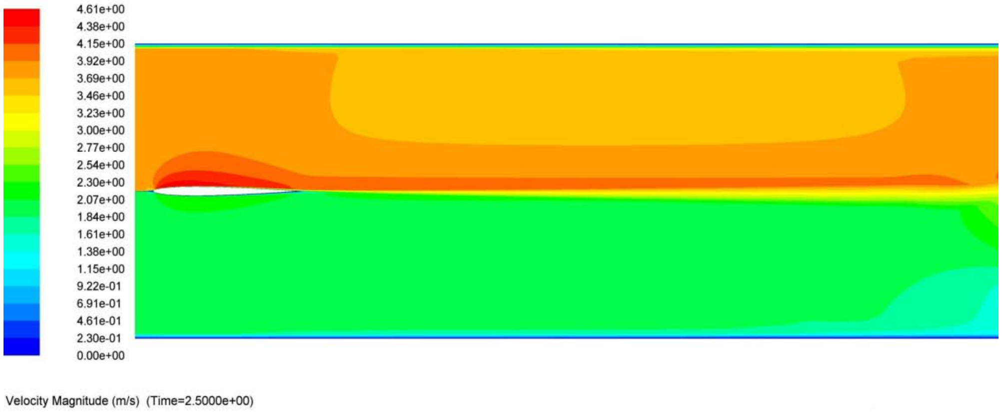

τ_4=126.8

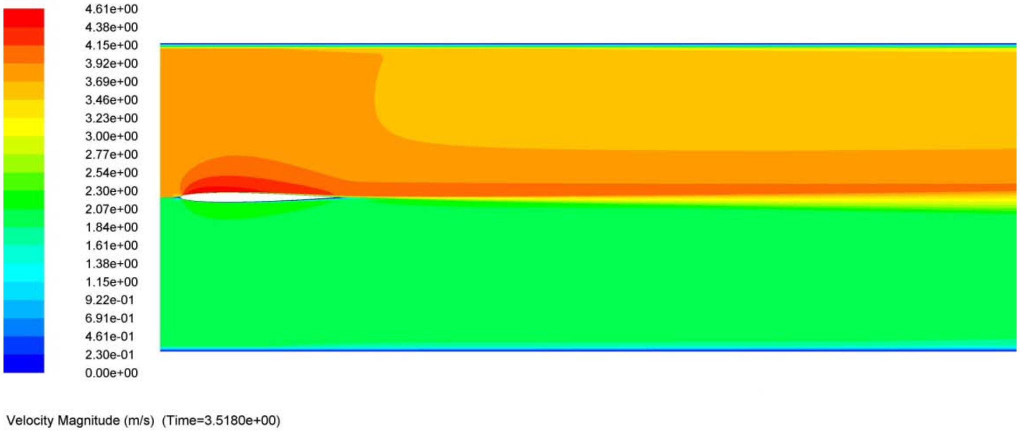

(a)

τ_1=39.1

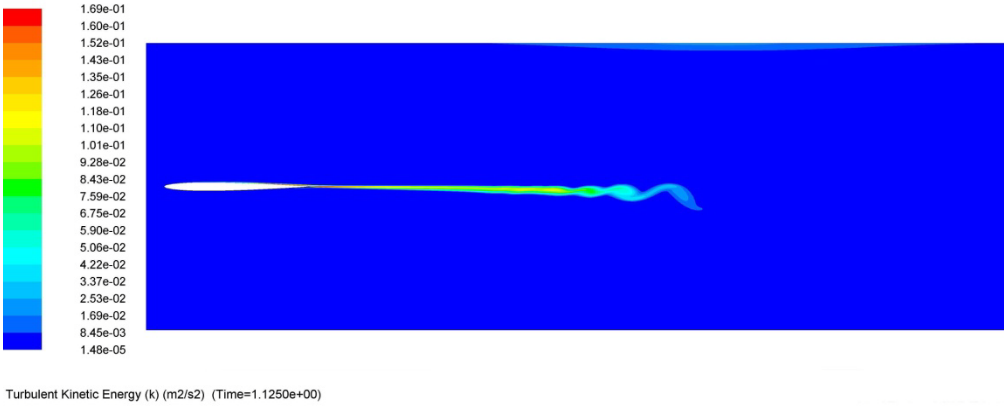

τ_2=75.2

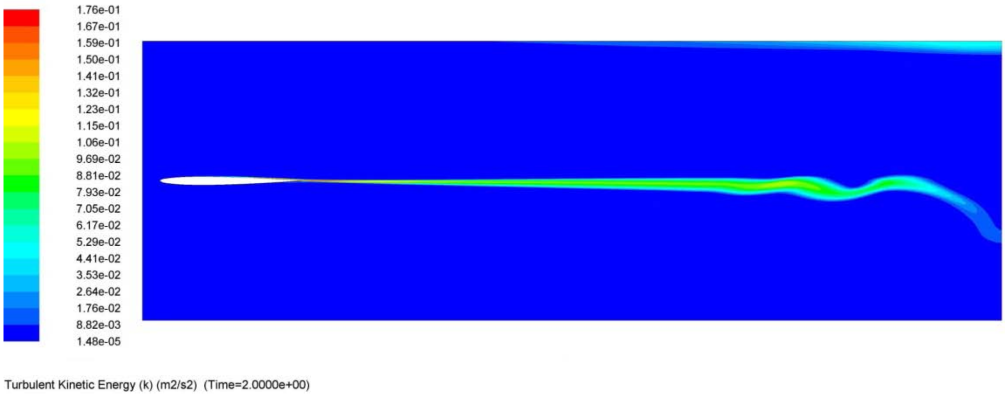

τ_3=101.5

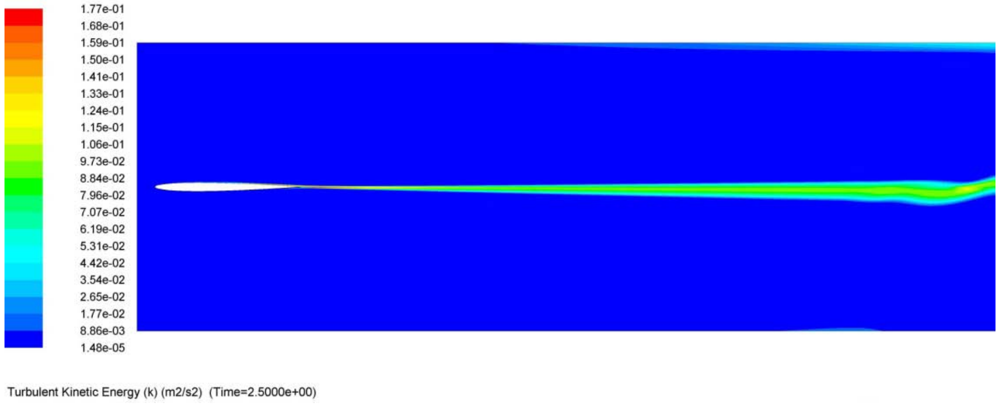

τ_4=126.8

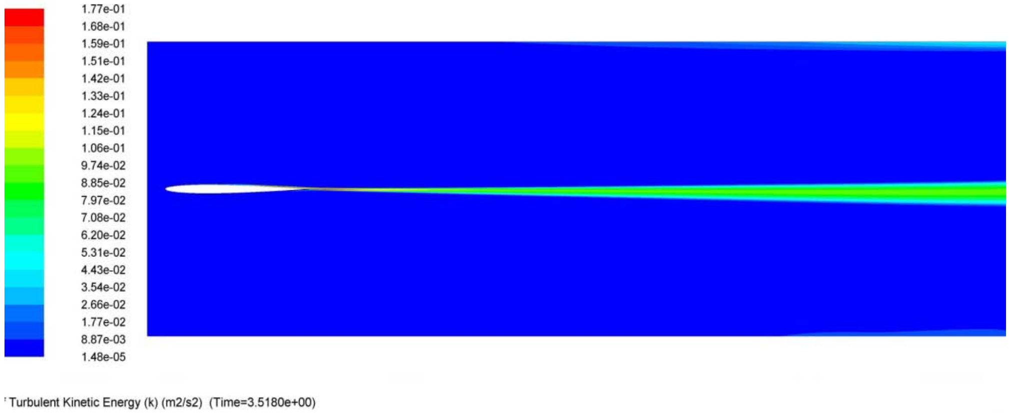

(b)

τ_1=39.1

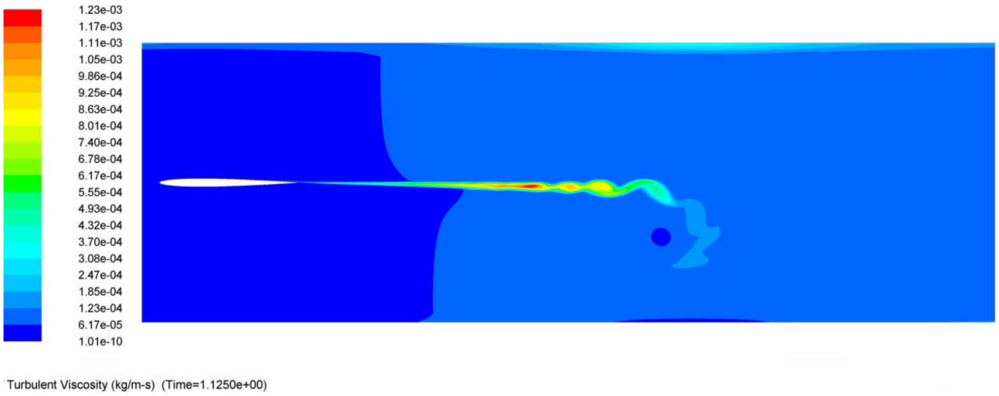

τ_2=75.2

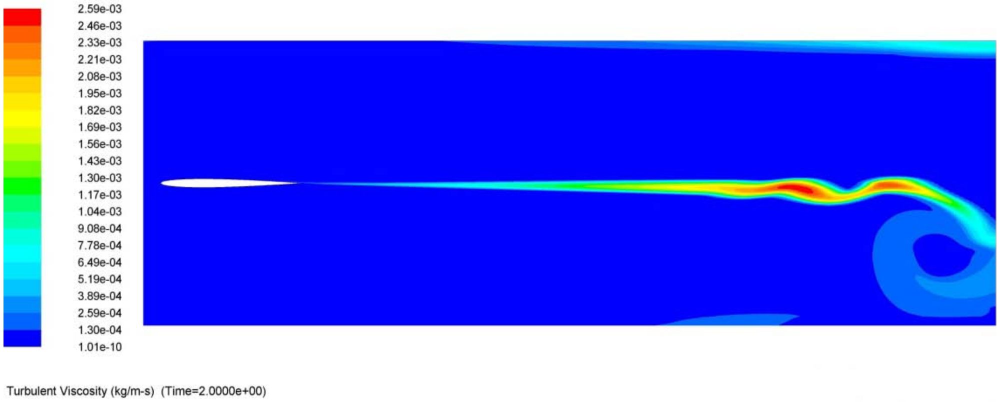

τ_3=101.5

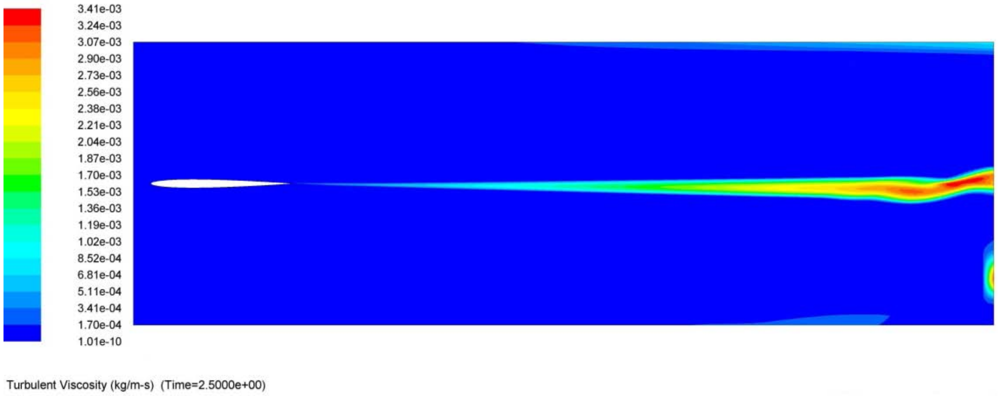

τ_4=126.8

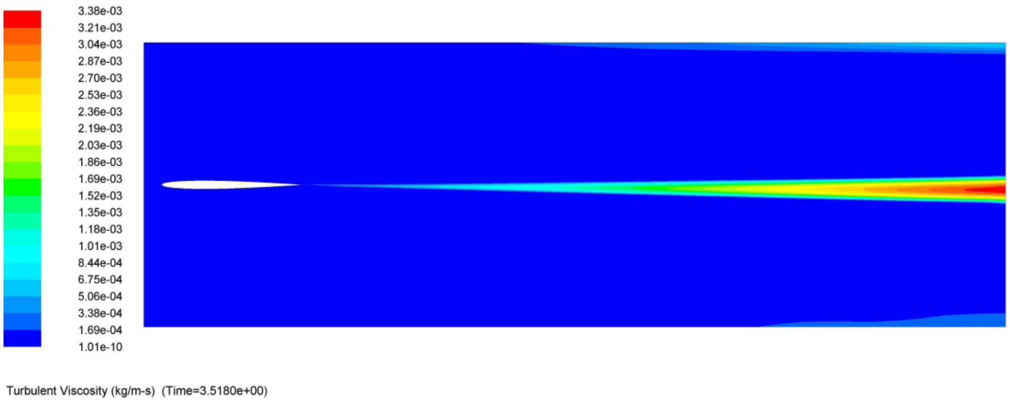

(c)

Fig. 44: Temporal evolution of the 2D turbulent mixing layer for free-stream Re=250,000 with I=2%, at flow times τ_1=39.06, τ_2=75.21, τ_3=101.56, and τ_4=126.81 using the SST turbulence model - contours of: a) mean velocity magnitude, b) turbulent kinetic energy, c) turbulent viscosity

As shown in the front view contours in Figure 44, asymmetric mean flow is revealed due to shedding of eddy structures that alternate from one side to another. This behavior was also reported in the study of Cherdron et al. (1978). At higher free-stream Reynolds numbers or intensities, further disturbances with higher magnitudes are generated at the core of the turbulent mixing layers. In the LES study of the present work, these disturbances are amplified because of the reproduction mechanisms of the turbulence. These disturbances in the current study were characterized by observing the fluctuating behavior of the solution residuals.

6.1.2. Three-Dimensional Mixing Layers

6.1.2.1. Numerical Solution - Unsteady

Based on the accuracy of the results of the 2D simulations, the Launder-Gibson RSTM (LGRSTM) and SST based on $k-\omega$ models were chosen to conduct the unsteady 3D simulations in OpenFoam. These models have almost the same features as $k-\epsilon$, Shear Stress Transport (SST), and Reynolds-Averaged Stress (RAS) models presented in the 2D case. Approximately the same prediction of the turbulent mixing layer behavior was observed by SST based on $k-\omega$ and Launder-Gibson RSTM models. Only results of the SST based on $k-\omega$ model are discussed in this section.

Evolution of the 3D mixing layers subject to high-speed side free-stream Re=500,000 with I=2% at the end of last time step $\tau_{I=2\%}$ =169.49, using the SST model, is shown in Figure 45 from the side (rear - yz plane at x=6.75m) and the top (xz plane at y=0m) views. A moderate percentage of the mixing layer’s three-dimensionality, due to the small velocity fluctuations, is seen in the contours. Although differences from the laminar case are evident, the self-sustaining 3D random motions of the turbulent structures cannot be observed in these results. Additionally, the three-dimensionality effects exist for all of the 3D simulations, even for the 2D mixing layers without any initial cross flow. These effects cause indirect influences of the spanwise fluctuations on the mean flow.

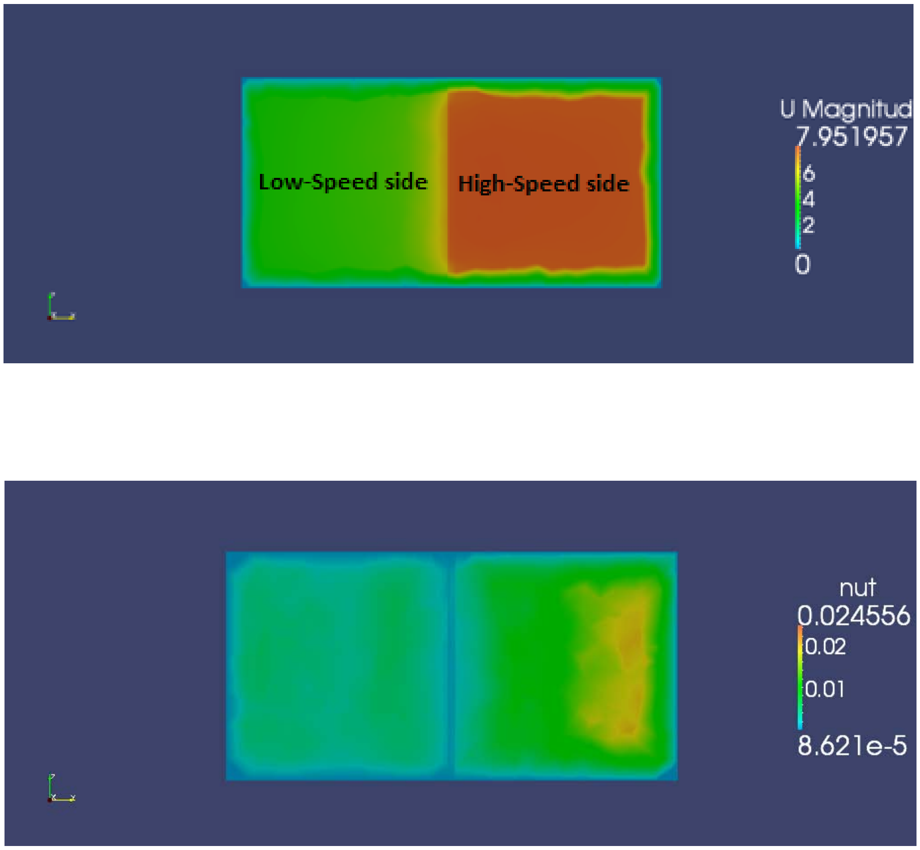

(a)

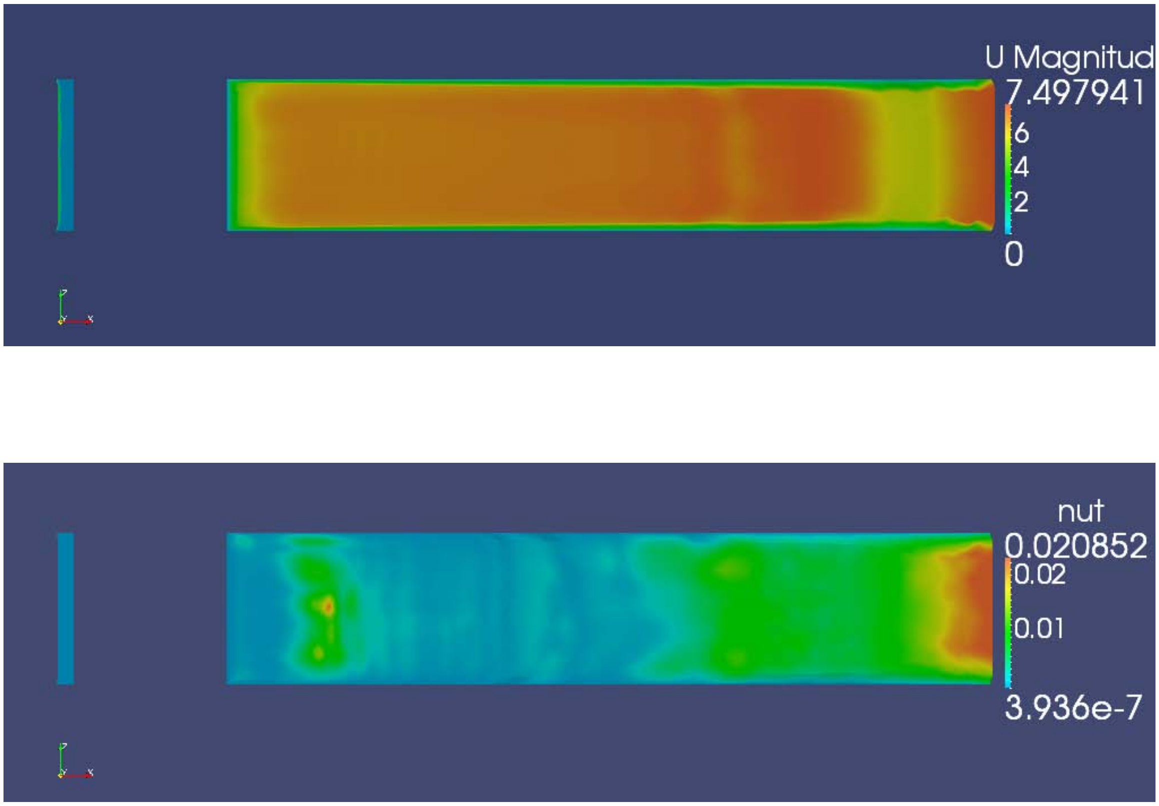

(b)

Fig. 45: Evolution of the 3D low-intensity (I=2%) turbulent mixing layers for Re=500,000 at the end of the last time step $\tau_{I=2\%}$ =169.49 using the SST model: a) side (rear) view contours (yz plane) of $\bar{u}$ and μ_t at x=6.75m, b) top view contours (xz plane) of $\bar{u}$ and μ_t at y=0m

From the top-view evolution, shown in Figure 45b, it is concluded that in the turbulent case, the initiated laminar mixing layers at the airfoil trailing edge break down as time proceeds. Further, the primary infinitesimal disturbances (2D T-S waves) start growing. Consequently, vortical structures expand through the whole domain. In other words, three-dimensionality appears by spanwise growth of the unstable T-S waves. It is notable that the strength of the three-dimensionality increases more quickly for the two-stream mixing layers than that in the single-stream flows. This might be attributed to higher shear strains in the former case. Soon after the transition stage of the developing mixing layers, the flow becomes intermittent with laminar-turbulent regions. Fully-developed mixing layers are finally reached further downstream (White, 2006, pp. 337-394). The visualization of the fully turbulent mixing layers will be discussed in detail through LES results.

6.1.2.2. Effects of Free-Stream Turbulence Intensity

Streamwise velocity profiles at different free-stream intensities using the SST turbulence model are depicted in Figure 46. The profiles show dimensionless variation of streamwise mean velocity magnitudes for Re=500,000 at the last station of domain x=6.75m within -0.5<y<0.5m of planes z=0m, z=-0.2m, z=-0.4m. The data are shown for the final computation times $\tau_{I=2\%}$ =169.49, $\tau_{I=10\%}$ =170.94, and $\tau_{I=15\%}$ =171.92.

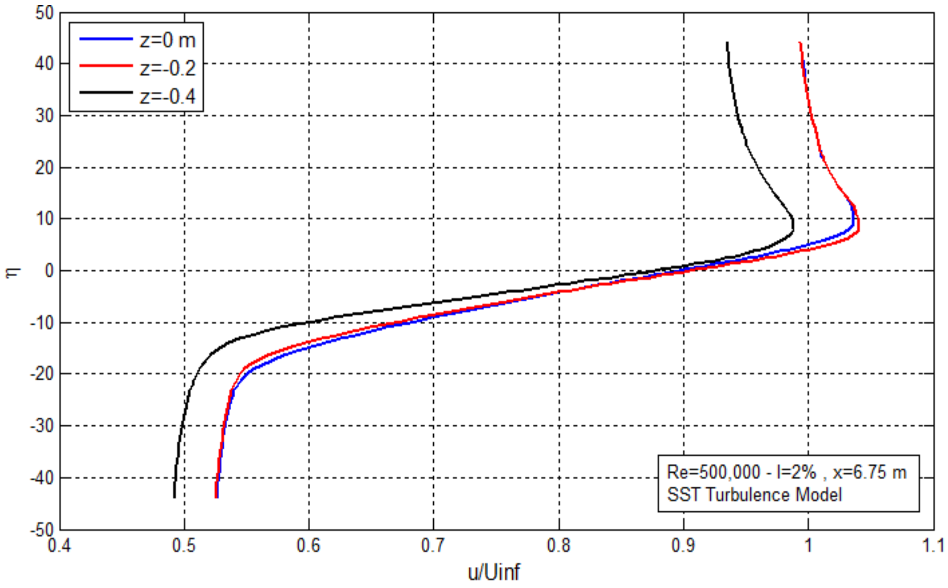

(a)

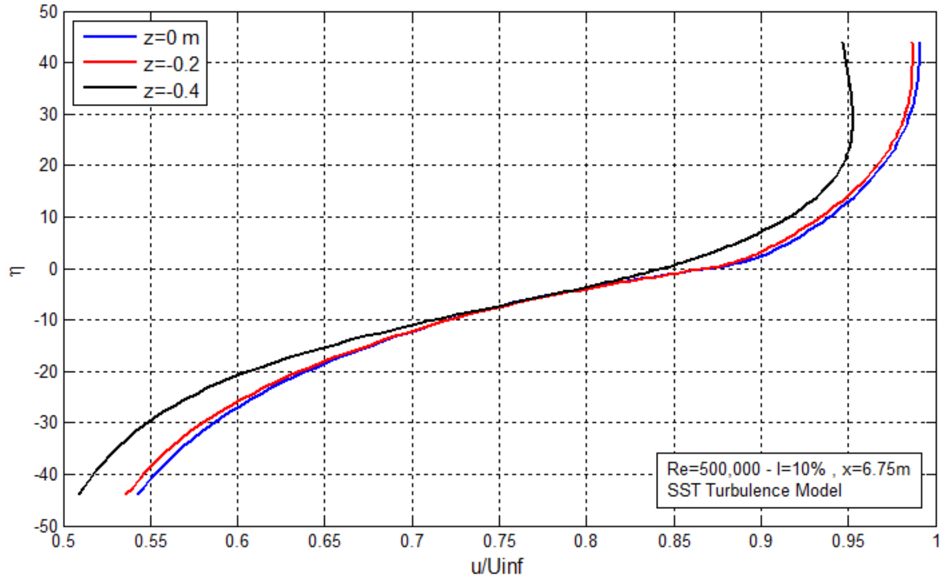

(b)

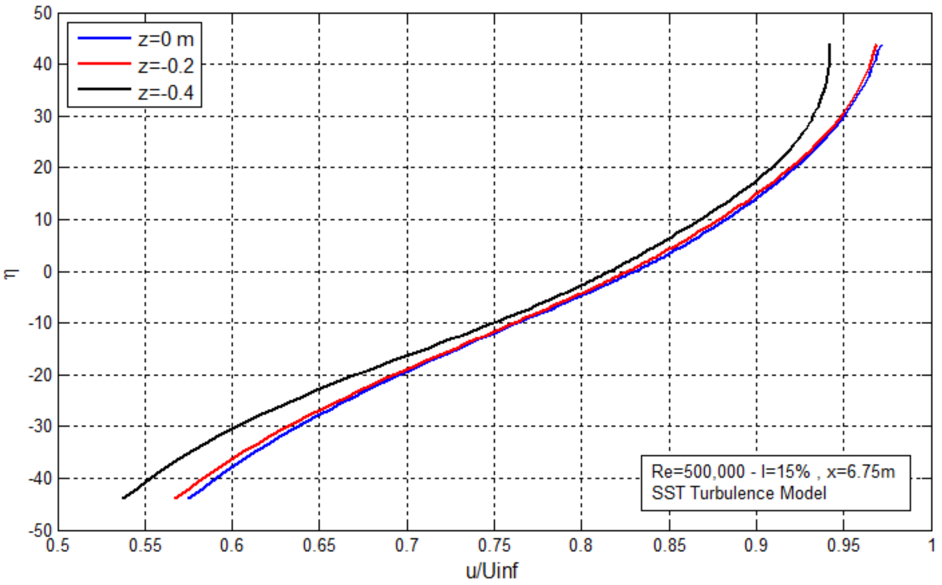

(c)

Fig. 46: Variation of dimensionless streamwise mean velocity profiles in the spanwise direction for the 3D turbulent mixing layer at Re=500,000 (at x=6.75m and z=0m, -0.2m, -0.4m); at the last computation times $\tau_{I=2\%}$ =169.49, $\tau_{I=10\%}$ =170.94, $\tau_{I=15\%}$ =171.92, using the SST turbulence model: a) I=2%, b) I=10%, c) I=15%

A gradient of the mean velocities in the spanwise direction is present due to the three-dimensionality effects produced by mixing layer evolution in the spanwise z direction. Another important observation in Figure 46 is the presence of the overshoots in the high-speed side velocity profiles at I=2%. These overshoots are eliminated at higher intensities, causing smoother profiles to appear. On the other hand, the momentum excess indicated by overshoots leads mean streamwise velocity $\bar{u}$ to be drifted toward the low-speed side of the mixing layers. In Figure 46, it is also shown that due to growing boundary layers on the channel walls, $\bar{u}$ in the near-wall regions (z=-0.4m) decreases with spanwise distance. From the turbulence view point, this kind of behavior is due to the merging of fluid flow vorticity fields generated by the secondary structures in the turbulent mixing layers. The small spanwise variation of the gradients of mean velocity $\frac{d\bar{u}}{dz}$, and also $\frac{d\bar{w}}{dz}$, that skew the vorticity fields, ensure presence of the secondary flows across the mixing region. This procedure is regarded as one of the additional turbulent kinetic energy production mechanisms in high-intensity turbulent mixing layers. It is notable that these variations lose their significance in the near-wall regions (viscous sublayer) where streamwise gradients are dominant over spanwise ones (Hollingsworth and Bourgogne, 1995).

Figure 47 shows streamwise variation of strain rate and turbulent kinetic energy at Re=500,000 and *I*=15% along the centerlines of the three equally-spaced planes z=0m, z=-0.2m, z=-0.4m using the SST turbulence model. The decreasing trend of the strain rates with streamwise (x) distance was investigated in previous sections. As shown in Figure 47a, strain rates do not reveal any significant changes in the spanwise direction, even when observed in downstream regions. Accordingly, this implies that vorticity magnitudes in the spanwise direction do not vary significantly and can be considered to be negligible. Note that, changing the free-stream turbulence intensity does not affect this trend. However, due to formation of the thick boundary layers on the walls, in the case of the free-stream turbulence intensity *I*=2%, small changes of vorticity magnitudes are expected.

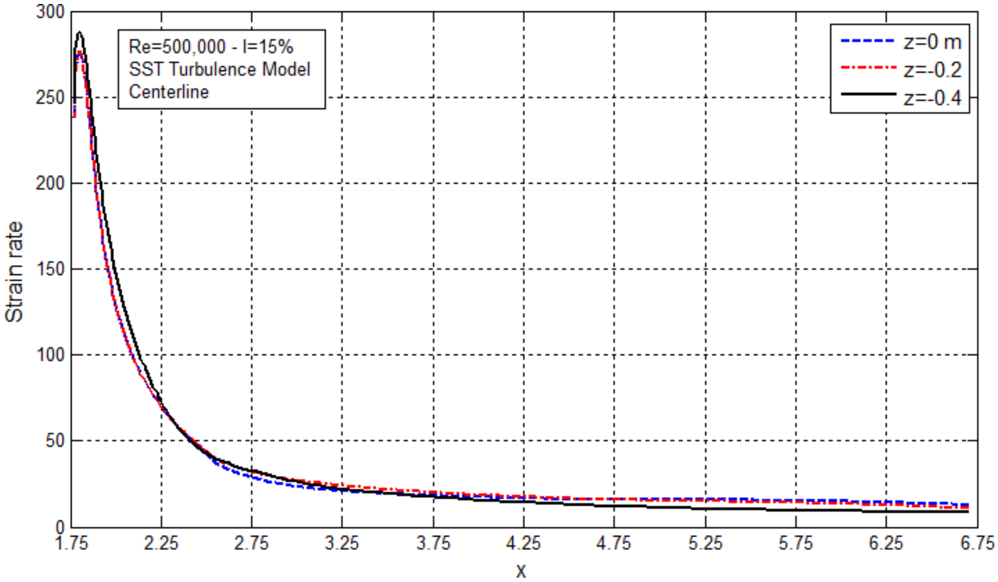

(a)

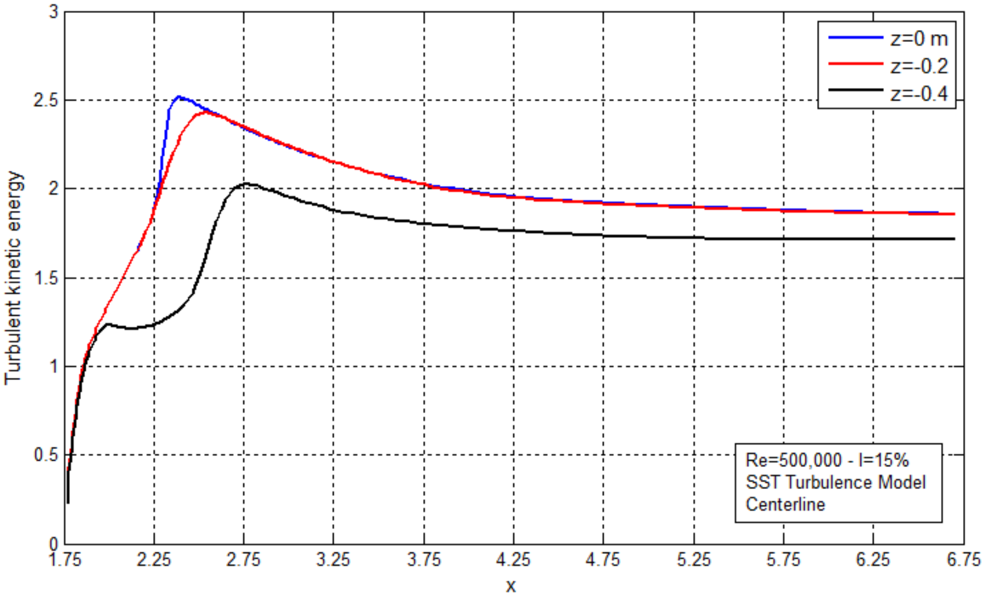

(b)

Fig. 47: Streamwise variation of strain rate for the 3D turbulent mixing layer at Re=500,000 and I=15% along the centerlines of three equally-spaced planes z=0m, z=-0.2m, z=-0.4m; at the end of the last time step $\tau_{I=15\%}$ =171.92 using the SST turbulence model

Using the same method of 3D analysis, streamwise mean velocity magnitudes along the centerlines of the three spanwise planes (not shown here) shows an opposite and increasing trend compared to the strain rate variations. Similarly, no significant difference was observed. Thus, the results obtained suggest that spanwise variation of the strain rates and mean velocity magnitudes along the centerlines of these planes are independent of free-stream turbulent intensities.

Included in Figure 47b is a variation of the turbulent kinetic energy in the spanwise direction along the same lines used before. Streamwise variation of the turbulent kinetic energy for a range of free-stream intensities was studied in the 2D case. In the spanwise direction, as depicted in the figure, k follows the same distributions along the centerlines of z=0m and z=-0.2m planes. As streamlines become closer to the channel walls, a sudden reduction of the turbulent kinetic energy magnitudes appears. Step-like behavior of the k distribution along the centerline of plane z=-0.4m, upstream of the mixing layers close to the trailing edge of the airfoil, is estimated to be due to the presence of low-momentum corner flow at the intersection of the airfoil and side walls. This corner flow interacts with the generated cross flow and streamwise wake regions, just behind the airfoil trailing edge.

Spanwise variations of the mean velocity profiles, turbulent kinetic energy, and strain rates at free-stream Re=500,000 with I=2%, I=10%, I=15% at the last station x=6.75m are shown in Figure 48. Results are given for final computation times $\tau_{I=2\%}$ =169.49, $\tau_{I=10\%}$ =170.94, and $\tau_{I=15\%}$ =171.92 using the SST turbulence model. The findings indicate relatively similar distributions as for the laminar case at Re=10,000. Generally, behavior of the turbulent mixing layers at low intensity, I=2%, is approximately the same as for the laminar flow. As a result, and because of the growing boundary layers on the walls, distribution of the mean velocity magnitudes is nearly uniform, as depicted in the Figure 48a. However, due to the presence of the three-dimensionality effects, and highly fluctuating eddies in the near-wall regions, the corresponding profile at I=2% shows reduced momentum in core mixing regions (z=0m) compared to those close to the channel walls. Another reason for this kind of distribution is the tendency of the streamlines around the airfoil to be drifted toward the “separating lines” formed on the airfoil upper and lower surfaces (White, 2006, pp. 308-319).

In contrast to the mean velocity magnitudes, the adverse behavior of the turbulent kinetic energy (and turbulent viscosity, not shown here) is observed in Figure 48b. The figure illustrates that with increasing free-stream turbulence intensity, turbulent kinetic energy k goes up. This observation can be explained mathematically through Equation (31), representing a direct relation between free-stream turbulence intensity and kinetic energy. It is also deduced that for the lowest turbulence intensity, high-frequency eddies in the near-wall regions carry more turbulent kinetic energy than those in the core regions of the mixing layers. This distribution is reversed with rising turbulence intensity such that viscous forces (near the channel walls) are dominated by convective accelerating forces in the central regions.

With increasing turbulence intensity, low-momentum flow in the near-wall regions and high-momentum flow in the outer regions are generated. As a result, fully-developed mean velocity profiles with steeper slopes, as compared to the laminar case, are observed. It is also evident that due to approximately uniform distributions of the turbulence intensities in the spanwise direction at the observed flow times, all present profiles are symmetric.

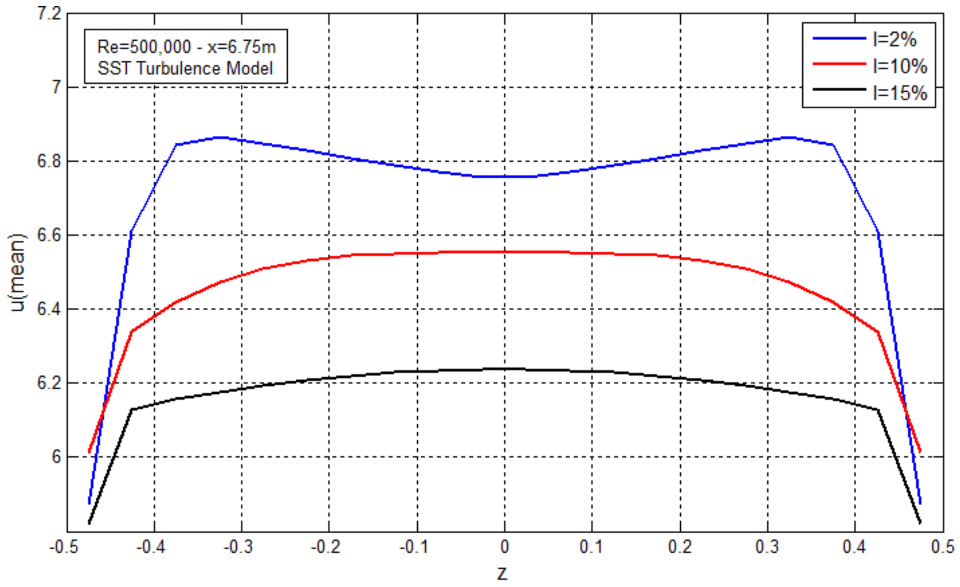

(a)

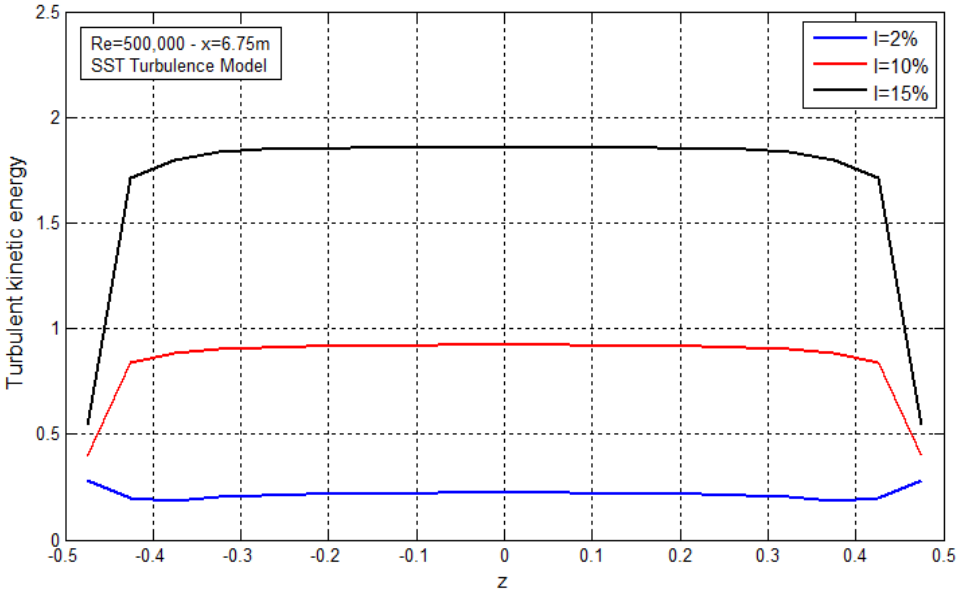

(b)

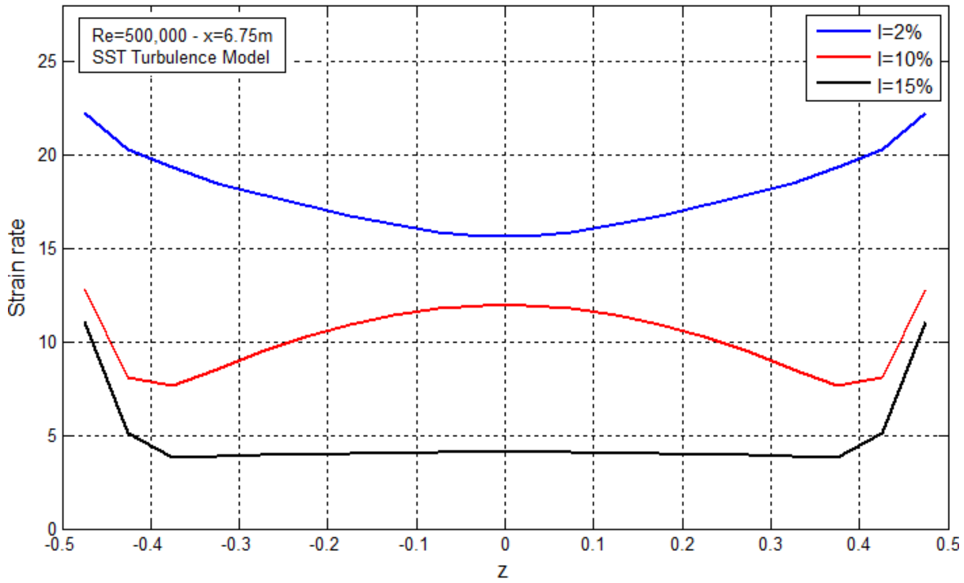

(c)

Fig. 48: Spanwise variations of a) mean velocity magnitude, b) turbulent kinetic energy, and c) strain rate, in the streamwise direction for the 3D turbulent mixing layer at high-speed side free-stream Re=500,000 with I=2%, I=10%, I=15% at x=6.75m and y=0m; and at the last computation times $\tau_{I=2\%}$ =169.49, $\tau_{I=10\%}$ =170.94, and $\tau_{I=15\%}$ =171.92 using the SST turbulence model

Spanwise variations of the strain rates at x=6.75m are depicted in Figure 48c. They show an approximately developed distribution for the lowest turbulence intensity. This behavior is mainly due to the presence of the high shear strain gradients ($\frac{\partial \bar{u}}{\partial y}$) in the near-wall regions further upstream of the mixing layer; and also due to the formation of the wakes behind of the airfoil trailing edge. As a result, strain rate changes are reduced in the regions far enough from the walls. With rising turbulence intensity up to I=10%, a double-peak distribution of the strain rates, with lower magnitudes compared to the lowest intensity profile, emerges. This observation can be explained by the fact that the turbulent mixing layer is approaching a fully-developed state. Moreover, interactions of the developing high-momentum mixing layers with growing boundary layers on the walls, and also with low-momentum corner flow in the junction of the airfoil and side walls, are expected to cause this behavior. The double-peak behavior at I=10% is slowly eliminated when reaching I=15% in a way that a fully-developed distribution of the strain rates with a roughly constant minimum value is present for I=15%. So, according to the above results, it is possible to say that the turbulent mixing layer for the highest free-stream turbulence intensity behaves as a fully-developed turbulent flow. Note that, decreasing the free-stream Re number leads to a reduction of strain rates, mean velocity magnitudes, and other turbulent flow parameters.

6.1.2.3. Variation of Reynolds Stresses

In order to investigate behavior of the Reynolds stresses, 3D simulations were conducted by employing the Launder-Gibson RSTM (LGRSTM) model. To reduce the computation time, RANS-based simulations were started by using the $k-\epsilon$ model (i.e. as an initial solution), and then switching to the RSTM. Distributions of the dimensionless Reynolds stresses ($\sqrt{\overline{u'^2}}, \sqrt{\overline{v'^2}}, \overline{u'v'}$) for free-stream Re=500,000 and the applied range of turbulence intensities, at the end of the last time step, are shown in Figure 49. Note that, non-dimensionalization was done in terms of the dimensionless scale parameters used by Hollingsworth and Bourgogne (1995) and Mehta (1991). Small Reynolds stresses in the near-wall regions are visible in the plots. This observation can be briefly explained by two reasons: 1) the no-slip boundary condition which is defined with regard to fluctuation is basically on a different scale from its usual definition for velocity; and 2) despite the fact that walls are generally resistant and impose damping effects on the flow, their resistances are limited in the case of the turbulent flows. Existence of the fluctuation, and Reynolds stresses, outside the mixing layers can be attributed to the presence of an intermittent superlayer at the interface of the turbulent and non-turbulent regions, that interact with the outer boundary layers (Klebanoff, 1955). It should be added that bounding walls around the turbulent shear layers cause anisotropy within the flow field. As a result, even though all three present Reynolds stresses follow approximately the same trends, due to small differences in their rms values, low percentages of turbulence inhomogeneity are expected. Note that, the Reynolds stresses are moderately weakened in the near-wall regions, as displayed in Figure 49 for $\overline{u'^2}$, and strengthened with increasing free-stream velocity.

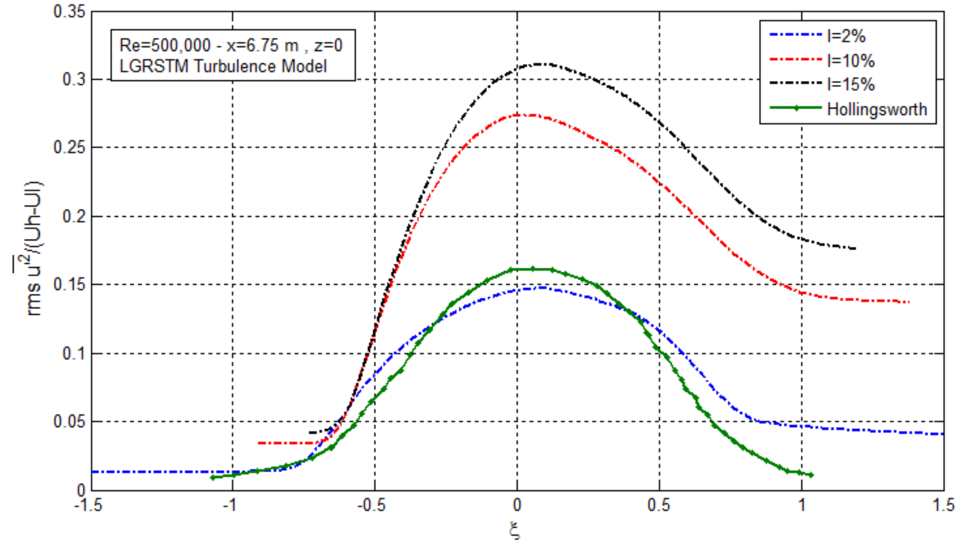
Re=500,000 - x=6.75 m , z=0
LGRSTM Turbulence Model
I=2%
I=10%
I=15%
Hollingsworth
rms $\overline{u^2}$/(Uh-Ul)
ξ
0.35
0.3
0.25
0.2
0.15
0.1
0.05
0
-1.5
-1
-0.5
0
0.5
1
1.5

(a)

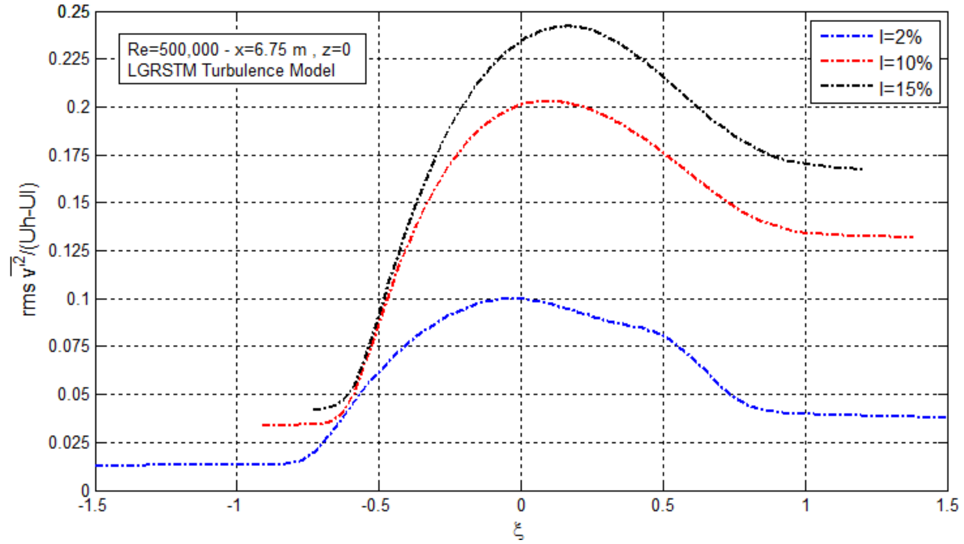
Re=500,000 - x=6.75 m , z=0
LGRSTM Turbulence Model
I=2%
I=10%
I=15%
rms $\overline{v^2}$/(Uh-Ul)
ξ
0.25
0.225
0.2
0.175
0.15
0.125
0.1
0.075
0.05
0.025
0
-1.5
-1
-0.5
0
0.5
1
1.5

(b)

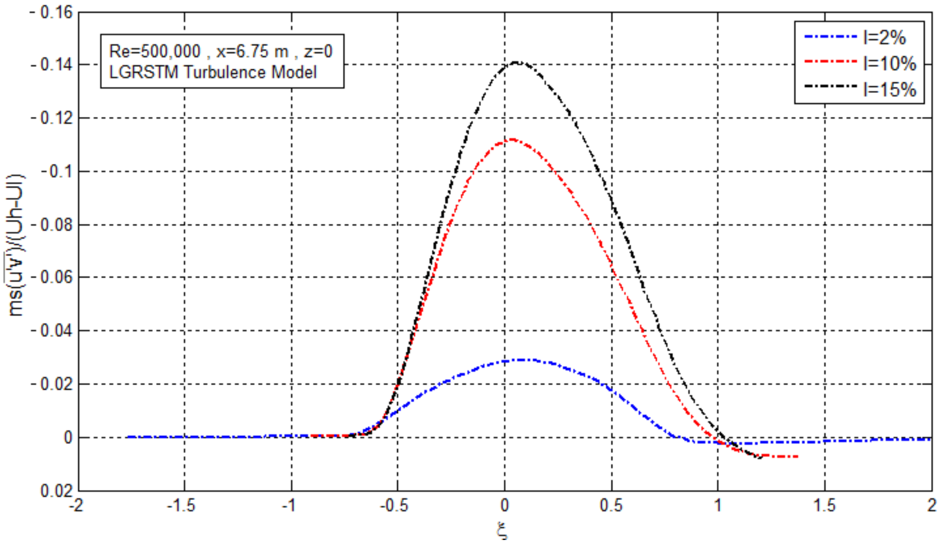

(c)

Fig. 49: Normalized root mean-square Reynolds stress distribution for the 3D turbulent mixing layer at free-stream Re=500,000 with different turbulence intensities *I*=2%, *I*=10%, *I*=15% at x=6.75m and z=0m; at the last computation times $\tau_{I=2\%}$ =169.49, $\tau_{I=10\%}$ =170.94, $\tau_{I=15\%}$ =171.92 using the LGRSTM turbulence model: a) streamwise normal stress ($\sqrt{\overline{u'^2}}$) – experimental data of Hollingsworth and Bourgogne (1995), b) lateral normal stress ($\sqrt{\overline{v'^2}}$), c) primary shear stress ($\overline{u'v'}$)

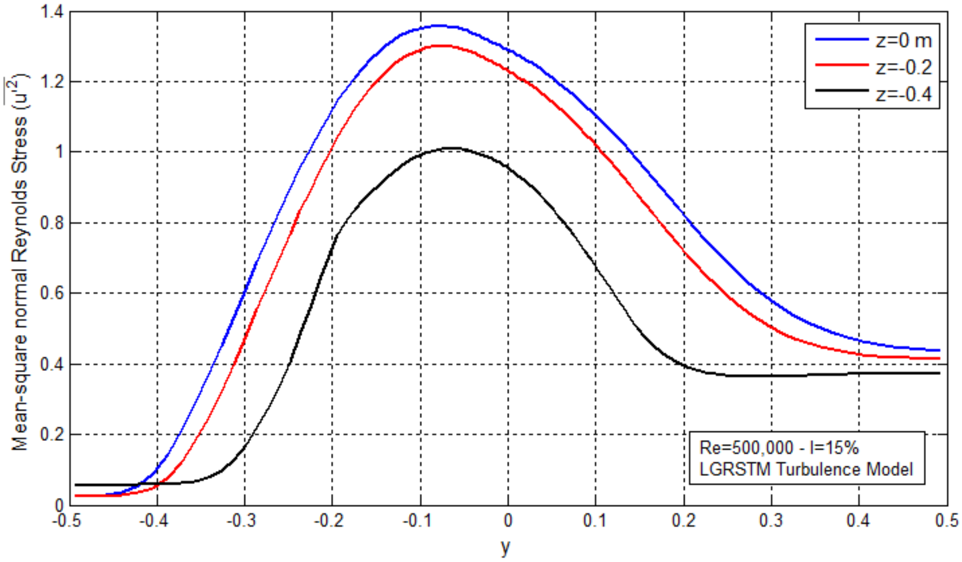

Fig. 50: Spanwise variation of mean-square streamwise normal stress ($\overline{u'^2}$) for the 3D turbulent mixing layer at free-stream Re=500,000 with *I*=15% at the last station of z=0m, z=-0.2m, z=-0.4m planes (x=6.75m); at flow time $\tau_{I=15\%}$ =171.92 using the LGRSTM turbulence model

Generally, in relatively low-intensity flows, shear stresses (strain rates) are more dominant in the mixing region and due to that, streamwise fluctuations are not able to be sustained. This is illustrated in Figure 50. The profiles of $\overline{u'^2}$ for the medium and high turbulence intensities display uniform trends outside the mixing layers. This uniformity might change slightly in the velocity-excess regions (Hollingsworth and Bourgogne, 1995).

Although symmetry is roughly approached in the curves of Figure 49, asymmetric behavior of the Reynolds stresses has an apparent bias toward the low-speed side prior to normalization of the stresses. The velocity ratio and transverse gradient of the mean velocity profiles, used as non-dimensionalization factors, seem to affect the symmetric behavior. This can be demonstrated by the fact that the transverse gradients of the mean velocity magnitudes across the mixing layers are enhanced by the presence of the wake behind the airfoil. Therefore, since transverse gradient is regarded as a turbulence production parameter in the Reynolds-stress governing equations, e.g. $\overline{v'^2}\frac{\partial \bar{u}}{\partial y}$, higher turbulence production and Reynolds stresses are generated in the core of the mixing layers. Moreover, the effect of the velocity defect in downstream regions, superimposed by mixing layers evolution, improves this behavior (Mehta, 1991). It is notable that because of the transverse fluctuations, small variation of the pressure gradients within the mixing layers is expected. This conclusion was not observed in the laminar case. A small secondary peak of the primary normal stresses is seen on the low-speed side of the mixing layers. This is largely due to the velocity defect produced by upstream wakes, and the three-dimensionality effects. The presence of such a secondary peak was reported similarly in the experimental study of Mehta (1991).

Another specific observation in Figure 49 is negativity of the primary shear stresses, $\overline{u'v'}$, inside the mixing layers. The negativity of $\overline{u'v'}$ stresses can be explained by positivity of the eddy viscosity which imposes the primary shear stress to be negative (positivity of the total shear stress). Additionally, by assuming positive shear strain, $\frac{\partial \bar{u}}{\partial y} > 0$, eddies with downward motions ($v'_{rms} < 0$) increase streamwise velocity ($u'_{rms} > 0$) causing a negative product. In the same manner, a decrease in u'_{rms} is observed for those eddies with upward motions in the flow field (White, 2006, pp. 398-485).

It is worth noting that negative Reynolds shear stress ($\overline{u'v'} < 0$) physically means transfer of the momentum in the gradient diffusion direction whereas positive $\overline{u'v'}$ represent a counter-gradient diffusion. Thus, the negative Reynolds shear stresses in mixing layers are estimated to be result of: 1) the faster velocity field in the upper side of the mixing layers, causing upper streams to be decelerated toward the lower side; and 2) the momentum transfer within large-scale eddies in their usual gradient direction. This behavior cannot be generalized in the case of the unstable small-scale eddies that are frequently seen in developing mixing layers (Ito et al., 2013).

The results shown in Figure 49 agree with the experimental data of Hollingsworth and Bourgogne (1995) who investigated self-similarity in mixing layers behind a splitter plate. Differences between the profiles are predicted to be attributed to the presence of the airfoil as splitter and a mild pressure gradient formed due to that. Validation of the results also suggests that self-similarity is attained for the smallest turbulence intensity profiles. Presence of higher Reynolds stresses in the figure indicates that the self-preservation in the medium and high intensity environments occur at a longer time. This is estimated to be because of more entrainment of the turbulent spots for higher turbulence intensities.

Due to approximate equality of the root mean-square values of the streamwise and transverse Reynolds stresses (fluctuations) throughout the whole domain (far enough from the airfoil), a high percentage of turbulence isotropy is expected with respect to x, y coordinates. However, it is estimated that because of the three-dimensionality effects, this observation does not apply for Reynolds stresses in the spanwise z direction. It is pointed out that, generally turbulence quantities including fluctuations (i.e. Reynolds stresses) need more time to develop and show self-preservation in comparison with the mean quantities. As a result, turbulence isotropy within the flow field is delayed (White, 2006, pp. 398-485).

6.1.2.4. Mixing Layer Growth

Streamwise variation of the mixing layer growth parameters was studied in the 2D case. In order to explore spanwise changes of the mixing layer displacement and momentum thicknesses in the 3D case, the same procedure was implemented as in the 2D case.

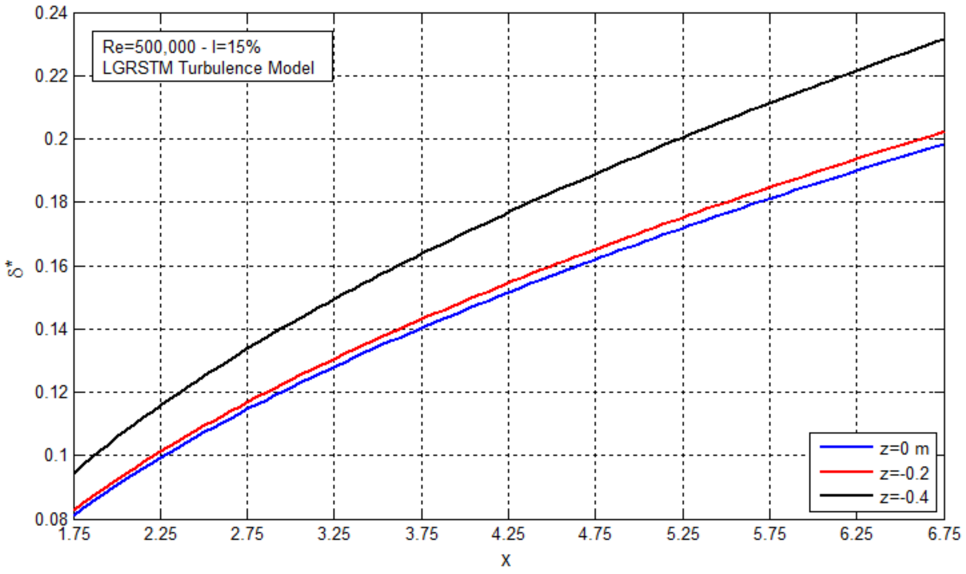

(a)

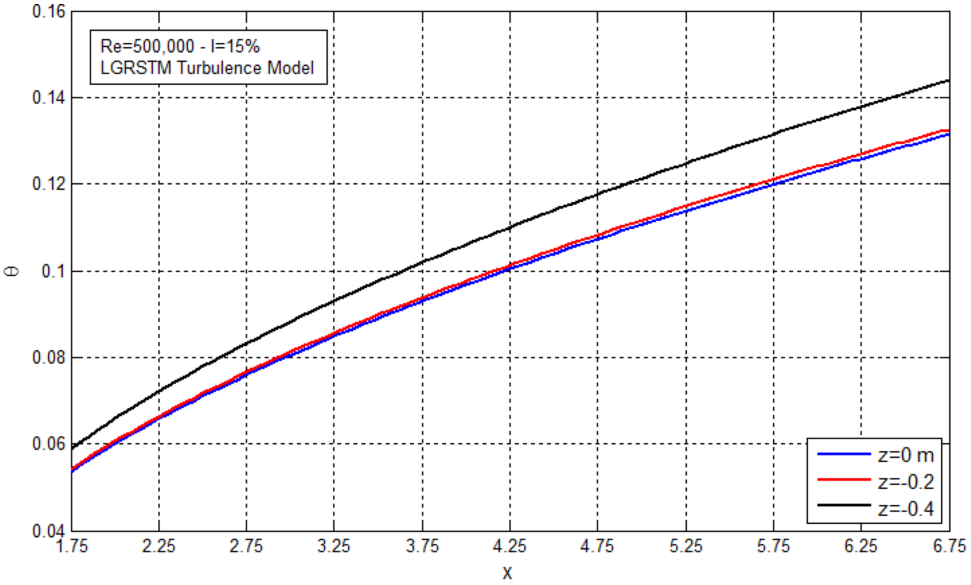

(b)

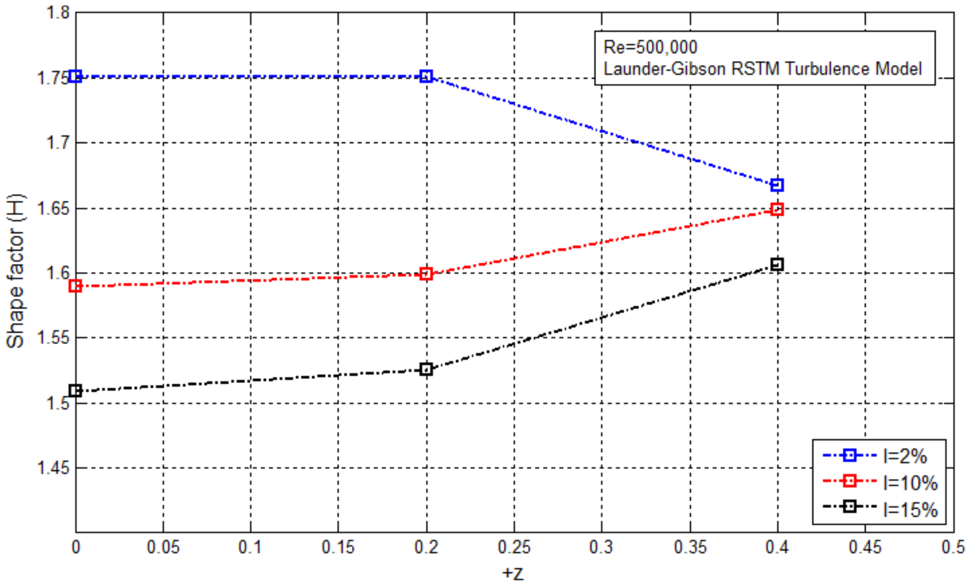

(c)

Fig. 51: Spanwise variation of: a) displacement thickness (I=15 %), b) momentum thickness (I=15%), and c) shape factor for the 3D turbulent mixing layer at high-speed side free-stream Re=500,000 and different free-stream intensities along the centerlines of planes z=0m, z=-0.2m, z=-0.4m; at time scales $\tau_{I=2\%}$ =169.49, $\tau_{I=10\%}$ =170.94, and $\tau_{I=15\%}$ =171.92 using the LGRSTM turbulence model

Variations of the mixing layer streamwise growth rate parameters at high-speed side free-stream Re=500,000 and I=15% and shape factors in the applied range of free-stream intensities are given in Figure 51. The plots show the variations in the spanwise direction along the centerlines of three uniformly-spaced planes z=0m, z=-0.2m, z=-0.4m. The LGRSTM model in OpenFoam was used to examine these variations. Results are taken at the last time steps $\tau_{I=2\%}$ =169.49, $\tau_{I=10\%}$ =170.94, and $\tau_{I=15\%}$ =171.92. As depicted, for the medium and high turbulence intensities, shape factor increases gradually whereas in the lowest turbulence intensity (I=2%), an opposite trend is observed. This behavior, that occurs mainly due to formation of a relatively thick boundary layer in the near-wall regions, was similarly illustrated in the 3D laminar case for Re=100,000 and 150,000. Note that, the same trends for growth rate parameters were observed at other free-stream Re and turbulence intensities. Also, the shape factors found by the applied turbulence models (not presented here) collapse relatively well onto each other.

6.2. Large Eddy Simulation (LES)

In the LES modeling, the full unsteady Navier-Stokes partial differential equations are solved by filtering the turbulent eddies in the flow. Existing eddies larger than the grid size (turbulence length scale) are resolved directly, whereas smaller eddies with sub-grid scales (SGS) are modeled.

Unsteady fully turbulent three-dimensional mixing layers of the present study were simulated by using the LES filtering method in OpenFoam. In this method, the Navier-Stokes equations are filtered such that large fluctuation (eddies) are resolved implicitly through direct numerical simulation (DNS) while small eddies are modeled by employing the RANS-based models. The LES simulations were conducted at high-speed side free-stream Re=500,000, and the oneEqEddy (k-equation eddy viscosity model) model was used to resolve the corresponding μ_{t-SGS} transport equation. Note that, in the oneEqEddy SGS model, a balance equation is derived to investigate the transport of the turbulent kinetic energy (OpenFoam, 2011-2015). The same grid was used as for the previous cases.

In order to ensure that the inflow conditions of the LES simulations generate a fully-turbulent flow, results of the LGRSTM model on the plane at x=6.75m were mapped and used as initial conditions for the LES. These conditions contain small perturbations (fluctuations) in the streamwise, transverse, and crosswise directions. Thus, initial vortex pairs are triggered to produce fully-turbulent inflow.

Spatial and temporal evolutions of the unsteady self-sustaining vortical structures are shown in 3D view contours of the subgrid-scale turbulent viscosity (μ_{t-SGS}) in Figures 52 and 53. These figures depict side (rear) and top views of time-varying μ_{t-SGS} contours at four streamwise stations: x=1.75m, 3.5m, 5.5m, 6.75m, for free-stream Re=500,000 with I=2%. A high percentage of three-dimensionality is seen in the contours. Fluctuating eddies of different sizes, with dissimilar energy levels, are seen to evolve through the domain. Moreover, since the turbulent mixing layer in this case is fully-turbulent, self-preservation is estimated to be attained in the far downstream regions as explained by theory: equilibrium exists between the turbulence production and decay (White, 2006, pp. 398-485).

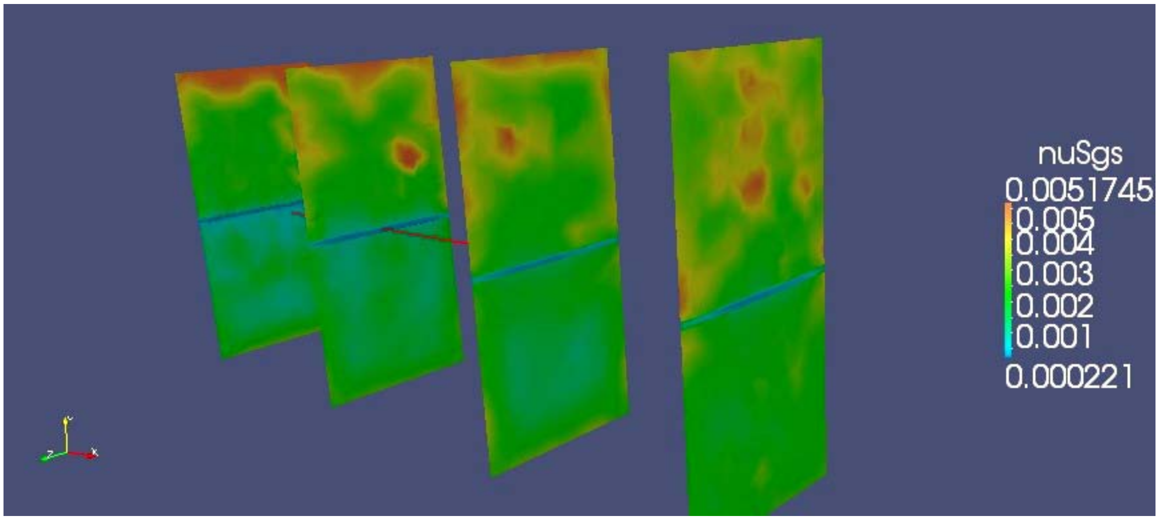

Fig. 52: Spatial evolution of the 3D turbulent mixing layers at free-stream Re=500,000 with I=2%, at the last simulation time τ_4= 427.21 using the LES: 3D view contours of μ_{t-SGS} at x=1.75, 3.5, 5.5, 6.75m (yz plane)

τ_1=105.9

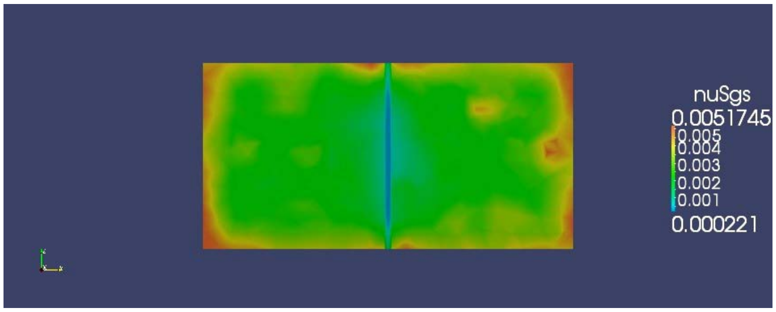

τ_2=205.6

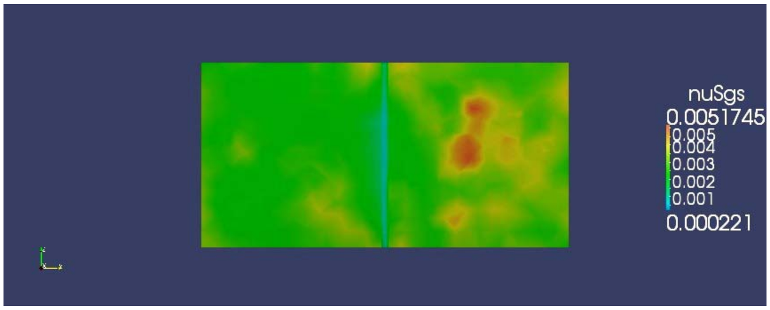

τ_3=311.7

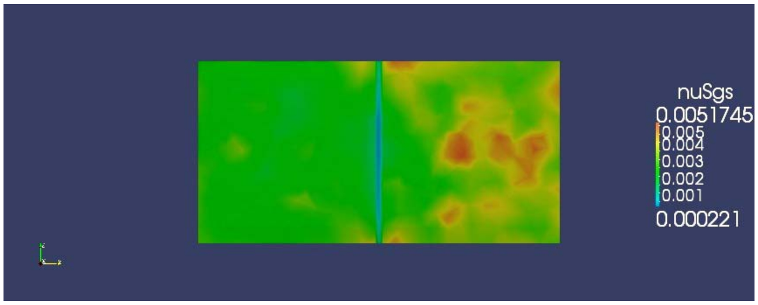

τ_4=427.2

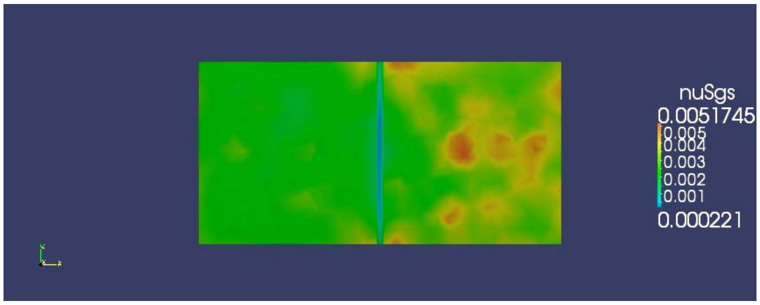

(a)

τ_1=105.9

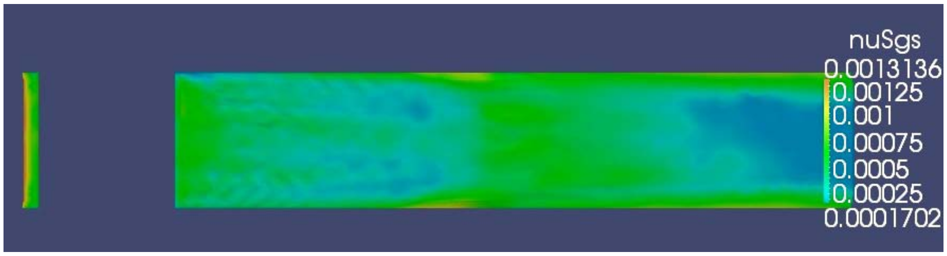

τ_2=205.6

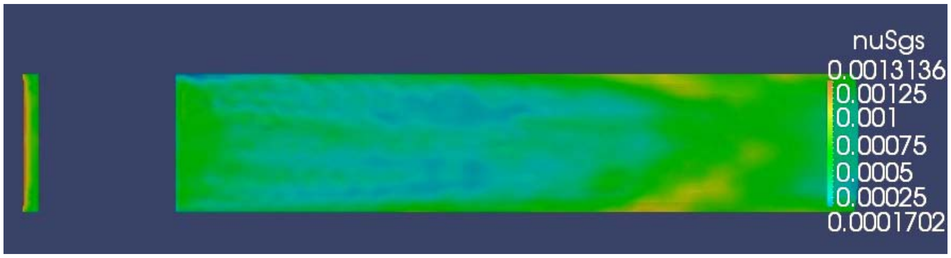

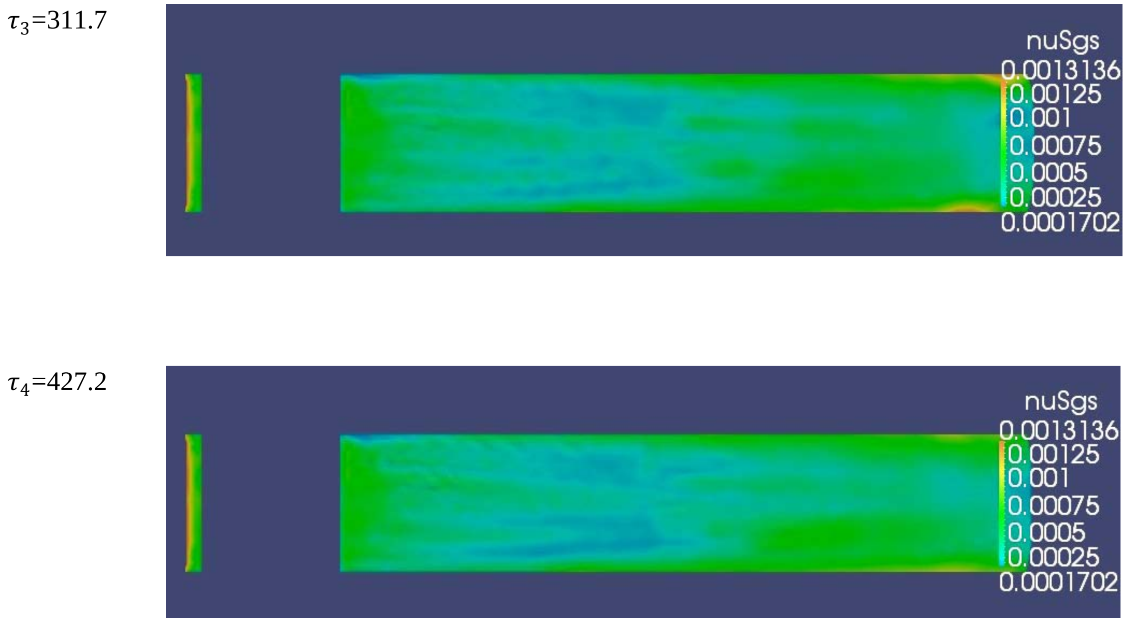

(b)

Fig. 53: Temporal evolution of the 3D turbulent mixing layers in the streamwise direction at high-speed side free-stream Re=500,000 with I=2%, at dimensionless time scales τ_1 =105.93, τ_2 =205.61, τ_3 =311.79, and τ_4 =427.21 using the LES: a) side (rear) view (yz plane at x=6.75m), and b) top view (xz plane at y=0m) contours of μ_{t-SGS}

Turbulent structures in Figures 52-53 are unsteady streamwise vortices evolved in the spanwise direction leading to formation of secondary coherent structures (Rogers and Moser, 1992). It is observed in Figure 52 that, at the second station, x=3.5m, streamwise subgrid scale turbulent viscosity (and consequently streamwise vorticity) distribution does not change significantly. However, vorticity strength on the walls is somewhat reduced in comparison with the first station. The vortical structures experience more apparent changes in the last two stations such that their corresponding peak levels of μ_{t-SGS} relatively increase in the core regions. This increase is interpreted to be due to either turbulence reproduction mechanisms or shear stress (strain rate) amplification in the core regions of the coherent vortical structures. It is notable that the spanwise rollers exhibit their strongest effects in the near-field region, resulting in alignment of the vortices in the main stream flow direction. Their contribution is then decreased further downstream of the mixing layers leading to a fast decay of the streamwise and spanwise vortices at the last station. This behavior is frequently seen for flows with low percentages of inflow disturbances (Wiecek and Mehta, 1998).

Furthermore, as shown in the side (rear) view contours, the decaying large scale turbulent eddies (dominated by hairpin structures (Brinkerhoff and Yaras, 2014)) proceed through the mixing layers such that most of the viscous dissipation is observed at the last station. However, the mean velocity gradients across the mixing layers guarantee continuous production of the turbulent kinetic energy and reproduction of the coherent vortical structures. As time proceeds, primary hairpin structures stretch and grow in the streamwise and lateral directions to initiate reproduction of the turbulent vortices and spots (Brinkerhoff and Yaras, 2014). It is noted that these coherent structure patterns appear similarly at the intermittent interface of the mixing layer non-turbulent and turbulent fields (Holmes, 1998).

Another important observation of Figures 52-53 is the presence of the turbulence structures adjacent to the channel walls. Subgrid-scale turbulent viscosity in these regions is maximum at x=1.75m, and then starts decreasing as the flow proceeds through the domain. High percentages of the μ_{t-SGS} in the near-wall region are mainly attributed to the development of the unstable boundary layers (shear layers) containing highly-fluctuating small eddies near the walls. These eddy structures have higher strain rates and energy (including production and dissipation) compared to other existing structures in the flow field. It should be pointed out that turbulence is damped out slowly in the near-wall regions (viscous sublayer) such that boundary layers in these regions are dominated by viscous forces (White, 2006, pp. 398-485).

Included in the side (rear) view contours of the μ_{t-SGS} in Figures 52-53 is a very thin layer on the symmetry line of the contour planes. This layer represents the nearly-inviscid potential core of the mixing layers and is generated due to the wake region behind the airfoil. Because of the high convective acceleration corresponding to such a plane wake, this potential core vanishes far downstream in the mixing layers (White, 2006, pp. 398-485). It is worthwhile to mention that formation of calmed regions behind the turbulent spots' trailing edges and also sweep motions generated by hairpin structures, are expected to affect the potential core behavior (Sabatino and Smith, 2008).

Time-varying contours of the mean velocity magnitudes at free-stream Re=500,000 with I=2% are shown in different views in Figure 54. 3D evolution of these contours at the last simulation time τ_4=427.21 through the four streamwise uniformly-spaced planes (stations) are depicted in Figure 55. Spatial growth of the turbulent mixing layers originating from the airfoil trailing edge is the prominent observation of these contours. A decrease in the effects of the channel side walls on the evolution of the flow is also seen in the side (rear) view contours. Moreover, momentum loss and mass deficit across each of the stations increase in the streamwise direction (White, 2006, pp. 398-485).

τ_1=105.9

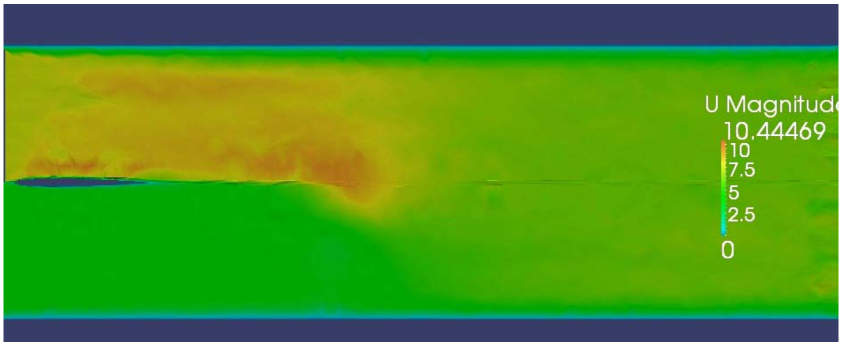

τ_2=205.6

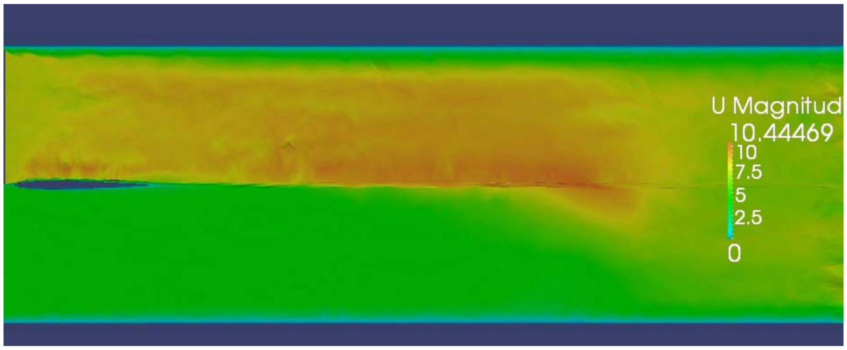

τ_3=311.7

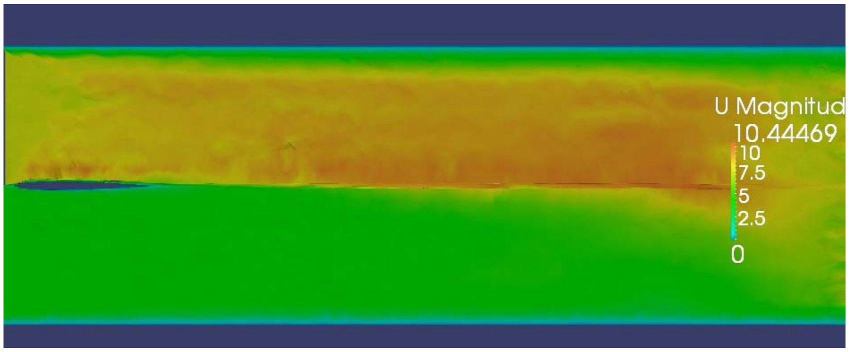

τ_4=427.2

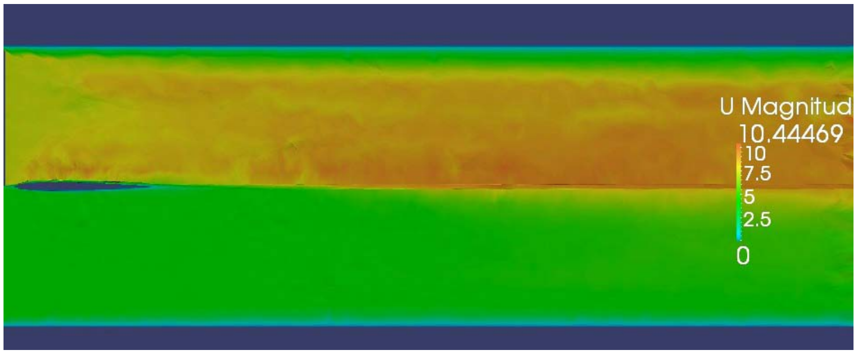

(a)

τ_1=105.9

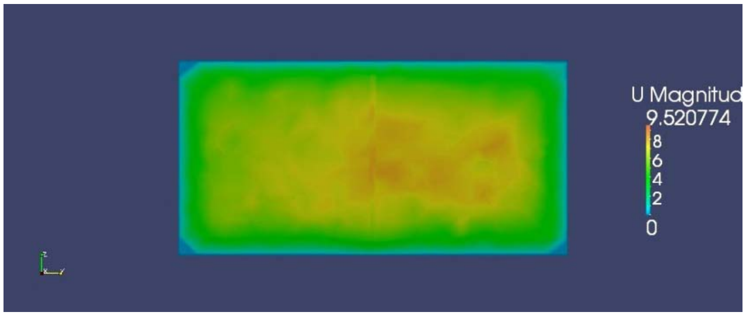

τ_2=205.6

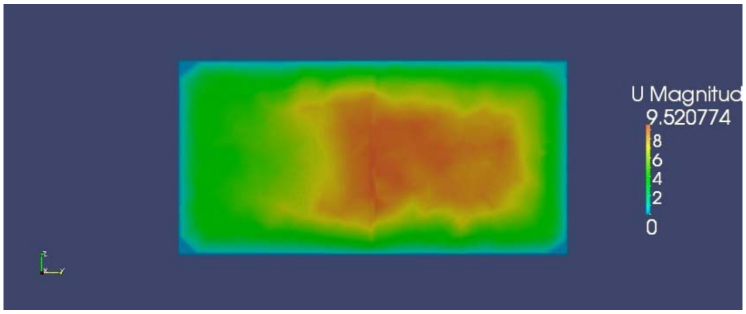

τ_3=311.7

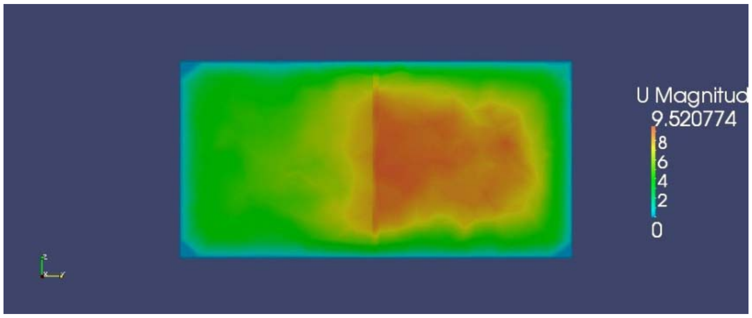

τ_4=427.2

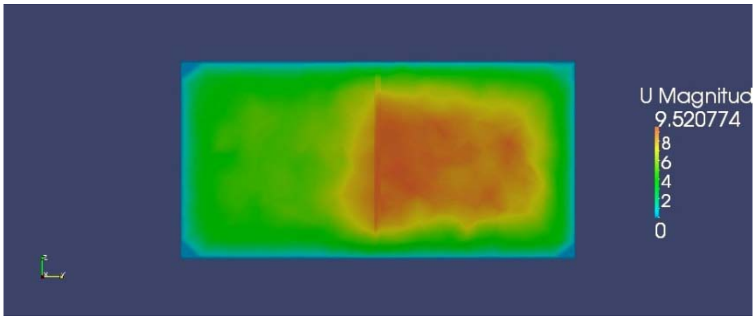

(b)

τ_1=105.9

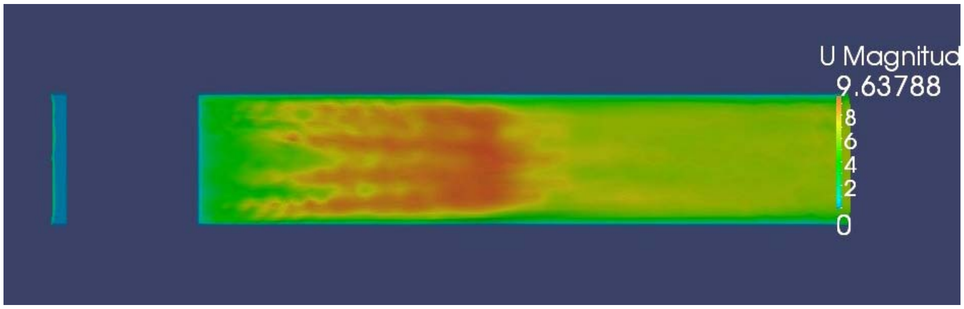

τ_2=205.6

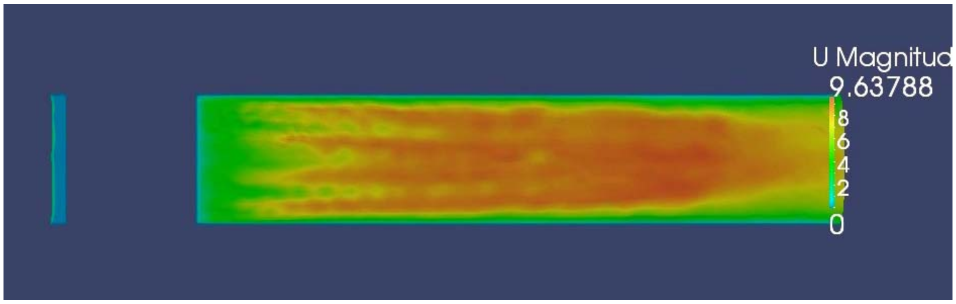

τ_3=311.7

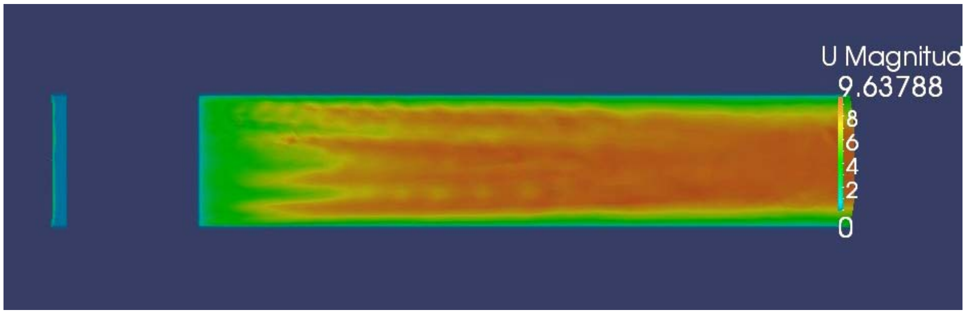

τ_4=427.2

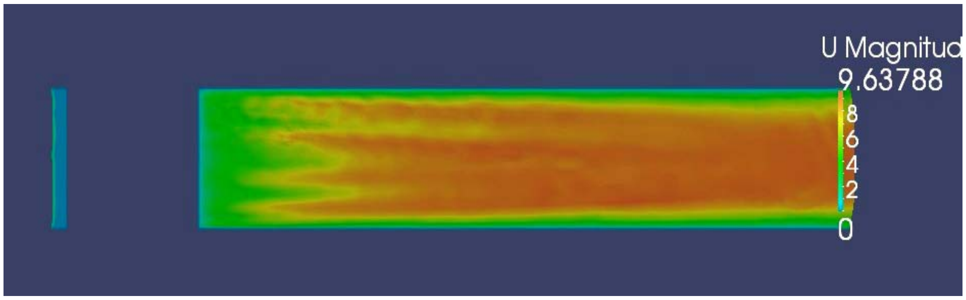

(c)

Fig. 54: Temporal evolution of the 3D turbulent mixing layers in the streamwise direction at free-stream Re=500,000 with I=2% at dimensionless time scales τ_1=105.93, τ_2=205.61, τ_3=311.79, and τ_4=427.21 using the LES: a) front view (xy plane at z=0m), b) side (rear) view (yz plane at x=6.75m), c) top view (xz plane at y=0m)

Figure 54 shows streamwise evolution of the coherent structures of the mean streamwise velocity in different contour views. A major observation in the contours is the spanwise presence of the equally-spaced turbulent streaks starting at the airfoil trailing edge. These high-speed streaks are formed mainly due to: 1) the high vorticity magnitudes at the airfoil trailing edge; and 2) the transfer of the momentum from the high-speed streams to the low-speed streams (Johnson, 2001). They merge slowly with the coherent structures in further downstream regions. As suggested by Schröder et al. (2008), differences in the speeds of these streaks generate strong spanwise shear layers. These unstable shear layers stretch and develop, along with the primary streamwise vortices, to form the secondary hairpin structures. As time proceeds, the turbulent eddies become larger such that their turbulent kinetic energy and consequently intermittency of the turbulence decrease (streak disappearance). This is in contrast to the outer-layer regions with larger scale eddies and less intermittency. It is noted that the observed turbulent streaks are different from the 2D rib structures shown in the laminar case. However, development of the 2D ribs leads to the formation of the larger vortical structures.

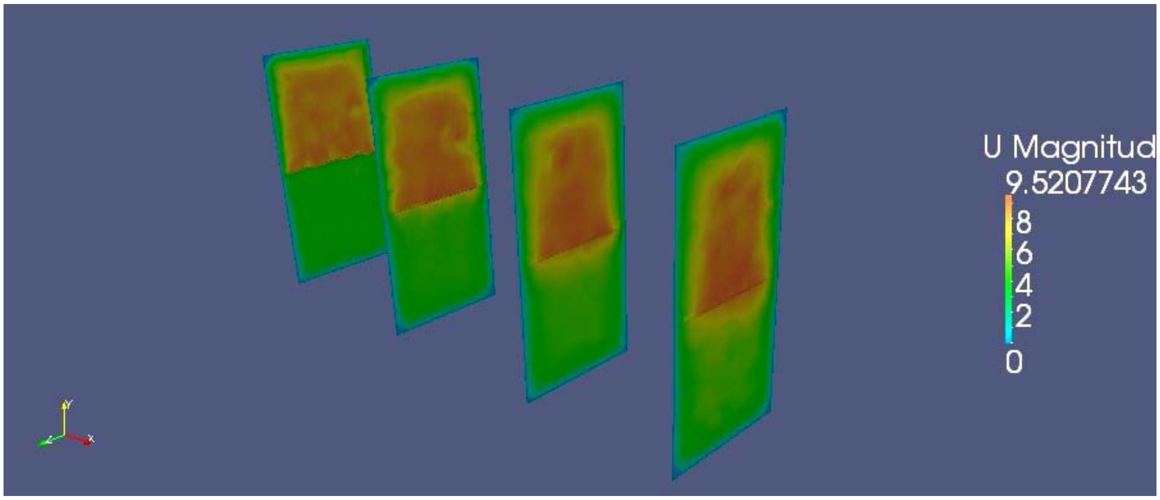

Fig. 55: Spatial evolution of the 3D turbulent mixing layers at free-stream Re=500,000 with I=2% at the last simulation time τ_4=427.21 across the four streamwise uniformly-spaced planes (x=1.75, 3.5, 5.5, 6.75m) using the LES: 3D view contours of mean velocity magnitude

Visual inspection of the figures in the top view also indicates that streamlines distributed in the spanwise direction are drifted approximately toward the centerline of the mixing layers. It is expected that the "separating lines" formed on the airfoil surfaces coincide with this centroidal line (White, 2006, pp. 308-319).

6.2.1. Time-Averaging

Since a wide range of random motions with different time scales are observed in the LES study of the present work, and also to ensure that the turbulent mixing layers are fully developed, the LES simulations were allowed to run for a longer period of time. This time period was set approximately to twice the time required for the inlet velocity field to march through the whole domain (about 1.65s). Using this increased time makes the unsteady turbulent mixing layers statistically steady. However, steadiness is not basically defined in LES solutions. Thus, an averaged mean velocity profile at x=6.75m and z=0m was attained by using time-averaging of all mean velocity profiles found by the flow time of 4.1s. Figure 56a shows all mean velocity profiles at high-speed side Reynolds number of 500,000 with I=2% found for equal time step sizes of 0.1s between flow times of 1s and 4.1s (τ_1=105.93 and τ_4=427.21). As depicted, the mean velocity profiles show spotty (jagged) behavior at different time steps which is expected to be due to the presence of an intermittent region (superlayer) at the interface of the turbulent and non-turbulent regions.

Although there is an approach to the self-similarity in the profiles shown in Figure 56, because of the lasting effects of the wake generated by the airfoil on one hand, and continuous reproduction mechanisms inside the turbulent flow field on the other hand, self-similarity cannot be observed clearly even at large flow times. This implies small turbulence dissipation compared to turbulence production within the simulation time (White, 2006, pp. 398-485).

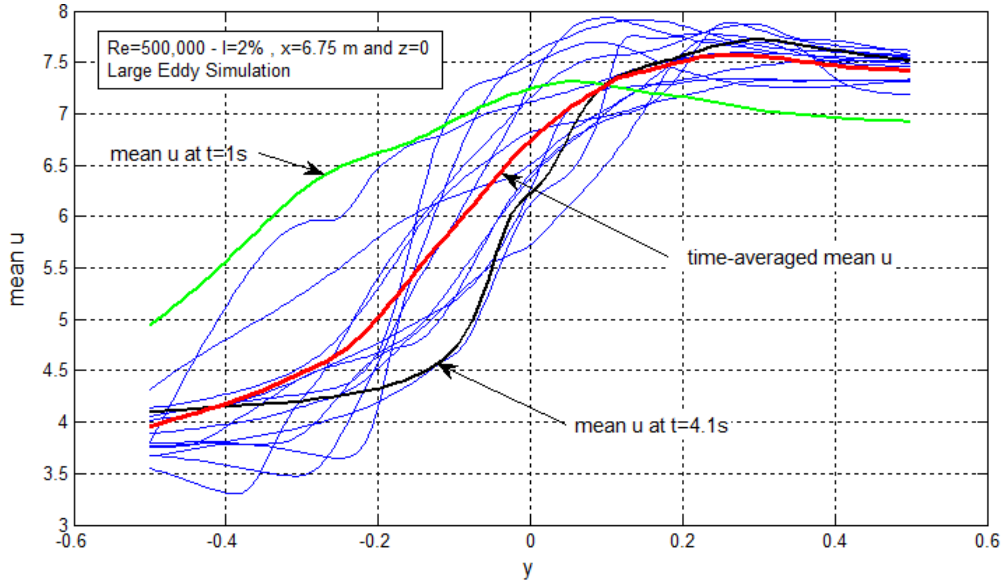

(a)

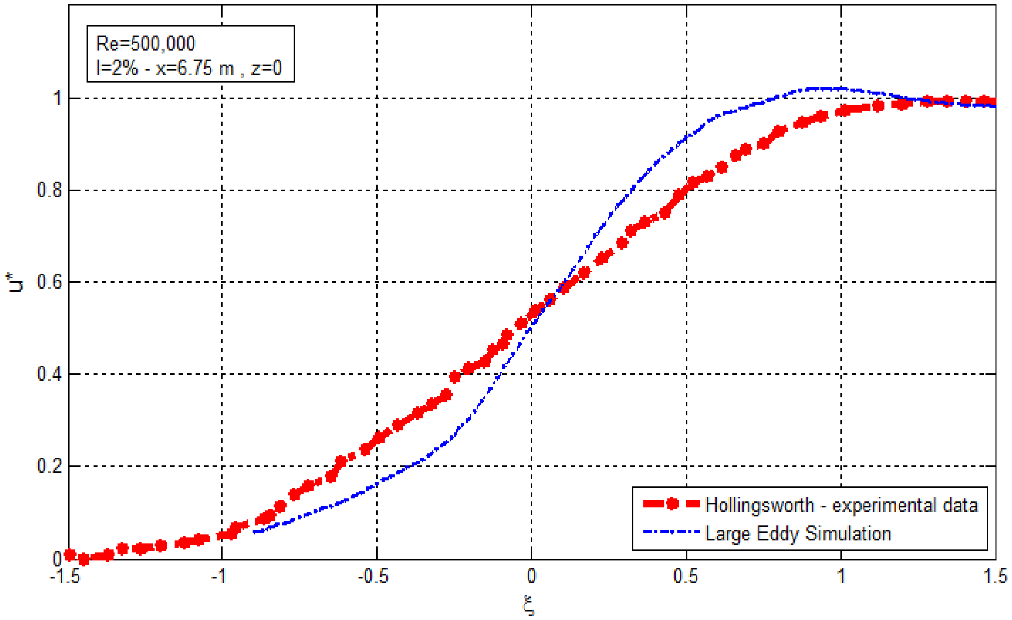

(b)

Fig. 56: Time-averaged velocity profiles for the 3D turbulent mixing layer using the LES method: a) temporal evolution of the mean velocity profiles at x=6.75m and z=0m, between flow times τ_1=105.93 and τ_4=427.21 with equal time step sizes Δt=0.1s, b) comparison of the LES results with experimental data of Hollingsworth and Bourgogne (1995)

Included in Figure 56b is also experimental data of Hollingsworth and Bourgogne (1995). As indicated in the figure, and by visual inspection of the data, it is possible to conclude that in the numerical simulations of the unsteady 3D turbulent mixing layers, the LES findings are in the closest agreement with experimental data in comparison with the previous results obtained by SST and LGRSTM models.

Chapter 7: Conclusion and Recommendation for Future Work

7.1. Summary and Conclusion: Laminar Mixing Layers

Laminar mixing layers generated behind a NACA0006 airfoil in two and three dimensional domains exposed to different high-speed side free-stream Reynolds numbers and temperatures were investigated numerically by using ANSYS-Fluent for 2D and OpenFoam for 3D computation domains. Numerical results are validated against an analytical solution of the simplified Navier-Stokes equations for 2D Falkner-Skan mixing layers solved in Matlab. In spite of the existence of overshoots in velocity profiles at Re=10,000, evaluations of the findings show a reasonable consistency with the analytical solution. The differences are mainly due to the wall boundary layer effects, the local pressure gradients formed by the presence of the airfoil, and also possibly numerical errors. This conclusion was also confirmed through a series of verifying numerical simulations for similar mixing layers behind a flat plate splitter.

The findings of the 2D simulations show that increasing the free-stream temperature over the airfoil has a negative effect on the stability of mixing layers, pushing the onset of instability further upstream in the flow. This behavior is improved at higher free-stream velocities.

The numerical simulations for the 3D laminar mixing layer show wavy-shape behaviors of the mixing layer in both streamwise and spanwise directions. However, the main flow is estimated to evolve with the least variations in the spanwise z direction showing approximately a Blasius-type velocity profile in the last station of the domain. Nevertheless, the presence of three-dimensionality was evidently seen in the corresponding velocity contours, confirming variation of flow parameters in both directions. So, it can be explained that although the similarity solution of Blasius and basically boundary layer theory do not apply for the wake region, they are still reasonably applicable in dealing with 2D and even 3D laminar mixing layers behind the NACA0006 airfoil. It is emphasized that in the case of initial crossflow in the spanwise z direction, or general complex flows, possible similarity solutions fail to predict the true behavior of the fluid flow.

7.2. Summary and Conclusion: Turbulent Mixing Layers

Steady and unsteady behaviors of the turbulent mixing layers in 2D and 3D hybrid mesh grids were studied. In the case of the 2D steady simulations, RANS-based models including S-A, $k-\epsilon$, $k-\omega$, transition $k-kl-\omega$, SST, and RAS were tested in ANSYS-Fluent. For the 3D cases, selected RANS-based models in OpenFoam i.e. $k-\epsilon$ (Realizable), SST, and LGRSTM were used to investigate the behavior of the mean velocity profiles and mixing layer growth at different free-stream turbulence intensities. Selection of the RANS-based models in OpenFoam was based on the reliability of the results of the 2D simulations. In order to reduce the computation time, 3D simulations were run in parallel, on four processors. Comparison of the numerical results with the experimental data indicate that for both 2D and 3D cases, best matches were found for SST and RAS (and LGRSTM) turbulence models. This conclusion is mainly due to the presence of the empirical correlations in the derivations of the SST and RAS models. These correlations control the onset of transition, length of transition region, and excess of turbulent diffusion in the flow.

Dimensionless mean velocity profiles of the turbulent mixing layers plotted at x=6.75m were observed to be steeper compared to those found in the laminar case. Such a behavior is basically due to the nature of the turbulent viscosity showing high values in the outer layers and low values in the inner layers of the turbulent flow (White, 2006, pp. 398-485).

Large Eddy Simulation (LES) was conducted in OpenFoam over the 3D turbulent mixing layers by employing the same parallel computation method as the laminar case. Turbulent kinetic energy (k) eddy-viscosity model (oneEqEddy) was also used to resolve the sub-grid scale turbulent viscosity (μ_{t-SGS}) transport equation. In order to capture all turbulent scales precisely, inflow conditions for the LES simulations were taken as the mapped results of the LGRSTM modeling at x=6.75m, on the inlet plane of the LES computation domain (i.e. a fully-turbulent inflow). The mean velocity profiles were then time averaged within a large period of flow time to ensure approximated steadiness. The resultant time-averaged mean velocity profile matched well with the experimental data of mixing layers behind flat plates (Hollingsworth and Bourgogne, 1995). Such an agreement was not clearly seen in comparison of the 2D simulations with the analytical solution. In addition, verification of the findings with experimental data confirms that results of the LES model collapse better than the results estimated by SST and RAS (and LGRSTM) models. This slight difference might be attributed to uncertainties in the prediction of the turbulent kinetic energy by RANS-based models (Akhtar, 2010). However, it is expected that by using different types of airfoils, thicker and cambered, more distinctive behaviors of the mixing layers would be observed.

In spite of overall complications in reaching self-preservation of bounded mixing layers, comparing the results of the turbulent mixing layers behind the airfoil in the present work suggests that for higher intensity turbulence environments, lower shape factors and higher Reynolds stresses are predicted. Moreover, it is shown that increasing the free-stream Re number does not substantially affect the shape factor variations. This conclusion is estimated to be due to the fast diffusion of momentum, energy and mass in the turbulent mixing layers. Depending on the distance of the mixing region streamlines from the channel walls for the 3D case, this behavior relatively changes.

Furthermore, results of the studied turbulent mixing layers indicate that for higher free-stream Reynolds numbers and turbulence intensities, self-preservation of the Reynolds stresses and mean velocity profiles is attained at a longer streamwise distance (and at longer flow times) in comparison with the laminar case. The main reason for this conclusion is estimated to be due to more entrainment of the turbulent spots by stronger fluctuations (Pui and Gartshore, 1979). It is also observed that in the case of the turbulent mixing layers simulations, particularly LES, behavior of the mean velocity profiles, even in far downstream regions, is still dependent on the inflow conditions. This is in contrast with the laminar case where self-preserving velocity profiles are attained quickly and consequently flow becomes independent of the inflow conditions.

7.3. Future Work and Recommendations

Unsteady LES of turbulent mixing layers behind a NACA0006 airfoil in a 3D domain was studied. The pisoFoam solver in OpenFoam was used to resolve the corresponding governing equations i.e. continuity and momentum, by coupling the velocity and pressure gradients through a PISO algorithm. The applied solver does not account for solving the energy equation. Therefore, to investigate the effects of the free-stream temperature on the behavior of the turbulent mixing layers, a new solver, called "pisoFoamHeat.c" (source file), was developed by using the "fvCFD.h" (header file) code library in OpenFoam. To do that, the energy transport Equation (3) was rewritten as Equation (59) in OpenFoam, assuming a zero source term, and then coupled with the existing pisoFoam solver previously used for the LES simulations. Also, in order to study the influence of the heat conductivity on the results, a linear approximation of the thermal conductivity coefficient (k_h) in terms of a reference temperature, T_{ref}=300K, a reference thermal conductivity, ${k_h}_0$(at T_{ref}=300K), and with a constant coefficient A=0.001 $\frac{m^2}{s-K}$ was applied in the energy equation as:

$$\rho c_p\left(\frac{\partial T}{\partial t}+\nabla.(\mathbf{u}T)\right)-\nabla.(k_h\nabla T)=0 \tag{59}$$

where

$$k_h={k_h}_0-A\left(T-T_{ref}\right). \tag{60}$$

The new solver was compiled and used to investigate the effects of the high-speed side free-stream temperature on the 3D laminar mixing layers behavior. As shown in Figure 57, variations of the temperature within the mixing layers core, in contrast with the velocity contours, do not display wave like evolution at τ = 210.2. This might be because of the nature of temperature which is an extensive scalar quantity. Note that simulations were run for free-stream high-speed side Re=100,000 with the fixed velocity ratio of 2 between the sides. Also, free-stream temperature of the low-speed side was set to 200K whereas it remained at 300K for the high-speed side.

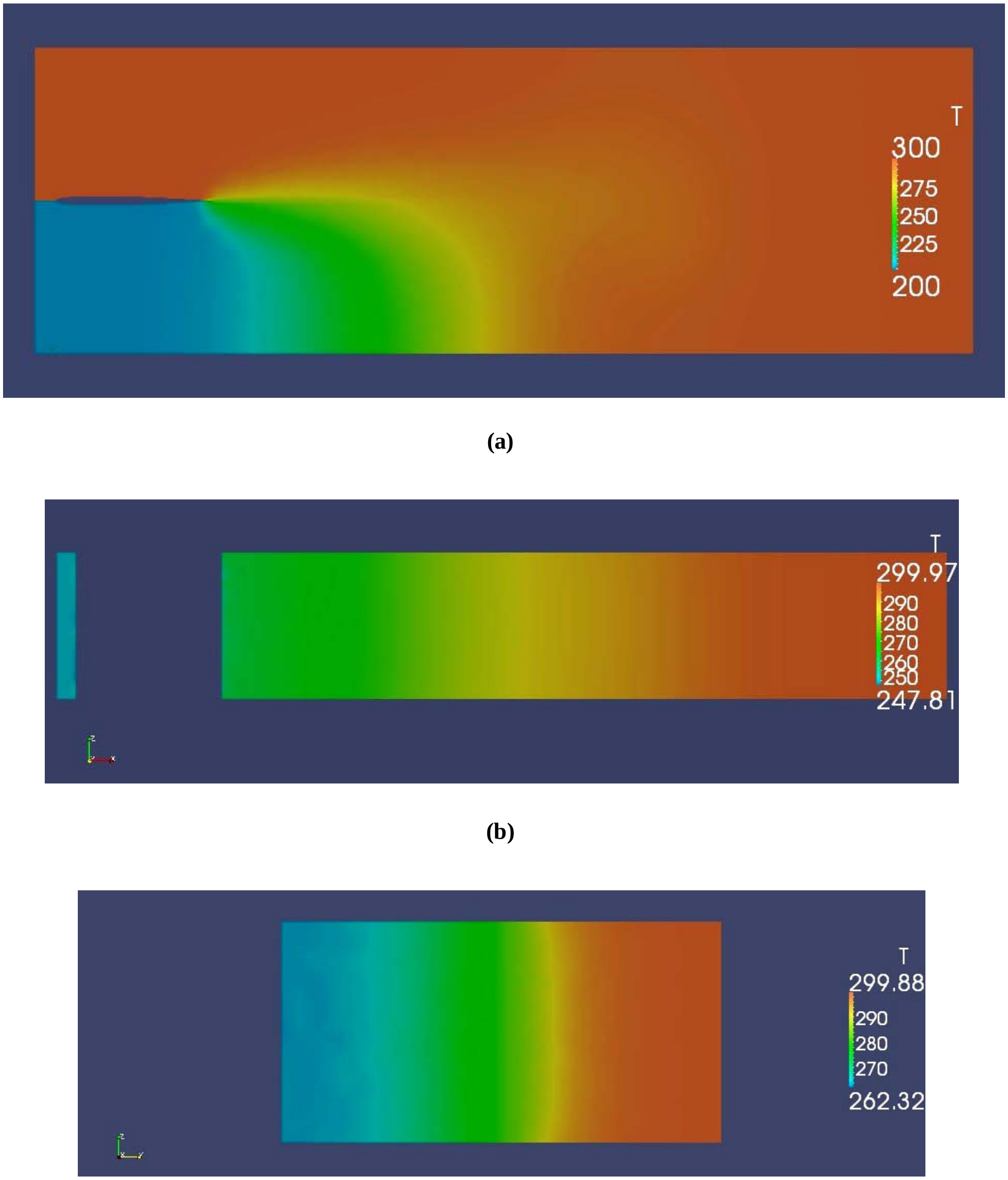

(a)

(b)

(c)

Fig. 57: Contours of temperature - 3D laminar mixing layers evolution at free-stream Re=100,000 with high-speed side temperature of 300K and low-speed side temperature of 200K at flow time τ = 210.2 using the "pisoFoamHeat" solver: a) front view (xy plane at z=0m), b) top view (xz plane at y=0), and c) side (rear) view (yz plane at x=6.75m)

Exploring the effects of the high-speed side free-stream temperature on the self-preservation behavior of the turbulent mixing layers behind the NACA0006 airfoil by using the developed solver “pisoFoamHeat” and LES method, is one of the future objectives of this research.

Experimental and high-order numerical investigations of the mixing layers generated in downstream regions of highly-curved airfoils with built-in suction or roughness elements (holes) on surface - extensively used to control the separation of the flow on guide vane blades in turbines - are recommended for future studies.

References

Abdolhosseini, R. and Milane, R. E. (2000). On the effect of vortex grid density in the vortex-in-cell simulation of mixing layer. *International Journal of Fluid Dynamics* 13, 161-183.

Akhtar, K. (2010). *Numerical Investigation using RANS Equations of Two-dimensional Turbulent Jets and Bubbly Mixing Layers*. M.A.Sc. Dissertation. Blacksburg, Virginia: Virginia Polytechnic Institute and State University.

Ames, F. E. and Moffat, R. J. (1990). *Heat transfer with High Intensity, Large Scale Turbulence: the Flat Plate Turbulent Boundary Layer and the Cylindrical Stagnation Point*. Report HMT-44. Dept. Mech. Eng., Stanford University.

ANSYS-Fluent, SAS IP, Inc. (2013). *Fluent Theory Guide*. Retrieved from http://www.arc.vt.edu/ANSYS_help/flu_ug/flu_ug.html. Feb. 2013.

Arnal, D. (1984). Description and prediction of transition in two-dimensional incompressible flow. AGARD Spec. Course on Stability and Transition of Laminar Flow 71p, pp. 2-1 to 2-71.

Baldwin, B. S. and Lomax, H. (1978). Thin Layer Approximation and Algebric Model for Separated Turbulent Flow. *AIAA Paper* 1978-257.

Bell, J. H. and Mehta, R. D. (1990). Dvelopment of a two-stream mixing layer with tripped and untripped boundary layers. *AIAA Journal* 28 (12), 2034-2042.

Bell, J. H. and Mehta, R. (1992). Measurements of the streamwise vortical structures in a plane mixing layer. *Journal of Fluid Mechanics* 239, 213-248.

Beninati, M. L. and Marshall, J. S. (2005). An experimental study of the effect of free-stream turbulence on a trailing vortex. *Experiments in Fluids* 38 (2), 244-257.

Bernal, L. and Roshko, A. (1986). Streamwise vortex structure in plane mixing layers. *Journal of Fluid Mechanics* 170, 499-525.

Birch, S. F. and Eggers, J. M. (1973). A critical review of the experimental data for developed free turbulent shear layers. NASA SP-321. vol. 1, *Conference Procs. - Free Turbulent Shear Flows Conference*, pp. 11-40. NASA Langley Research Center, Hampton, Virginia.

Brinkerhoff, J. R. and Yaras, M. I. (2014). Numerical investigation of the generation and growth of coherent flow structures in a triggered turbulent spot. *Journal of Fluid Mechanics* 759, 257-294.

Buell, J. and Mansour, N. N. (1989). Asymmetric effects in three-dimensional spatially developing mixing layers. *Proc. Seventh Symp. Turbulent Shear Flows* (pp. 9.2.1-9.2.6). Stanford University.

Cherdron, W., Durst, F., and White, J. H. (1978). Asymmetric flows and instabilities in symmetric ducts with sudden expansions. *Journal of Fluid Mechanics* 84, 13-31.

Das, D. K. (1988). A Simple Theory for Calculating Turbulent Boundary Layers under Arbitrary Pressure Gradients. *International Journal of Engineering Fluid Mechanics* 1, 83-99.

Do, T., Chen, L., and Tu, J. (2010). Numerical study of turbulent trailing edge flows with base cavity effects using URANS. *Journal of Fluids and Structures* 26 (7-8), 1155-1173.

Dunn, M. G., Martin, H. L., and Stanek, M. J. (1986). Heat Flux and Pressure Measurements and Comparison with Prediction for a Low Aspect Ratio Turbine Stage. *Journal of Turbomachinery* 108, 108-155.

Görtler, H. (1957). A New Series for the Calculation of Steady Laminar Boundary Layer Flows. *Journal of Mathematics and Mechanics* 6, 1-66.

Hartree, D. R. (1937). On an equation occurring in Falkner and Skan's approximate treatment of the equations of the boundary layer. *Proc. Cambridge Philos. Soc.*, 33, 223–239.

Hollingsworth, D. K. and Bourgogne, H. A. (1995). The development of a turbulent boundary layer in high free-stream turbulence produced by a two-stream mixing layer. *Experimental Thermal and Fluid Science* 11, 210-222.

Holmes, P. E. (1998). *Turbulence, Coherent Structures, Dynamical Systems, and Symmetry*. New York: Cambridge University Press.

Hughes, T. H. and Reid, W. H. (1965). On the stability of the asymptotic suction boundary layer profile. *Journal of Fluid Mechanics* 23, 715-735.

Ito, Y., Nagata, K., Sakai, Y., and Terashima, O. (2013). Momentum and mass transfer in developing liquid shear mixing layers. *Journal of Experimental Thermal and Fluid Science* 51, 28-36.

Johnson, M. W. (2001). On the flow structure within a turbulent spot. *International Journal of Heat and Fluid Flow* 22, 409–416.

Johnson, P. L. and Johnston, J. P. (1989). *The Effects of Grid-Generated Turbulence on Flat Plate and Concave Turbulent Boundary Layers*. Report MD-53, Dept. Mech. Eng., Stanford University.

Kaltenbach, H.-J. (1997). Cell aspect ratio dependence of anisotropy measures for resolved and subgrid scale stresses. *Journal of Computational Physics* 136, 399-410.

Klebanoff, P. S. (1955). *Characteristics of Turbulence in a Boundary Layer with Zero Pressure Gradient*. NACA Report 1247.

Kline, S. J., Cantwell, B. J., and Lilley, G. M. (1982). Complex Turbulent Flows: Comparison of Computation and Experiment. *The 1980-81 AFOSR - HTTM Stanford Conference on Complex Turbulent Flows: Comparison of Computation and Experiment* (vols. 1-3, 1248-1251). Stanford University, Stanford, California.

Koutmos, P. and McGuirk, J. J. (1989). Isothermal Flow in a Gas Turbine Combustor - A Benchmark Experimental Study. *Experiments in Fluids* 7, 344-354.

Lakehal, D., Smith, B. L., and Milelli, M. (2002). Large-eddy simulation of bubbly turbulent shear flows. *Journal of Turbulence* 3, N 25.

Lasheras, J. C. and Choi, H. (1988). Three-dimensional instability of a plane free shear layer: an experimental study of the formation and evolution of streamwise vortices. *Journal of Fluid Mechanics* 189, 53-86.

Launder, B. E. and Spalding, D. B. (1972). *Lectures in Mathematical Models of Turbulence*. London, England: Academic Press.

Leboeuf, R. L. and Mehta, R. D. (1993). Streamwsie vortex meander in a plane mixing layer. *Physics of Fluids* A 5, 1983-1991.

Leboeuf, R. L. and Mehta, R. D. (1996). Vortical structure morphology in the initial region of a forced mixing layer: Roll-up and pairing. *Journal of Fluid Mechanics* 315, 175-221.

Lees, L. and Lin, C. C. (1964). *Investigation of the Stability of the Laminar Boundary Layer in a Compressible Fluid*. National Advisory Committee for Aeronautics, Report No. 876, Washington, D. C.

Lock, R. C. (1951). The velocity distribution in the laminar boundary layer between parallel streams. *Quarterly Journal of Mechanics and Applied Mathematics* 4, 42-63.

Maciejewski, P. K. and Moffat, R. J. (1989). *Heat Transfer with very High Free-Stream Turbulence*. Report HMT-42. Dept. Mech. Eng., Stanford University.

Masutani, S. M. and Bowman, C. T. (1986). The structure of a chemically reacting plane mixing layer. *Journal of Fluid Mechanics* 172, 93-126.

Mavriplis, C., Schrader, L. U., Wajda, V., and Chrust, M. (2013). Control of Separated Flow Over a NACA 2415 Airfoil by Spectral Element Direct Numerical Simulation. *15th CASI Aerodynamics Symp.*

Mehta, R. D. (1991). Effect of velocity ratio on plane mixing layer development: influence of splitter plate wake. *Experiments in Fluids* 10, 194-204.

Mehta, R. D. and Westphal, R. V. (1986). Near-field turbulence properties of single- and two-stream plane mixing layers. *Experiments in Fluids* 4, 257-266.

Melander, M. V. and Hussain, F. (1993). Coupling between a coherent structure andfine scale turbulence. Physical Review E 48, 2669-2707.

Metcalfe, R. W., Orszag, S. A., Brachet, M. E., Menon, S., and Riley, J. J. (1987). Secondary instability of a temporally growing mixing layer. *Journal of Fluid Mechanics* 184, 207-243.

Milane, R. E. (2004). Large eddy simulation (2D) using diffusion-velocity method and vortex-in-cell. *International Journal for Numerical Methods in Fluids* 44, 837-860.

Moin, P. and Mahesh, M. (1998). Direct Numerical Simulations: A Tool in Turbulence. *Annual Review of Fluid Mechanics* 30, 539-578.

OpenFOAM Foundation, OpenCFD Ltd. (2011-2015). *OpenFoam User Guide*. Retrieved from http://www.openfoam.org/docs/user/index.php. Jan. 2014.

Oster, D. and Wygnanski, I. J. (1982). The forced mixing layer between two parallel streams. *Journal of Fluid Mechanics* 123, 91-130.

Pentelow, S. (2014). *Wing-Tip Vortex Structure and Wandering*. M.A.Sc. Dissertation. Dept. Mech. Eng., University of Ottawa, Ontario, Canada.

Plesniak, M. W. and Johnston, J. P. (1988). The Effects of Stabilizing and Destabilizing Curvature on a Plane Mixing Layer, in M. Hirata and N. Kasagi (Eds.). *Transport Phenomena in Turbulent Flows*, pp. 377-390. Hemisphere, New York.

Plesniak, M. W. and Johnston, J. P. (1989). *The Effects of Longitudinal Curvature on Turbulent Two-Stream Mixing Layers*. Report MD-54, Dept. Mech. Eng., Stanford University.

Pui, N. K. and Gartshore, I. S. (1979). Measurement of the growth rate and structure in plane turbulent mixing layers. *Journal of Fluid Mechanics* 91, 111-130.

Reshotko, E. (1987). Stability and transition, how much do we know? in J. P. Lamb, (Ed.), *Proceedings of the Tenth U.S. National Congress of Applied Mechanics, American Society of Mechanical Engineers*, pp. 421-434. New York.

Rogers, M. M. and Moser, R. D. (1992). The three-dimensional evolution of a plane mixing layer: The Kelvin-Helmholtz rollup. *Journal of Fluid Mechanics* 243, 183-226.

Roig, V., Suzanne, C., and Masbernat, L. (1998). Experimental investigation of a turbulent bubbly mixing layer. *International Journal of Multiphase Flow* 24 (1), 35-54.

Rumsey, C. L. and Ying, S. X. (2002). Prediction of high lift: review of present CFD capability. *Progress in Aerospace Sciences* 38, 145-180.

Sabatino, D. R. and Smith, C. R. (2008). Turbulent spot flow topology and mechanisms for surface heat transfer. *Journal of Fluid Mechanics* 612, 81–105.

Sabin, C. M. (1965). An analytic and experimental study of a plane, incompressible, turbulent shear layer with arbitrary velocity ratio and pressure gradient. *Transactions of the ASME. Series D, Journal of Basic Engineering* 87, 421-428.

Schlichting, H. and Gersten, K. (2000). *Boundary Layer Theory*, 8th ed., New York: Springer.

Schröder, A., Geisler, R., Elsinga, G. E., Scarano, F., and Dierksheide, U. (2008). Investigation of a turbulent spot and a tripped turbulent boundary layer flow using time-resolved tomographic PIV. *Experiments in Fluids* 44, 305–316.

Shang, Z. (2014). Impact of mesh partitioning methods in CFD for large scale parallel. *Computers and Fluids* 103, 1-5.

Tavoularis, S. (2012). *Theory of Turbulence* (Lecture Notes). University of Ottawa, Ontario, Canada.

The MathWorks, Inc. (2015). *Global Optimization Toolbox*. Retrieved from http://www.mathworks.com/products/global-optimization/features.html#genetic-algorithm-solver. June 2014.

Thole, K. A. (1992). *High Free-Stream Turbulence Effects on the Transport of Heat and Momentum*. Ph.D. Dissertation, Dept. Mech. Eng., University of Texas, Austin.

Townsend, A. A. (1976). *Structure of Turbulent Shear Flow*. Cambridge: Cambridge University Press.

Tung, C. (1992). *Initial Streamwise Vorticity Formation in a Two-Stream Mixing Layer*. Ph.D. Dissertation. Dept. Mech. Eng., University of Houston.

Wazzan, A. R., Gazley, C. J., and Smith, A. M. (1979). Tollmien-Schlichting waves and transition. *Progress in Aerospace Sciences* 18 (2), 351-392.

Westerweel, J., Fukushima, C., Pederson, J. M., and Hunt, J. C. (2009). Momentum and scalar transport at the turbulent/non-turbulent interface of a jet. *Journal of Fluid Mechanics* 631, 199-230.

Weygandt, J. H. and Mehta, R. D. (1995). Three-dimensional structure of straight and curved plane wakes. *Journal of Fluid Mechanics* 282, 279-311.

White, F. M. (2006). *Viscous Fluid Flow*, 3rd edition., New Delhi: McGraw Hill Education.

Wiecek, K. C. and Mehta, R. D. (1998). Effects of velocity ratio on mixing layer three-dimensionality. *Experimental Thermal and Fluid Science* 16, 165-176.

Wilcox, D. C. and Rubesin, M. W. (1980). *Progress in Turbulence Modeling for Complex Flow Fields Including Effects of Compressibility*. NASA TP-1517.

Yarusevych, S., Sullivan, P. E., and Kawall, J. G. (2004). Investigation of airfoil boundary layer and wake development at low Reynolds numbers. *AIAA Paper 2004-2551*.